楕円空孔コア円形空孔ホーリーファイバを用いた光デバイスの設計

Doctoral Thesis

Design of Optical Devices Based on Single-Polarized Elliptical-hole Core Circular-hole Holey Fiber

Zejun ZHANG

Muroran Institute of Technology

March 2016

Contents

Chapter 1

Preface

With the rapid development of information society, the demand for high-speed large-capacity optical communication system is further increased. In order to achieve this objective, the demand for high-performance optical devices has also been increased. In recent years, several ways to enhance the information propagation velocity and expand the transmission capacity have been investigated, such as the automatic optimum design of optical devices [1]-[12], the study on multiplexing communication systems [13]-[14], novel optical devices based on special fibers [15]-[47], and so on. Multiplexing is the set of techniques that allows the simultaneous transmission of multi signals across a single data link. For the multiplexing communication systems there are some key optical devices, such as polarization splitter (PS) [48]-[63], polarization converter (PC) [64]-[77], mode converter/splitter (MCS) [78]-[84], and so on. Recently, novel passive optical devices based on special optical fibers have been attracted much attentions and have been widely studied.

Among the special optical fibers, novel fibers consisting of a single material with air holes have made remarkable advances over the past decade and their ideas were first presented, to our best knowledge, by Kaiser and Astle in 1947. Thereafter, in the last two decades, photonic crystal fibers (PCFs) [15]-[18], consisting of single material with a periodical array of air holes around the fiber core, have attracted a lot of attention due to their special properties that cannot be obtained by the conventional fibers, such as large mode area, endless single mode, high nonlinearity, and so on [16]. One of these properties is the absolutely single polarization transmission, and a number of single-polarized PCF structures have been proposed

[25]-[41]. Among these structures, a single-polarized PCF with a core consisting of elliptical-holes, which called elliptical-hole core circular-hole holey fiber (EC-CHF), has been proposed recently [35],[36]. These studies show that EC-CHF can be designed to transmit only x- or y-polarization easily by changing the major axis direction of the elliptical-holes in core region.

A PS, which can split a light beam into two orthogonal polarization states, is very important component in coherent optical communication system and optical-fiber sensing system. For the polarization division multiplexing (PDM) system, the PS can be used to split and composite the orthogonal polarized light waves. Several designs of PS based on PCF have been proposed. In 2003, a PS based on dual-core PCF has been proposed by Zhang and Yang [48], and an extinction ratio (ER) of -11 dB with a bandwidth of 80 nm can be achieved in the PS which is consisted of dual-core PCF with three kinds of different core sizes. After that, several kinds of PSs based on new structure of PCFs were proposed [49]-[63]. In 2004, Saitoh $et\ al.$ proposed a PS using three-core PCF, which has an ER better than -20 dB for the bandwidth of 37 nm with a device length of 1.9 mm [57]. In 2013, Lu $et\ al.$ proposed a PS based on three-core PCF which is designed by using the difference between coupling lengths of x- and y-polarizations, respectively. It has an ER as low as -20 dB with a ultra-broad bandwidth of 400 nm, while it suffers from a long splitting length of 72.5 mm [59]. Although many new kinds of PSs based on PCF have been proposed, none of them can realize the crosstalk-free separation.

In addition, in recent years, silicon-on-insulator (SOI) has been considered as a promising platform for photonic circuits due to the CMOS-compatible fabrication technology and the high refractive-index contrast of the waveguide structure [64],[65]. However, such high refractive indices also lead to a high polarization dependence of the group index [66]. In order to overcome this problem, a polarization diversity scheme could be employed. In this case, firstly, the orthogonal polarization components of incident light are split into two different waveguides by using a PS. Then, the polarization of guided light in one of the waveguide is rotated 90° by using a PC. Therefore, in the rest of the photonic circuit only one polarization has to be processed. Various polarization splitter/converters (PSCs) based on SOI waveguides have been proposed so far [67]-[71]. In 2011, L. Liu $et\ al.$ proposed a polarization splitting and rotating device built on the SOI plat-

form with a total length of 36.8 μm [67]. The insertion loss is -0.6 dB and the ER is 12 dB. Moreover, the PC based on PCF has also been studied [72]-[77]. In 2012, Hameed $et\ al.$ proposed a novel design of single and multiple sectioned passive PC based on rectangular lattice PCF with a L-shaped core region [72]. The single and multiple sectioned PCF PCs offer nearly 100% polarization conversion ratio with device lengths of 1743 μm and 1265 μm. In 2013, Hameed $et\ al.$ proposed a passive ultra-compact PC based on soft glass equiangular spiral photonic crystal fiber (ES-PCF) which offers 99% polarization conversion ratio with an ultra-compact device length of 96 μm [74]. However, the spiral structure complicates the fabrication process. Until now, the PSC based on PCF has not been widely investigated.

So far, all the proposed optical devices based on PCF have to discuss the ER, in order to obtain a low ER with a wider bandwidth, devices always suffering a long device length or a complex structure. Therefore, optical device with the cross-talk free property is the main objective of our research. Based on the absolutely single-polarized EC-CHF mentioned before, we proposed several cross-talk free passive optical devices and the propagation property of each device has also been investigated in detail. In chapter 2, I will give a brief introduction about the PCF and its applications. Then, in this research, since the full-vectorial finite element method (FV-FEM) [85],[86] and full-vector finite element beam propagation method (FE-BPM) [87] have been employed to simulate the modal effective index of the waveguide and the propagation behavior of incident light, respectively. I will explain the vector finite element analysis of PCF in chapter 3. After that, the main part of this thesis, I will focus on the design of optical devices based on EC-CHF. In chapter 4, we propose a novel cross-talk free PS based on EC-CHFs which can split x- and y-polarized waves into two different fibers. Simulation results demonstrate the PS with large hole EC-CHFs (air filling fraction in core is 36.73%) and small hole EC-CHFs (air filling fraction in core is 4.08%) can completely split an arbitrarily polarized light beam into two orthogonal polarization states without any crosstalk, respectively. In addition, the tolerance and wavelength dependence of the PS have also been discussed. In chapter 5, a novel single PC element based on square lattice EC-CHF with 45 degrees oblique elliptical holes in core has been proposed. Utilizing the symmetry property of the square lattice EC-CHF, an incident orthogonal polarization can be converted 90 degrees. Moreover, we adopt two

EC-CHF waveguides at both sides of the PC to achieve the cross-talk free property. In chapter 6, in order to contribute to the PDM and mode division multiplexing (MDM) system simultaneously, we consider a MCS based on square lattice EC-CHFs to achieve the mode splitting and converting. Finally, the conclusions and future work of this research are given in chapter 7.

Chapter 2

Background

In this chapter, first, we will give a brief introduction about the PCF and its applications. Then, we will illustrate the special PCF with elliptical holes in the core, *i.e.* EC-CHF which can achieve the absolutely single polarization transmission easily.

2.1 Optical Device Utilizing PCF

2.1.1 Photonic Crystal Fiber

Pioneered by the research group of Philip St. J. Russell in the 1990s, the development of PCFs and the exploration of the great variety of possible applications have attracted huge interest. This is partly because these fibers offer many degrees of freedom in their design to achieve a variety of peculiar properties, which make them interesting for a wide range of applications. A photonic crystal fiber (also called holey fiber, hole-assisted fiber) is an optical fiber which obtains its waveguide properties from an arrangement of very tiny and closely spaced air holes which go through the whole length of fiber. There is a great variety of hole geometries and arrangements, which can lead to PCFs with very different properties. All these PCFs can be considered as specialty fibers. In recent decades, PCFs have been widely used in the optical devices [42]-[47], such as fiber lasers [42]-[44], optical switch [45], fiber sensor [46], and so on. This is because PCFs have the unique light wave guided properties, including the endless single-mode, flexible dispersion control, absolutely single polarization, *etc.*

According to the different light wave guided mechanisms, PCF can be generally divided into two categories: the holey fiber (HF) that light wave confinement using

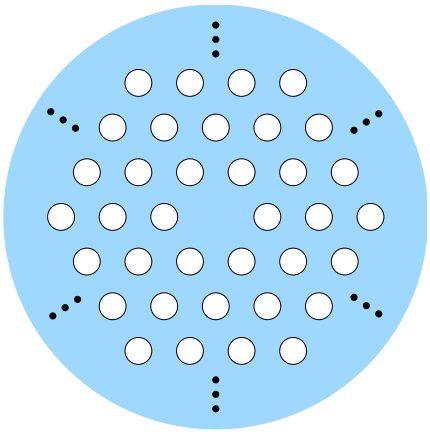

Figure 2.1: Cross sectional view of conventional HF with a triangular pattern of air holes, where the central hole is missing.

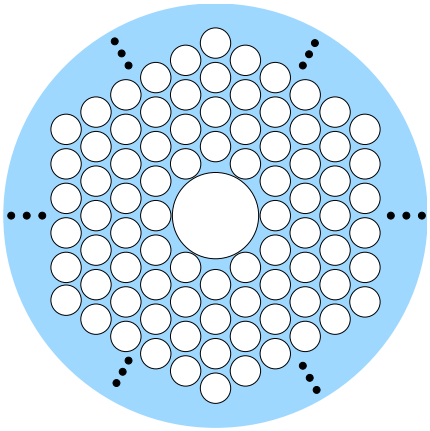

Figure 2.2: Cross sectional view of a PBG fiber with a large air hole in the core.

the total internal reflection at the core-cladding boundary; another kind of PCF is called photonic band-gap (PBG) fiber that light is confined by the photonic band-gap which is generated by setting a periodic structure in the cladding region. A conventional HF, as shown in Fig. 2.1, has a triangular pattern of air holes with one hole missing, $i.e.$ with a solid core surrounded by an array of air holes. The region with the missing hole has a higher effective refractive index, similar to the core in a conventional fiber. Therefore, the total internal reflection at the core-cladding boundary exists. On the other hand, the PBG fiber, as shown in Fig. 2.2, which transmits the light through the central hole, has the characteristic of high intensity and low-loss transmission, and so on.

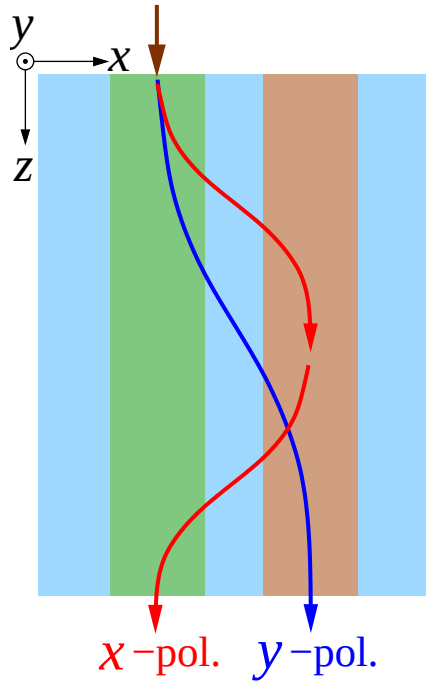

Figure 2.3: Schematic of PS which has a multi-core structure and achieves the polarization splitting by using the coupling length difference between x- and y-polarizations.

2.1.2 Polarization Splitter Based on PCF

In recent decades, most studies on PSs based on PCF have a multi-core distribution and achieve the polarization splitting by using the coupling length difference between x- and y-polarizations [64]-[74]. The schematic for this kind of PSs is shown in Fig. 2.3. With an incident light launched into the left core, utilizing the birefringence in each core, we note that the x- and y-polarized modes have different coupling lengths. When the power of x-polarization reaches a maximum in one waveguide, while the power of y-polarization also reaches a maximum in another waveguide, then the polarization splitting is achieved. However, for this kind of PS, it is difficult to realize cross-talk free with a wide bandwidth, therefore, the ER should be considered. For the left side waveguide in 2.3, the formula of ER can be given as,

$$\mathrm{ER} = 10\log_{10}\frac{\text{light power of } y\text{-polarization}}{\text{light power of } x\text{-polarization}}$$

Moreover, for this kind of PS, they generally suffers from a long device length due to considering the difference between two coupling lengths. PSs based on this

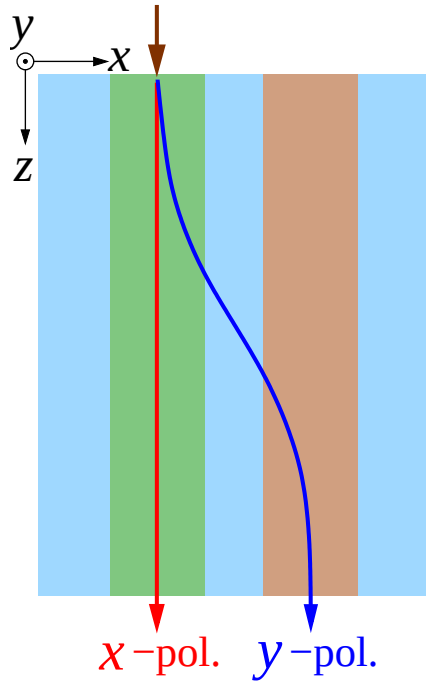

Figure 2.4: Schematic of PS which achieves the polarization splitting by coupling only one orthogonal polarized component.

mechanism are widely proposed [64]-[73], such as in [50], the authors proposed a polarization-dependent coupler based on twin-core PCF. Large and small holes are introduced to obtain a high birefringence in each hole. After being launched into the input core, a 45-degree linearly polarized light with Gaussian distribution experiences a quick splitting. Simulation results show that at the device length of 3.28 mm, two polarization modes are separated well. The ERs are 16.436 and 16.749 dB for x- and y-polarizations, respectively.

In addition, in order to obtain a PS with low ER, another kind of PS designed by coupling out only one orthogonal polarized component has been proposed, the schematic is shown in Fig. 2.4. Utilizing the birefringence in each core, the effective index of x-polarization is higher than the y-polarization in the left waveguide, while for the right waveguide, the effective index of y-polarization is higher than the x-polarization. Therefore, if the two waveguides are designed to satisfy the phase matching condition only for y-polarization, then with an incident light launched into the left waveguide, only the y-polarized component couples into the right waveguide, while the x-polarized component remains in the left waveguide

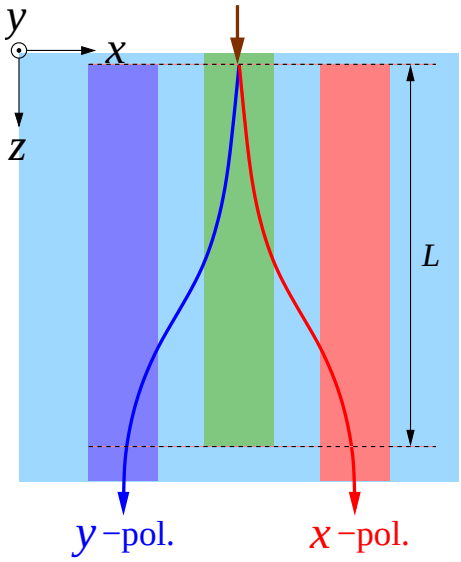

Figure 2.5: Schematic of our proposed PS with three single-polarized PCFs in parallel.

since the phase matching condition is not satisfied. We note that this kind of PS may has a shorter device length than the previous owning to only consider one coupling length. However, it requires a high precision in fabrication process. Slight variations are possibly cause the ER, such as the variation of the device length or structure parameters which leads the y-polarized component can not completely coupled out, especially the ER for left waveguide should be considered. Referring [57], the authors proposed a PS with a three-core PCF. Owing to the asymmetrical distributions in each core, highly birefringence exists, and the large effective index difference between x- and y-polarizations can be used for polarization selective devices. In order to achieve a low ER, authors using three core in parallel, by designing the satisfied structural parameters, only the x-polarized component of incident light in left waveguide coupled into the right waveguide, while y-polarized component remained in the left waveguide. Device length of this PS is $L = 1.93$ mm, and simulation results also illustrate that the ER is better than -20 dB with a bandwidth of 37 nm.

As expected, these two kinds of PS are difficult to achieve the cross-talk free, and the ER of each waveguide should be considered. In addition, according to the above design cases, we note that the design flexibility of PS is low, $e.g.$ large ER occurs if we slightly change the operation wavelength or vary the device length.

In summary, the ER is an important issue for an optical device. In order to overcome this issue, to obtain a cross-talk free device is the main objective for our research. Here, we proposed a novel PS by using three special single-polarized PCFs [62], [63]. The schematic of the PS is illustrated in Fig. 2.5. utilizing the absolutely single-polarization transmission of the special PCFs, when a beam of incident light launched into the input waveguide in the middle, the x- and y-polarized components will be separated and only coupled into the x- and y-polarized PCFs, respectively. We use the single polarization PCF as the output waveguide, $e.g.$ for a y-polarized PCF, only y-polarized component can be transmitted, while x-polarized component is not exist. According to the formula of ER, the ER of the y-polarized PCF is infinitely small, and cross-talk free is achieved. Moreover, if we change the operation wavelength or the device length, for the output waveguide the power coupling efficiency may not be 100%, but the output component is still single polarized, and the uncoupled component remains in the input waveguide which has no effect to the output waveguides. Thus, our proposed PS has a high design flexibility. We will explain the design of PS in chapter 4 in detail.

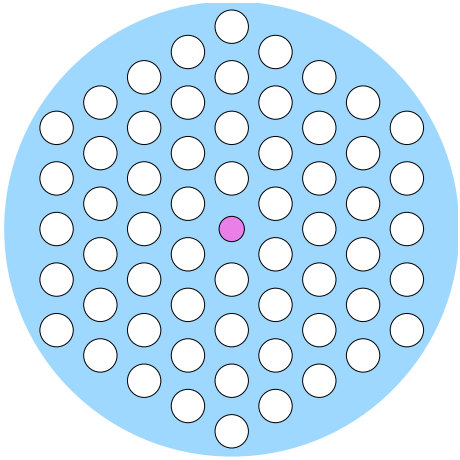

Figure 2.6: Schematic of PC element based on LC-PCF (Pink shaded area indicates the liquid crystal filled hole).

2.1.3 Polarization Converter Based on PCF

After we introduce the design of PS based on PCF, in this subsection, I would like to focus on the design of PC (also called polarization rotator) based on PCF. PCs have attracted the interest of many researchers in recent years due to their use in communication systems. So far, numerous studies on the PC that designed by using silicon-on-insulator (SOI) have been proposed [67]-[71]. On the other hand, the fiber type PC elements have also been widely studied, several designs of PC based on soft glass PCF with liquid crystal filled holes (LC-PCF) have been reported [72]-[74], the schematic is shown as Fig. 2.6. Utilizing the anisotropic character of liquid crystal, this kind of PCF PCs can enforce the coupling between the two fundamental polarization states. In 2010, M. F. O. Hameed *et al.* proposed a PC based on nematic LC-PCF, which has no central hole and provides a strong polarization conversion ratio of 99.81% with a device length of 1072 μm. Since all the air holes in the cladding are filled with the nematic liquid crystal, the nematic LC-PCF PC has a complex fabrication process. Moreover, in 2011, the same research team proposed a PC based on LC-PCF which has a central hole infiltrated with nematic liquid crystal [74]. At a wavelength of 1.55 μm, nearly 100% polarization conversion ratio is obtained, with a device length of 558 μm. However, the LC-PCF has a strong temperature dependence, and the cross-talk of LC-PCF PCs increases rapidly with the variation of temperature.

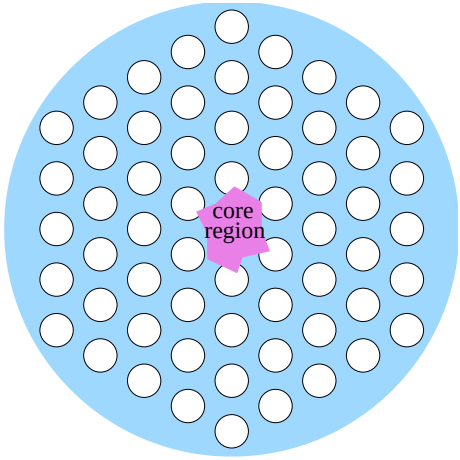

Figure 2.7: Schematic of PC element based on PCF with an anisotropic core.

In addition, instead of using LC-PCF, PC elements designed by using air hole PCF with an anisotropic core have also been investigated in recent years [75]-[77]. The schematic of this kind of PCF PCs is shown in Fig. 2.7, holes in cladding are arranged periodically that lead an isotropic cladding, while the asymmetric distribution in the core is used to obtain highly hybridness waveguide that can support the x- and y-polarization with nearly equal amplitude of magnetic field components. M. F. O. Hameed $et\ al.$ have reported a PC based on PCF with a L-shaped core region in 2012 [75]. All of the air holes arranged in a rectangular pattern and the asymmetric L-shaped core has a larger region along the vertical direction than that along the horizontal direction. Nearly 100% polarization conversion ratio with device length of 1743 μm can be achieve through this PC, and the ER is better than -20dB for the wavelength varies in the range of $1.55\ \mu\text{m} \pm 0.05\ \mu$m. After that, M. F. O. Hameed $et\ al.$ have also proposed a novel PC based on equiangular spiral PCF (ES-PCF). The proposed design relies on using ES-PCF with eight arms and an elliptical air hole in the core to obtain highly hybridness. The major axis of the elliptical hole is rotated by 45°, which offers 99% conversion ratio with device length of 96 μm. The cross-talk is better than -18dB for the wavelength varies in the range of $1.55\ \mu\text{m} \pm 0.05\ \mu$m. However, the equiangular spiral PCF requires a extremely precise manufacturing process.

According to the presentation above, it can be observed that the PCs based on PCF has a complex manufacturing process for the LC-PCF or the special PCF

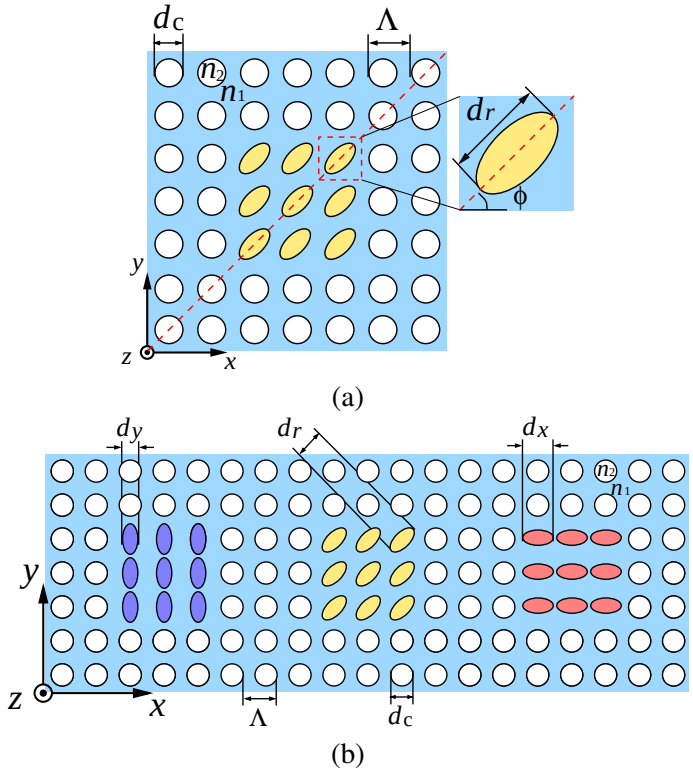

Figure 2.8: Our proposed PC element based on square lattice single-polarized PCF. Cross-sectional view of (a) single PC element and (b) cross-talk free three-core PC element.

distribution. Moreover the cross-talk of the PC element should also be considered. In this thesis, we proposed a novel single PC element based on single-polarized PCF which consists of square lattice air holes with a symmetrical distribution. Fig. 2.8(a) shows our proposed single PC element, since the structure has symmetry with respect to $y = x$, incident x- or y-polarized waves can be completely rotated $90°$. The single PC element can achieve polarization conversion with a compact conversion length of 31.7 μm and the ER is better than -23dB. In order to realize the cross-talk free device, two single-polarized PCFs are added at both sides of the PC waveguide to ensure that the input and output waves are absolutely single-polarized, as shown in Fig. 2.8(b). The three-core PC element provides a 99.1% conversion ratio with device length of 1550 μm. We will explain the design of PC in chapter 5 in detail.

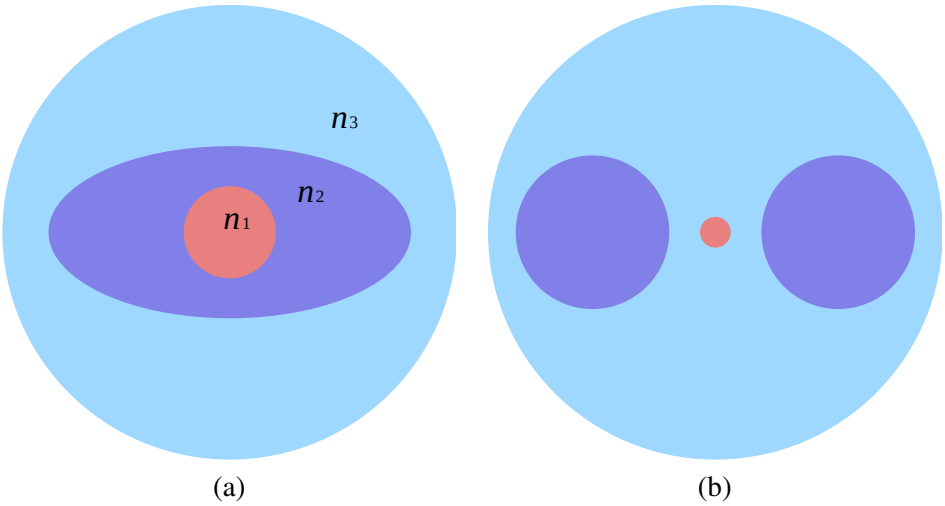

Figure 2.9: SPSM optical fibers based on conventional fibers. Schematic of (a) SPSM fiber using elliptical cladding and (b) PANDA fiber.

2.2 Absolutely Single-Polarization Single-Mode PCF

In this section, we will illustrate the single-polarization single-mode (SPSM) holey fibers. After that, among these SPSM HFs, we will focus on an special HF which has elliptical holes in the core, as known as EC-CHF. Finally, two kinds of EC-CHFs that we used in this research with different arrangement are illustrated.

2.2.1 SPSM Optical Fibers

So far, the basic method of designing an absolutely single-polarization optical fiber is introducing anisotropy into the core or the cladding region, then utilizing the cut-off wavelength difference between x- and y-polarization to ensure that only one polarization exist. Several different designs of single-polarization optical fibers using a conventional fiber have been proposed [23], [24]. The fiber may be geometrically asymmetric or have a refractive index profile which is asymmetric such as the design using an elliptical cladding, as shown in Fig. 2.9(a). Alternatively, stress birefringence can be produced by inducing the stress permanently in the fiber, such as PANDA Fiber, as shown in Fig. 2.9(b).

After the PCF has been proposed, numbers of single-polarization PCFs have been studied and proposed [26]-[41]. Fig. 2.10 illustrates four types of typical

SPSM PCFs. Fig. 2.10(a) shows the structure of first proposed SPSM PCF which has large circular air holes at the top and bottom of the core to obtain an asymmetrical arrangement. Utilizing the cut-off wavelength difference between x- and y-polarization to achieve the absolutely single-polarization. Fig. 2.10(b) shows a stress-imparting SPSM PCF [29] based on different thermal expansion coefficients of different materials. Like PANDA fiber, in this kind of SPSM PCF, birefringence can be obtained by appropriately designing the stress-applying part around the core. Fig. 2.10(c) and (d) give the SPSM PCFs with elliptical holes in the core or the cladding region. Large birefringence can be obtained by introducing elliptical holes in the core region, and this kind of PCF is known as elliptical-hole core circular-hole holey fiber [35]. Since the effective index of fundamental space-filling mode (FSM) of the core is anisotropic, large effective index difference between the slow wave and the fast wave is occurred. If the effective index of isotropic cladding region is set between that of the slow wave and fast wave, the EC-CHF for only propagating slow wave can be easily designed. On the contrary, SPSM PCF with elliptical holes in the cladding region [38] has also been proposed in 2009 with almost the same design principle.

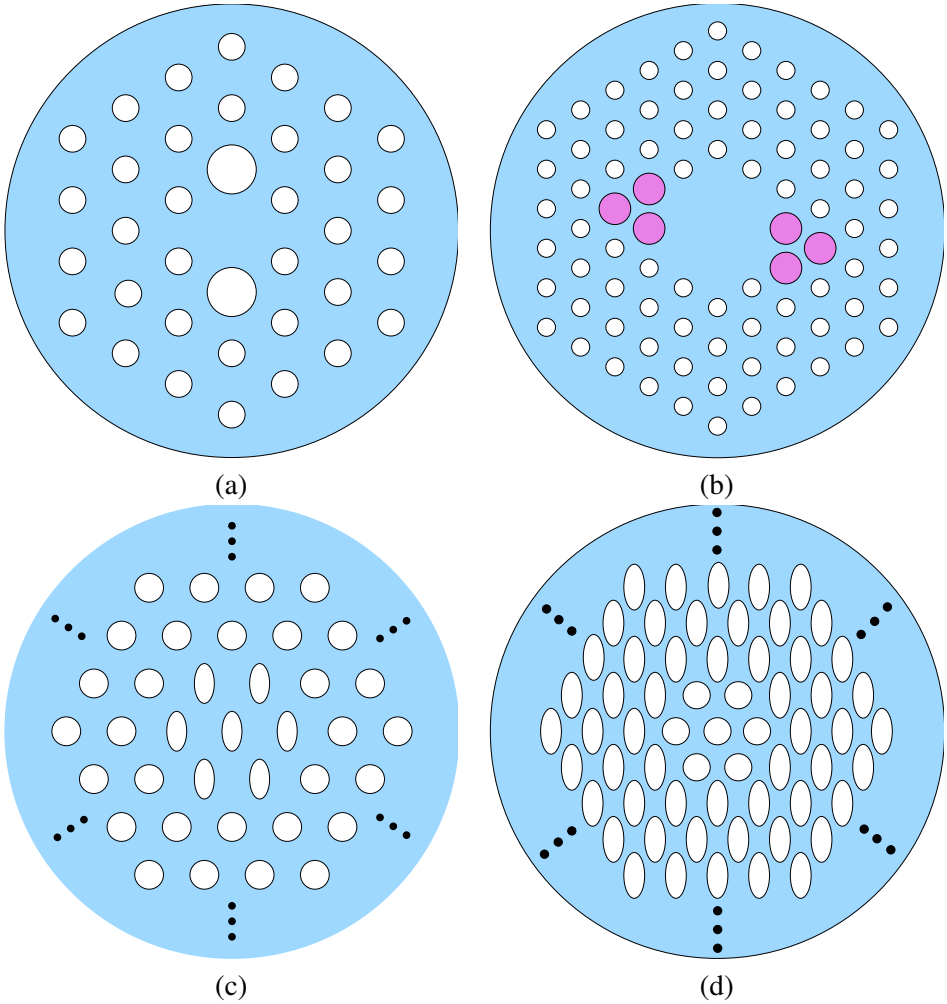

Figure 2.10: SPSM optical fibers based on PCFs. Schematic of (a) SPSM PCF with asymmetrical core, (b) stress-imparting SPSM PCF, (c) EC-CHF, (d) SPSM PCF with elliptical holes in the cladding.

2.2.2 Triangular Lattice EC-CHF

As we mentioned in the previous subsection, PCF with elliptical holes in the core region leads a large birefringence, with appropriate designed circular holes in the cladding, single-polarization transmission can be easily obtained. A three-dimensional structure of EC-CHF is shown in Fig. 2.11. In our research, we propose and design a novel PS element based on triangular lattice EC-CHFs. Utilizing the absolutely single-polarization property of EC-CHFs, cross-talk free PS can be designed.

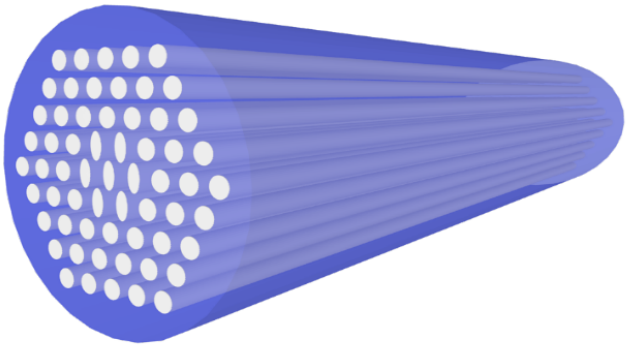

Figure 2.11: 3-dimensional structure of an EC-CHF.

As we know, a conventional HF has a sixfold symmetry and has an isotropic in the core region, as shown in Fig. 2.12(a). From the effective refractive index distribution of the HF shown in Fig. 2.12(b), we can observe that the FSM of core region (both x- and y-polarizations) is higher than that of the cladding region, $i.e.$ both x- and y-polarized components can be transmitted through this HF. Birefringence can be obtained by introducing elliptical air holes in the core region and the cross section of an EC-CHF with one ring core is shown in Fig. 2.12(c). The effective refractive index distribution of the EC-CHF is shown in Fig. 2.12(d). For the y-polarized wave, compared with the cladding region, the core region has a higher effective refractive index of FSM. On the other hand, for the x-polarized wave, the core region has the lower effective refractive index of FSM. Therefore, the single-polarization transmission can be achieved. This kind of EC-CHF is referred to as a yEC-CHF due to the major axis of elliptical hole is aligned along the y direction. A yEC-CHF can only transmit the y-polarized wave, and in the same way, an xEC-CHF, whose major axis of elliptical holes is aligned along the x direction, can only transmit the x-polarized wave, as shown in Fig. 2.12(e). In addition, if the core region of an EC-CHF is formed by circular hole, whose diameter is smaller than the circular hole in the cladding, has no polarization dependence and both of the x- and y-polarized waves can be transmitted. Here, we refer to it as a circular-hole core circular-hole holey fiber (CC-CHF), as shown in Fig. 2.12(g).

2.2.3 Square Lattice EC-CHF

In this thesis, we will design the cross-talk free PS by using triangular lattice EC-CHFs in chapter 4. In addition, in chapter 5 and 6, we will focus on the design of PC and MCS based on square lattice EC-CHFs, respectively. Since our proposed PC element requires a symmetrical arrangement, PC with triangular lattice EC-CHF is difficult to achieve the symmetrical structure, therefore, square lattice EC-CHFs are used to design the cross-talk free PC element. The cross sectional views of three kinds of EC-CHFs (yEC-CHF, xEC-CHF and CC-CHF) with square lattice arrangement are illustrated in Fig. 2.13. Owing to the symmetry property of the square lattice, a yEC-CHF can easily convert into an xEC-CHF by rotating it 90 degree. The effective refractive index distribution of each EC-CHF is the same as triangular lattice EC-CHFs.

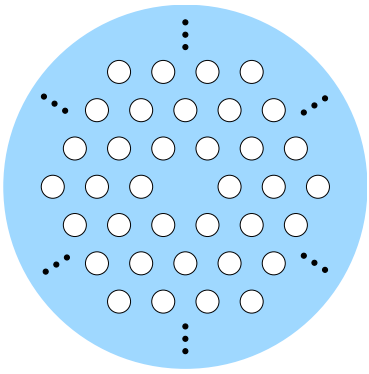

(a) Conventional HF

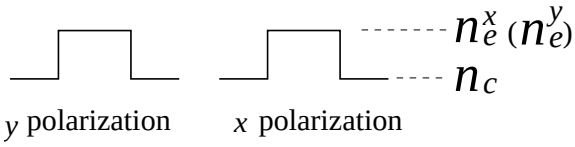

(b) Effective refractive index distribution

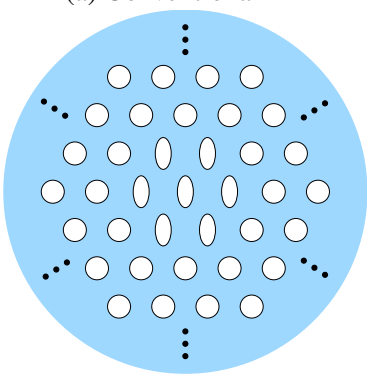

(c) yEC-CHF

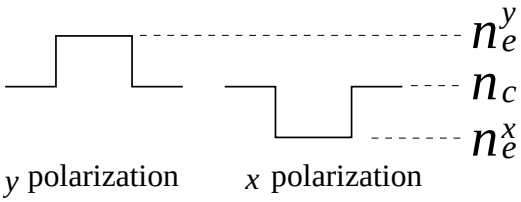

(d) Effective refractive index distribution

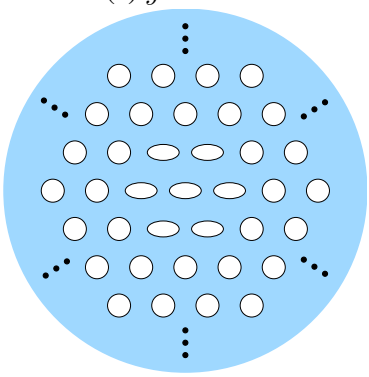

(e) xEC-CHF

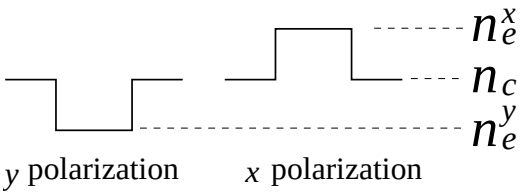

(f) Effective refractive index distribution

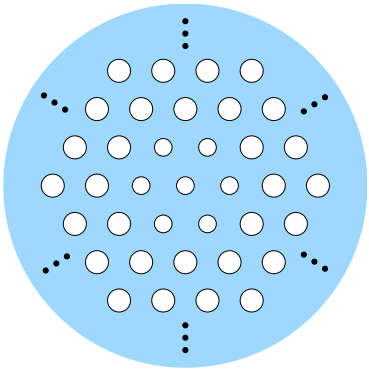

(g) CC-CHF

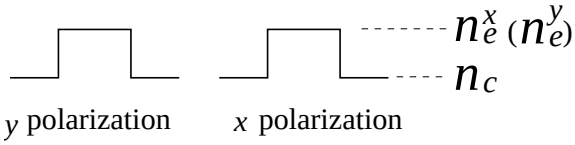

(h) Effective refractive index distribution

Figure 2.12: (a) Conventional HF, (c) yEC-CHF, (e) xEC-CHF and (g) CC-CHF and their corresponding effective refractive index distributions.

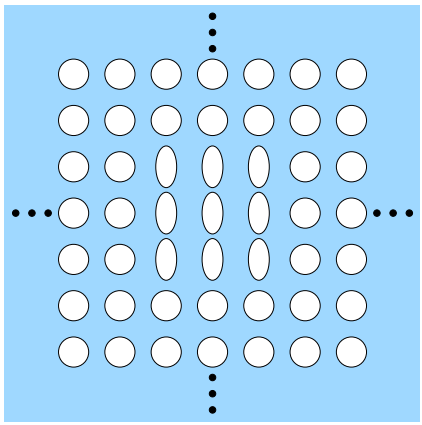

(a) yEC-CHF

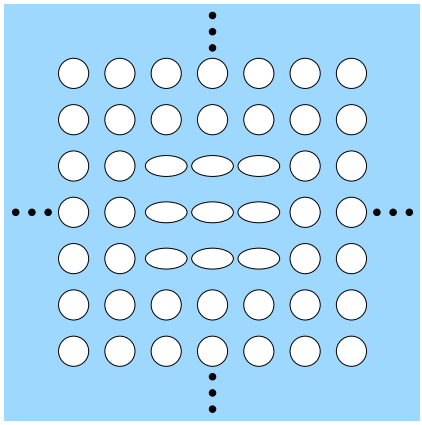

(b) xEC-CHF

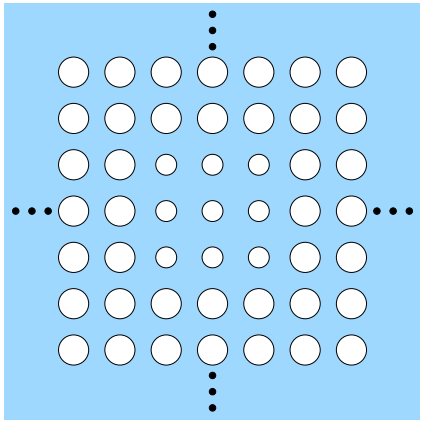

(c) CC-CHF

Figure 2.13: Cross sectional view of square lattice (a) yEC-CHF, (b) xEC-CHF and (c) CC-CHF.

Chapter 3

Vectorial Finite Element Method for PCF

In this chapter, we will focus on the analysis method for PCF in our research. In order to design a single-polarized PCF, the equivalent refractive indices of the core and cladding regions should be investigated. Since PCFs have a more complex structure than conventional optical fibers, the FEM, which has an excellent adaptability to any structure, is adopted to analyze the guided modes of our proposed optical devices. Here, in order to obtain the waveguide mode analysis and beam propagation analysis with a high accuracy, the FV-FEM using curvilinear hybrid edge/nodal element is used to analyze the cross section of the PCF. In this chapter, firstly, we will show the formulation of guided mode analysis for the PCF. Then, the formulation of BPM will be shown for analyzing the light propagation behaviors in our proposed optical devices. Finally, in order to obtained the equivalent waveguide of an EC-CHF, we will introduce the FSM of core and cladding region of an EC-CHF.

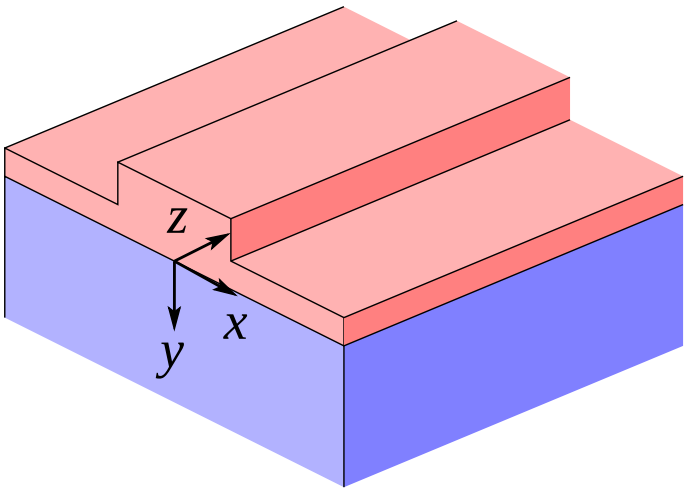

Figure 3.1: Three-dimensional optical waveguide.

3.1 Guided Mode Analysis

We consider a three-dimensional optical waveguide with a uniform structure along the z-direction. Light is confined in the xy plane and propagated along the z-direction, as shown in Fig. 3.1. Utilizing the electric field $\boldsymbol{E}$ and the magnetic field $\boldsymbol{H}$, Maxwell equations of the waveguide with isotropic materials can be expressed as follows:

$$\nabla \times \boldsymbol{E} = -j\omega\mu_0\mu_r\boldsymbol{H} \tag{3.1}$$

$$\nabla \times \boldsymbol{H} = j\omega\varepsilon_0\varepsilon_r\boldsymbol{E} \tag{3.2}$$

where ω is the angular frequency of the light wave, ε_0 and μ_0 are the permittivity and permeability in vacuum, respectively, ε_r and μ_r are the relative permittivity and relative permeability of the material, respectively. By multiplying both sides of (3.1) by μ_r^{-1}, then applying the curl to both sides of (3.1), we obtain

$$\nabla \times (\mu_r^{-1}\nabla \times \boldsymbol{E}) = -j\omega\mu_0\nabla \times \boldsymbol{H}. \tag{3.3}$$

By substituting this result into (3.2), we obtain a wave equation with only electric field $\boldsymbol{E}$, as follows:

$$\nabla \times (\mu_r^{-1}\nabla \times \boldsymbol{E}) - \omega^2\varepsilon_0\varepsilon_r\mu_0\boldsymbol{E} = 0. \tag{3.4}$$

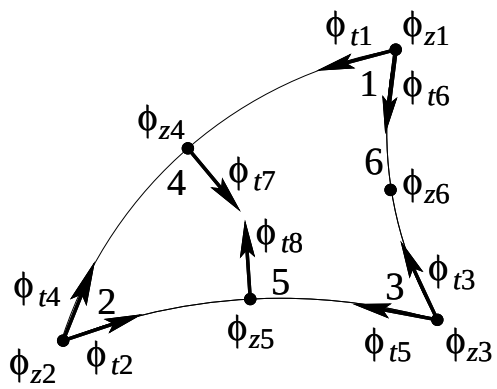

Figure 3.2: Triangular edge/nodal hybrid curved element.

Similarly, wave equation with only magnetic field $\boldsymbol{H}$ can also be obtained from (3.1) and (3.2), as follows:

$$\nabla \times (\varepsilon_r^{-1} \nabla \times \boldsymbol{H}) - \omega^2 \varepsilon_0 \mu_0 \mu_r \boldsymbol{H} = 0. \tag{3.5}$$

By considering (3.4) and (3.5), the vector wave equation from Maxwell's equations for describing the propagation light can be expressed in a unified form as follows:

$$\nabla \times ([p] \nabla \times \boldsymbol{\Phi}) - k_0^2 [q] \boldsymbol{\Phi} = \boldsymbol{0}. \tag{3.6}$$

where $k_0 = \omega\sqrt{\varepsilon_0 \mu_0}$ is the wavenumber in vacuum, $[p]$ and $[q]$ are determined by whether the function $\boldsymbol{\Phi}$ is regarded as electric field $\boldsymbol{E}$ or magnetic field $\boldsymbol{H}$, and the conditions are shown as follows:

$$\begin{aligned} [p] = [\mu]^{-1},\ [q] = [\varepsilon] \quad & \text{for } \boldsymbol{\Phi} = \boldsymbol{E} \\ [p] = [\varepsilon]^{-1},\ [q] = [\mu] \quad & \text{for } \boldsymbol{\Phi} = \boldsymbol{H}. \end{aligned}$$

The functional for this wave equation is

$$F = \iint [(\nabla \times \boldsymbol{\Phi}^*) \cdot ([p] \nabla \times \boldsymbol{\Phi}) - k_0^2 \boldsymbol{\Phi}^* \cdot ([q]) \boldsymbol{\Phi}] dxdy. \tag{3.7}$$

Considering the optical waveguide shown in Fig. 3.1, which has no structural variation along the z axis, the eigenmode of light propagates has the same propagation constant β along the z direction. In this case, dividing the xy cross-section by using the triangular edge/nodal hybrid curved element [85], as shown in Fig.

3.2, the field vector $\mathbf{\Phi}$ in each element can be expressed as follows:

$$\mathbf{\Phi} = \begin{bmatrix} \{U\}^T \{\phi_t\} \\ \{V\}^T \{\phi_t\} \\ j\beta \{N\}^T \{\phi_z\} \end{bmatrix} \exp(-j\beta z) = \begin{bmatrix} \{U\}^T & \{0\}^T \\ \{V\}^T & \{0\}^T \\ \{0\}^T & j\beta \{N\}^T \end{bmatrix} \begin{bmatrix} \{\phi_t\} \\ \{\phi_z\} \end{bmatrix} \exp(-j\beta z), \quad (3.8)$$

where $\{U\}$ and $\{V\}$ are the shape functions corresponding to the x and y components of each edge element, respectively. The corresponding shape function of nodal element is represented by $\{N\}$. Substituting (3.8) into (3.7), the second term of the integrand in (3.7) can be represented as,

$$\begin{aligned} -k_0^2 \mathbf{\Phi}^* \cdot ([q]\mathbf{\Phi}) = -k_0^2 \left[\{\phi_t\}^T \ \{\phi_z\}^T \right] & \begin{bmatrix} \{U\} & \{V\} & \{0\} \\ \{0\} & \{0\} & -j\beta \{N\} \end{bmatrix} \\ \times \begin{bmatrix} q_{xx} & q_{xy} & q_{xz} \\ q_{yx} & q_{yy} & q_{yz} \\ q_{zx} & q_{zy} & q_{zz} \end{bmatrix} & \begin{bmatrix} \{U\}^T & \{0\}^T \\ \{V\}^T & \{0\}^T \\ \{0\}^T & j\beta \{N\}^T \end{bmatrix} \begin{bmatrix} \{\phi_t\} \\ \{\phi_z\} \end{bmatrix}. \end{aligned} \quad (3.9)$$

In our research, we consider isotropic materials in all the proposed devices. Therefore, $[q]$ in the equation above can be written as

$$\begin{bmatrix} q_{xx} & q_{xy} & q_{xz} \\ q_{yx} & q_{yy} & q_{yz} \\ q_{zx} & q_{zy} & q_{zz} \end{bmatrix} = q \begin{bmatrix} 1 & 0 & 0 \\ 0 & 1 & 0 \\ 0 & 0 & 1 \end{bmatrix}.$$

Integrating the both sides of the equation (3.9) for each element, and superimposing on all the elements, we can obtain the following relation:

$$\begin{aligned} \iint -k_0^2 \mathbf{\Phi}^* \cdot ([q]\mathbf{\Phi}) dxdy = & \left[\{\phi_t\}^T \ \{\phi_z\}^T \right] \\ \times \left(\begin{bmatrix} \left[Q_{tt}^{(0)}\right] & [0] \\ [0] & [0] \end{bmatrix} - \beta^2 \begin{bmatrix} [0] & [0] \\ [0] & \left[Q_{zz}^{(2)}\right] \end{bmatrix} \right) & \begin{bmatrix} \{\phi_t\} \\ \{\phi_z\} \end{bmatrix}. \end{aligned} \quad (3.10)$$

For the first term of the integrand in (3.7), $\nabla \times \mathbf{\Phi}$ is expressed as follows:

$$\begin{aligned} \nabla \times \mathbf{\Phi} &= \begin{bmatrix} 0 & j\beta & \frac{\partial}{\partial y} \\ -j\beta & 0 & -\frac{\partial}{\partial x} \\ -\frac{\partial}{\partial y} & \frac{\partial}{\partial x} & 0 \end{bmatrix} \begin{bmatrix} \{U\}^T & \{0\}^T \\ \{V\}^T & \{0\}^T \\ \{0\}^T & j\beta \{N\}^T \end{bmatrix} \begin{bmatrix} \{\phi_t\} \\ \{\phi_z\} \end{bmatrix} \\ &= \begin{bmatrix} j\beta \{V\}^T & j\beta \{N_y\}^T \\ -j\beta \{U\}^T & -j\beta \{N_x\}^T \\ -\{U_y\}^T + \{V_x\}^T & \{0\}^T \end{bmatrix} \begin{bmatrix} \{\phi_t\} \\ \{\phi_z\} \end{bmatrix}. \end{aligned} \quad (3.11)$$

Based on the representation in (3.11), the first term of the integrand is given as follows:

$$(\nabla \times \mathbf{\Phi}^*)\cdot([p]\nabla \times \mathbf{\Phi}) = \left[\{\phi_t\}^T \ \{\phi_z\}^T\right] \begin{bmatrix} -j\beta\{V\} & j\beta\{U\} & -\{U_y\}+\{V_x\} \\ -j\beta\{N_y\} & j\beta\{N_x\} & \{0\} \end{bmatrix}$$
$$\times \begin{bmatrix} p_{xx} & p_{xy} & p_{xz} \\ p_{yx} & p_{yy} & p_{yz} \\ p_{zx} & p_{zy} & p_{zz} \end{bmatrix} \begin{bmatrix} j\beta\{V\}^T & j\beta\{N_y\}^T \\ -j\beta\{U\}^T & -j\beta\{N_x\}^T \\ -\{U_y\}^T+\{V_x\}^T & \{0\} \end{bmatrix} \begin{bmatrix} \{\phi_t\} \\ \{\phi_z\} \end{bmatrix}, \quad (3.12)$$

where $\{V_x\}$ and $\{U_y\}$ represent the partial differential of $\{V\}$ and $\{U\}$, as follows:

$$\{V_x\} = \frac{\partial\{V\}}{\partial x}, \quad \{U_x\} = \frac{\partial\{U\}}{\partial y}.$$

Similarly, $\{N_x\}$ and $\{N_y\}$ represent the partial differential of $\{N\}$ with respect to x and y, respectively. Here, considering isotropic materials, the matrix $[p]$ can be rewritten as

$$\begin{bmatrix} p_{xx} & p_{xy} & p_{xz} \\ p_{yx} & p_{yy} & p_{yz} \\ p_{zx} & p_{zy} & p_{zz} \end{bmatrix} = p \begin{bmatrix} 1 & 0 & 0 \\ 0 & 1 & 0 \\ 0 & 0 & 1 \end{bmatrix}.$$

Integrating both sides of the equation (3.12) for each element, and superimposing on all the elements, we can obtain the following relation:

$$\iint (\nabla \times \mathbf{\Phi}^*)\cdot([p]\nabla \times \mathbf{\Phi})dxdy = \left[\{\phi_t\}^T \ \{\phi_z\}^T\right]$$
$$\times \left(\begin{bmatrix} \begin{bmatrix} R_{tt}^{(0)} \end{bmatrix} & [0] \\ [0] & [0] \end{bmatrix} - \beta^2 \begin{bmatrix} \begin{bmatrix} R_{tt}^{(2)} \\ R_{zt}^{(2)} \end{bmatrix} & \begin{bmatrix} R_{tz}^{(2)} \\ R_{zz}^{(2)} \end{bmatrix} \end{bmatrix} \right) \begin{bmatrix} \{\phi_t\} \\ \{\phi_z\} \end{bmatrix}. \quad (3.13)$$

In our research, since we employ the isotropic material to consist all the optical devices, the matrices $[Q_{ij}^{(k)}]$ and $[R_{ij}^{(k)}]$ $(i, j = t, z,\ k = 0, 1, 2)$ in (3.10) and (3.13)

are represented as follows:

$$[Q_{tt}^{(0)}] = \sum_e \iint_e -k_0^2 q(\{U\}\{U\}^T + \{V\}\{V\}^T) d\Omega \tag{3.14}$$

$$[Q_{zz}^{(2)}] = \sum_e \iint_e k_0^2 q\{N\}\{N\}^T d\Omega \tag{3.15}$$

$$[R_{tt}^{(0)}] = \sum_e \iint_e p(\{V_x\} - \{U_y\}) \left(\{V_x\}^T - \{U_y\}^T\right) dxdy \tag{3.16}$$

$$[R_{tt}^{(2)}] = \sum_e \iint_e -p(\{V\}\{V\}^T + \{U\}\{U\}^T) dxdy \tag{3.17}$$

$$[R_{tz}^{(2)}] = [R_{zt}^{(2)}]^T = \sum_e \iint_e -p(\{V\}\{N_y\}^T + \{U\}\{N_x\}^T) dxdy \tag{3.18}$$

$$[R_{zz}^{(2)}] = \sum_e \iint_e -p(\{N_y\}\{N_y\}^T + \{N_x\}\{N_x\}^T) dxdy \tag{3.19}$$

Therefore, taking the variation of (3.7) under the condition of the eigenmode propagation, the final equation can be expressed as follows:

$$([K] - \beta^2[M])\{\phi\} = 0, \tag{3.20}$$

where $[K]$ and $[M]$ are generally referred to as the stiffness matrix and mass matrix, respectively. They are expressed as:

$$[K] = \begin{bmatrix} [K_{tt}] & [0] \\ [0] & [0] \end{bmatrix} \tag{3.21}$$

$$[M] = \begin{bmatrix} [M_{tt}] & [M_{tz}] \\ [M_{zt}] & [M_{zz}] \end{bmatrix} \tag{3.22}$$

$$\{\phi\} = \begin{bmatrix} \{\phi_t\} \\ \{\phi_z\} \end{bmatrix} \tag{3.23}$$

The $[K_{ij}]$ and $[M_{ij}]$ $(i, j = t, z)$ are given as follows:

$$
\begin{aligned}
[K_{tt}] &= -[Q_{tt}^{(0)}] - [R_{tt}^{(0)}] \\
&= \sum_e \iint_e [k_0^2 q(\{U\}\{U\}^T + \{V\}\{V\}^T) \\
&\quad - p(\{V_x\} - \{U_y\})(\{V_x\}^T - \{U_y\}^T)]dxdy \qquad (3.24)
\end{aligned}
$$

$$
[M_{tt}] = -[R_{tt}^{(2)}] = \sum_e \iint_e p(\{V\}\{V\}^T + \{U\}\{U\}^T)dxdy \qquad (3.25)
$$

$$
[M_{tz}] = -[R_{tz}^{(2)}] = \sum_e \iint_e p(\{V\}\{N_y\}^T + \{U\}\{N_x\}^T)dxdy \qquad (3.26)
$$

$$
[M_{zt}] = [M_{tz}]^T \qquad (3.27)
$$

$$
\begin{aligned}
[M_{zz}] &= -[Q_{zz}^{(2)}] - [R_{zz}^{(2)}] \\
&= \sum_e \iint_e [-k_0^2 q(\{N\}\{N\}^T + p(\{N_y\}\{N_y\}^T + \{N_x\}\{N_x\}^T)]dxdy. \qquad (3.28)
\end{aligned}
$$

By solving the generalized eigenvalue equation (3.20), the propagation constant β and the electromagnetic field distribution $\{\phi\}$ with a given wavelength can be obtained.

3.2 Formulation of Beam Propagation Method

In this section, based on the generalized eigenvalue equation obtained previously, we will give the formulation of the BPM. Firstly, we give the BPM formulation based on the paraxial equation. However, this formulation can be used only when the inclination angle is relatively small with respect to the z-axis. Then the BPM formulation based on the Helmholtz equation is given for analyzing the beam propagation with a wide angle. Moreover, we also show the BPM formulation based on the Padé expression.

3.2.1 BPM Formulation with Paraxial Equation

According to the generalized eigenvalue equation (3.20), the basic equation of beam propagation analysis can be fixed as the following equation by using $\beta \rightarrow j\frac{d}{dz} + k_0 n_0$.

$$([K] - \beta^2[M])\{\phi\} = 0 \rightarrow \left[[K] - \left(k_0^2 n_0^2 + 2jk_0 n_0 \frac{d}{dz} - \frac{d^2}{dz^2}\right)[M]\right]\{\phi\} = \{0\}. \tag{3.29}$$

It can be also written as,

$$[M]\frac{d^2\{\phi\}}{dz^2} - 2jk_0 n_0 [M]\frac{d\{\phi\}}{dz} + ([K] - k_0^2 n_0^2 [M])\{\phi\} = \{0\}. \tag{3.30}$$

When the amplitude of a waveguide varies slowly along z direction, $i.e.$,

$$\frac{\partial}{\partial z} \ll -j2k_0 n_0 \tag{3.31}$$

the slowly varying envelope approximation (SVEA) of the waveguide is concluded, and the paraxial equation can be obtained, as shown as follows:

$$-2jk_0 n_0 [M] \frac{d\{\phi\}}{dz} + \left([K] - k_0^2 n_0^2 [M]\right)\{\phi\} = \{0\} \tag{3.32}$$

where $d\{\phi\}/dz$ and $\{\phi\}$ can be represented as follows using the differential along z direction with θ scheme.

$$\frac{d\{\phi\}}{dz} = \frac{\{\phi\}_{i+1} - \{\phi\}_i}{\Delta z}, \tag{3.33}$$

$$\{\phi\} = \theta\{\phi\}_{i+1} + (1-\theta)\{\phi\}_i. \tag{3.34}$$

Here, Δz is the step size along propagation direction, the subscripts i and $i+1$ represent the i-th and $(i+1)$-th quantities related to the propagation step, respectively. Therefore, the (3.32) can be rewritten as

$$-2jk_0n_0\ [M]_{i+\frac{1}{2}}\frac{\{\phi\}_{i+1}-\{\phi\}_i}{\Delta z}+\left([K]_{i+\frac{1}{2}}-k_0^2n_0^2\,[M]_{i+\frac{1}{2}}\right)$$
$$\{\theta\{\phi\}_{i+1}+(1-\theta)\{\phi\}_i\}=\{0\}. \tag{3.35}$$

Finally, the sequential updating equation along z direction can be obtained as follows:

$$[A]_{i+\frac{1}{2}}\,\{\phi\}_{i+1}=[B]_{i+\frac{1}{2}}\,\{\phi\}_i, \tag{3.36}$$

where $[A]_i$ and $[B]_i$ are

$$[A]_i=-2jk_0n_0\,[M]_i+\theta\Delta z\left([K]_i-k_0^2n_0^2\,[M]_i\right), \tag{3.37}$$
$$[B]_i=-2jk_0n_0\,[M]_i+(\theta-1)\Delta z\left([K]_i-k_0^2n_0^2\,[M]_i\right). \tag{3.38}$$

For an incident light launched into initial waveguide is determined as $\{\phi\}_0$, the propagation of the light wave can be calculated by computing (3.36) sequentially.

3.2.2 BPM Formulation with Helmholtz Equation

For the formulation based on the paraxial equation in the previous subsection, it is not satisfied to the situations such as the waveguide is greatly inclined from the propagation direction, or in the case of the radiation wave increase. Therefore, in this subsection, we formulate the second-order difference in (3.30) by using the Newmark-β method to analyze the wide-angle beam propagation. Here, $d^2\{\phi\}/dz^2$, $d\{\phi\}/dz$ and $\{\phi\}$ are represented by

$$\frac{d\{\phi\}}{dz}=\frac{\{\phi\}_{i+1}-\{\phi\}_i}{\Delta z}, \tag{3.39}$$
$$\frac{d^2\{\phi\}}{dz^2}=\frac{\{\phi\}_{i+1}-2\{\phi\}_i+\{\phi\}_{i-1}}{\Delta z^2}, \tag{3.40}$$
$$\{\phi\}=\beta\{\phi\}_{i+1}+(1-2\beta)\{\phi\}_i+\beta\{\phi\}_{i-1}. \tag{3.41}$$

Finally, the sequential computing formula along z direction can be obtained as follows:

$$[A]_i\,\{\phi\}_{i+1}=2\,[C]_i\,\{\phi\}_i+[B]_i\,\{\phi\}_{i-1}, \tag{3.42}$$

where $[A]_i$, $[B]_i$ and $[C]_i$ are

$$[A]_i = (1 - 2jk_0n_0\Delta z)\,[M]_i + \beta\Delta z^2\left([K]_i - k_0^2n_0^2\,[M]_i\right), \tag{3.43}$$

$$[B]_i = (-1 - 2jk_0n_0)\,[M]_i - \beta\Delta z^2\left([K]_i - k_0^2n_0^2\,[M]_i\right), \tag{3.44}$$

$$[C]_i = [M]_i + (1 - 2\beta)\Delta z^2\left([K]_i - k_0^2n_0^2\,[M]_i\right). \tag{3.45}$$

Usually, β is used as $1/6$.

3.2.3 BPM Formulation with Padé Expression

The BPM formula with the Helmholtz equation mentioned above can be used to analyze the wide-angle beam propagation due to considering the second-order difference along the z direction. However, in order to determine the field of the next propagation step, the field of current and previous steps are required. This leads to a complicated calculation procedure. Moreover, when we update the finite element mesh along the z direction, since the number of interpolation for the field is increased, the analysis accuracy is degraded. In this subsection, we use the Padé expression along the z direction to obtain the BPM formula.

The equation (3.30) can be formally represented as

$$-2jk_0n_0\,[M]\,\frac{d\{\phi\}}{dz} = -\frac{\left([K] - k_0^2n_0^2[M]\right)\{\phi\}}{1 - \frac{1}{2jk_0n_0}\frac{d}{dz}}. \tag{3.46}$$

We can get the following recurrence formula with respect to the z direction.

$$\left.\frac{d}{dz}\right|_k = \frac{[M]^{-1}\left([K] - k_0^2n_0^2[M]\right)}{2jk_0n_0 - \left.\frac{d}{dz}\right|_{k-1}}. \tag{3.47}$$

Here, we approximate d/d_z to Padé (1,1), as follows:

$$\frac{d}{dz} \simeq \frac{1}{2jk_0n_0}[M]^{-1}\left([K] - k_0^2n_0^2[M]\right). \tag{3.48}$$

Equation (3.30) can be written as

$$-2jk_0n_0[\tilde{M}]\frac{d\{\phi\}}{dz} + \left([K] - k_0^2n_0^2\,[M]\right)\{\phi\} = \{0\}, \tag{3.49}$$

$$[\tilde{M}] = [M] + \frac{1}{4k_0^2n_0^2}\left([K] - k_0^2n_0^2[M]\right). \tag{3.50}$$

Equation (3.49) is obtained by replacing $[M]$ with $[\tilde{M}]$ from (3.32). The sequential updating equation based on Padé approximation is

$$[A]_{i+\frac{1}{2}} \{\phi\}_{i+1} = [B]_{i+\frac{1}{2}} \{\phi\}_i, \tag{3.51}$$

where $[A]_i$ and $[B]_i$ are

$$[A]_i = -2jk_0n_0[\tilde{M}]_i + \theta\Delta z \left([K]_i - k_0^2n_0^2 [M]_i\right), \tag{3.52}$$

$$[B]_i = -2jk_0n_0 [M]_i + (\theta - 1)\Delta z \left([K]_i - k_0^2n_0^2 [M]_i\right). \tag{3.53}$$

3.3 FSM of an EC-CHF

As we know, PCFs have attracted a lot of attentions in the last two decades due to their flexible structures and unique features. In index-guiding PCFs with a higher-index defect acting as the fiber core, such properties as endlessly single-mode operation and very large birefringence can be achieved [17], [18]. Many of these properties can be understood by a simple analogy with conventional optical fibers by the effective index model, where a PCF assumes an effective cladding index defined as the FSM [88]-[90] of the periodic cladding structure. Utilizing the FSM of cladding for a PCF and its effective index, it is possible to calculate confinement loss [91], bending loss [92], and to determine the single-mode region [19].

In our research, since the EC-CHF has two kinds of air holes, $i.\ e.$ elliptical holes in the core region and circular holes in the cladding, we design the single-polarized EC-CHF by using the effective indices of the FSM for the core and cladding region. Moreover, in order to design a cross-talk free PS element as mentioned in chapter 2, we design each waveguide by satisfying the phase matching condition. Instead of analyzing the complicated whole EC-CHF structure, we design the PS by using effective indices of the FSM in each waveguide, which is discussed in detail in chapter 4. For a triangular lattice EC-CHF, schematic of the infinitely periodic core lattice and the reduced cell which is used for numerical solution of FSM are shown in Fig. 3.3. Utilizing the structural symmetry, we can analyze the x-polarized FSM by setting the top and bottom boundaries of the reduced cell as the perfect magnetic conductor (PMC), and the left and right boundaries as the perfect electric conductor (PEC). On the contrary, when we analyze the y-polarized FSM, top and bottom boundaries are set to the PEC, and the left and right boundaries are set to the PMC. Moreover, if we replace the elliptical holes by circular holes in the cladding, then the FSM of cladding region can also been analyzed with the same boundary conditions.

In chapter 5 and 6, we design a PC element and a mode splitter based on square lattice EC-CHFs, respectively. In order to ensure the absolutely single-polarization propagation of a square lattice EC-CHF, the FSM of the core and cladding region should be considered. Schematic of the infinitely periodic core region for a square lattice EC-CHF and the reduced cell used for numerical solution are shown in Fig.

3.4. It can be observed that the reduced cell used for numerical solution is 1/4 of the unit cell due to the EC-CHF with square arrangement has a symmetrical property with respect to the horizontal and vertical directions. The reduced cell has the same boundary conditions as the triangular lattice EC-CHF.

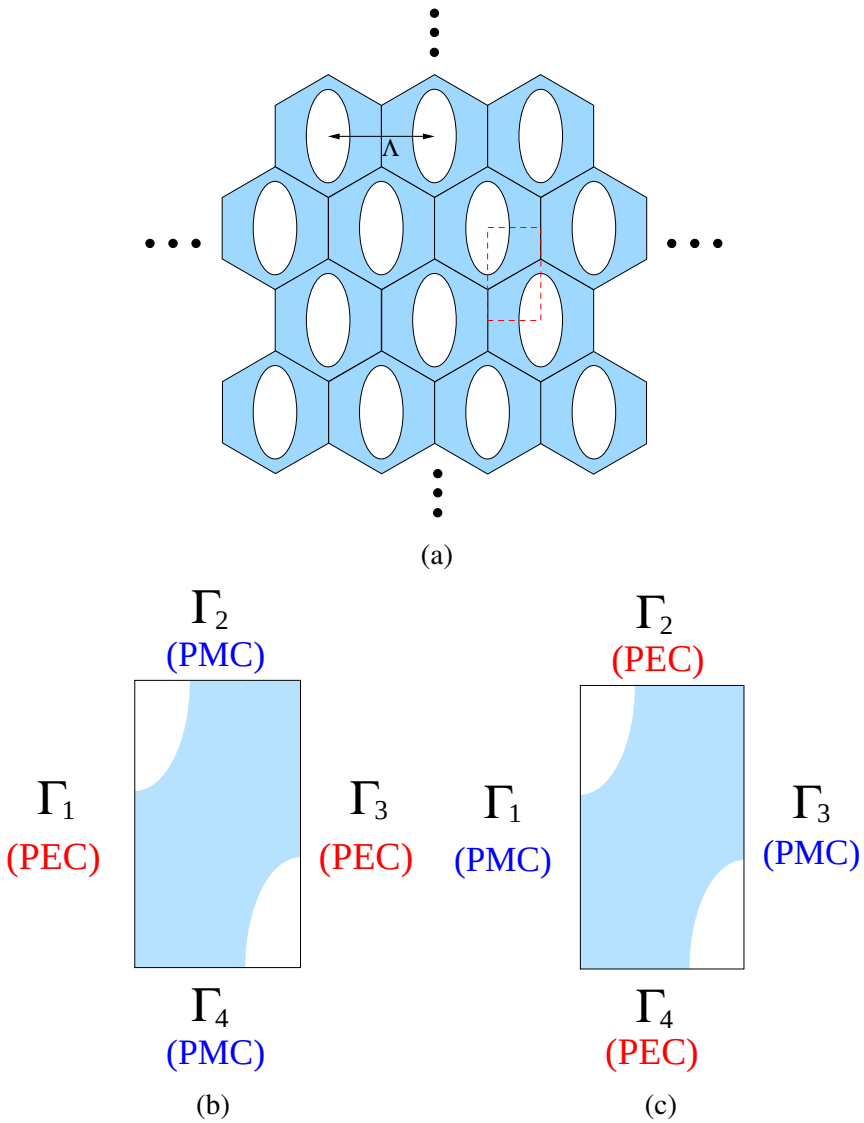

Figure 3.3: Schematic of (a) the infinitely periodic core lattice for a EC-CHF, and the reduced cell with different boundaries for analyzing (b) the x-polarization and (c) the y-polarization. Λ is the hole pitch, the red wire frame area is the reduced cell which is used for numerical solution of FSM.

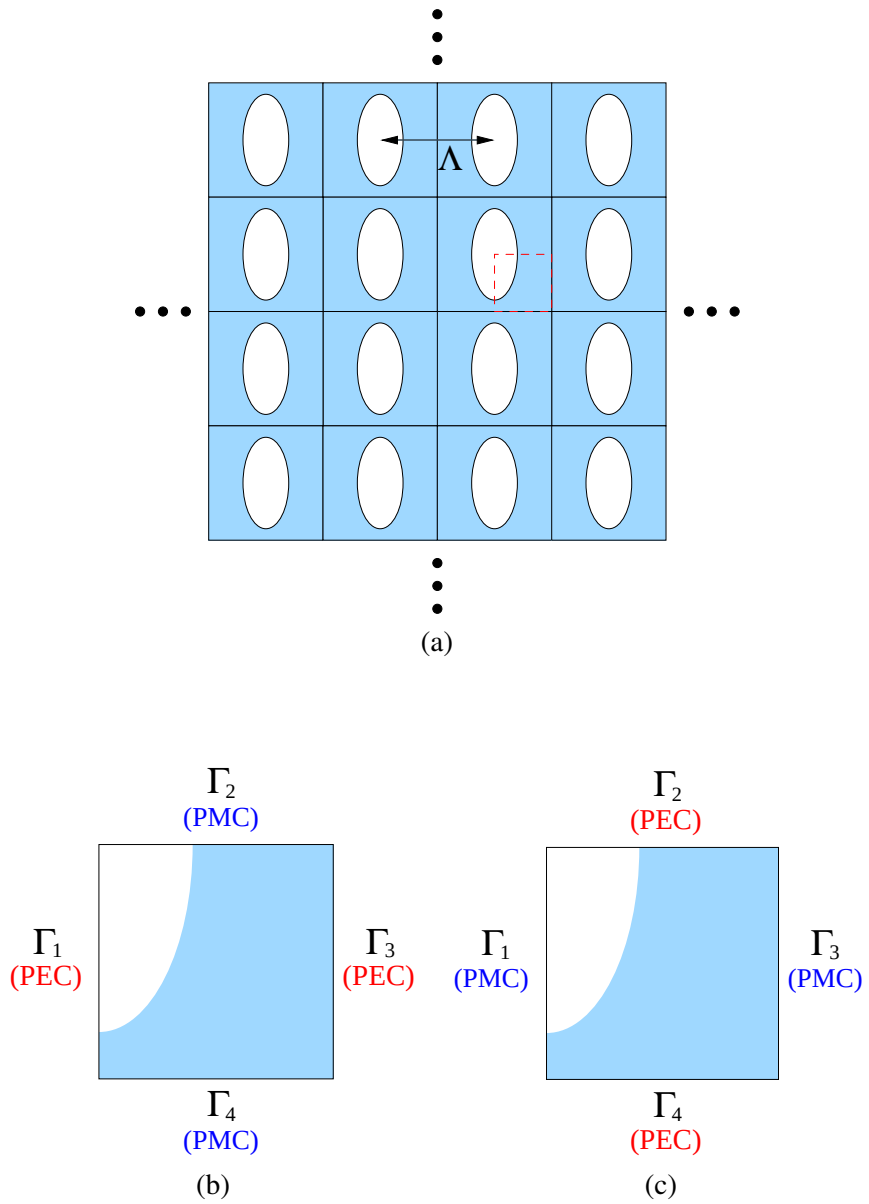

Figure 3.4: Schematic of (a) the infinitely periodic core region for a square lattice EC-CHF, and the reduced cell with different boundaries for analyzing (b) the x-polarization and (c) the y-polarization. Λ is the hole pitch, the red wire frame area is the reduced cell which is used for numerical solution of FSM.

Chapter 4

Cross-Talk Free Polarization Splitter

In this chapter, we design a novel cross-talk free PS based on triangular lattice EC-CHF. The 3 dimensional structure and cross sectional view are shown in Fig. 4.1 and Fig. 4.2, respectively. The device is consisted by three EC-CHFs in parallel, from left to right in order, a yEC-CHF, a CC-CHF, and an xEC-CHF. Using the FE-BPM, we demonstrated that an 45-degree polarized light can be completely divided into two orthogonally polarized waves. The x- and y-polarized components couple only to xEC-CHF and yEC-CHF, respectively. This phenomenon can be explained by the coupled mode theory.

As shown in Fig. 4.2, we design the cross-talk free PS by using three separated EC-CHFs. Here, we set the yEC-CHF as a reference waveguide, based on the coupled mode theory, we determine the other two EC-CHFs (xEC-CHF and CC-CHF) by satisfying the phase matching condition with the yEC-CHF. After that, the coupling lengths of the x- and y-polarization can be respectively estimated by setting an appropriate core interval between two adjacent cores. Finally, the device length is determined as the average of the two coupling lengths.

In this thesis, we present the design examples of our proposed PS with the large hole EC-CHFs (air filling fraction in core is 36.73%) and small hole EC-CHFs (air filling fraction in core is 4.08%). Moreover, in order to satisfy the phase matching condition between the yEC-CHF and the other two EC-CHFs (xEC-CHF and CC-CHF), we employ not only the effective index of each waveguide but also the FSM of the core region to design the PS efficiently, and the design accuracy of the FSM method has also been discussed in detail. Finally, the structure tolerance and wavelength dependence of our proposed PS have also been discussed.

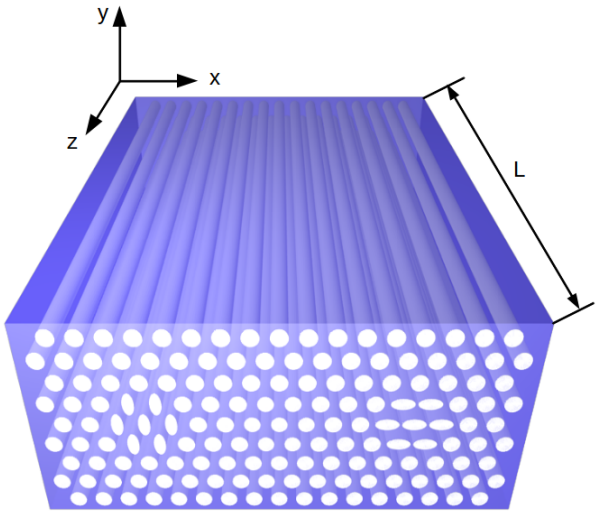

Figure 4.1: 3 dimensional structure of proposed PS based on triangular lattice EC-CHFs.

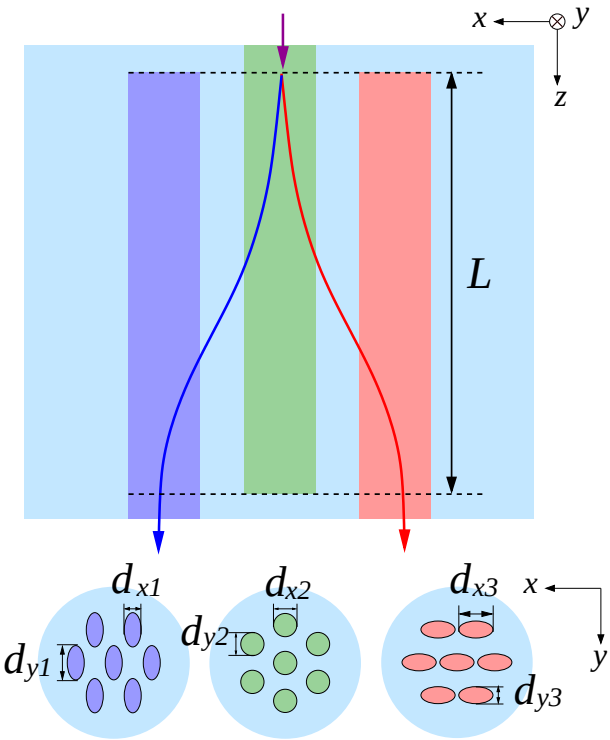

Figure 4.2: Structure of proposed PS based on triangular lattice EC-CHFs.

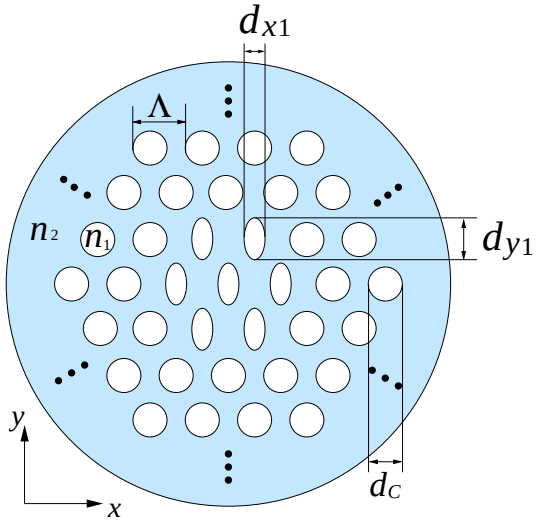

Figure 4.3: Cross sectional view of a triangular lattice yEC-CHF.

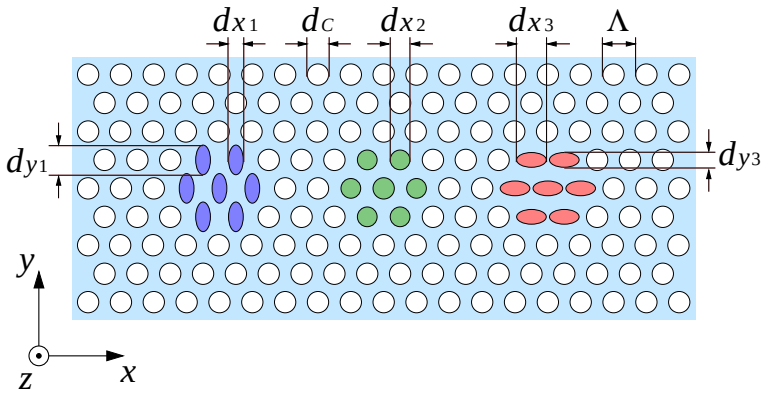

Figure 4.4: Cross sectional view of our proposed PS.

4.1 Design of PS with Large Hole EC-CHFs

EC-CHF with large air holes has a large effective index difference between the core and cladding region, and the waveguide has a strong light confinement. In this section, we design the PS based on large hole EC-CHF (air filling fraction in core is 36.73%). Fig. 4.3 shows the cross sectional view of the triangular lattice yEC-CHF. Here, the parameters of the yEC-CHF refer to Ref. [35], the lattice pitch is $\Lambda = 1.24$ μm, the circular hole diameter in the cladding region is $d_c = 0.65\Lambda$, the major axis of elliptical hole size in the core region is $d_{y1} = 0.9\Lambda$, and the ellipticity is $d_{y1}/d_{x1} = 2$. The refractive index of silica and air are $n_1 = 1.45$ and $n_2 = 1$,

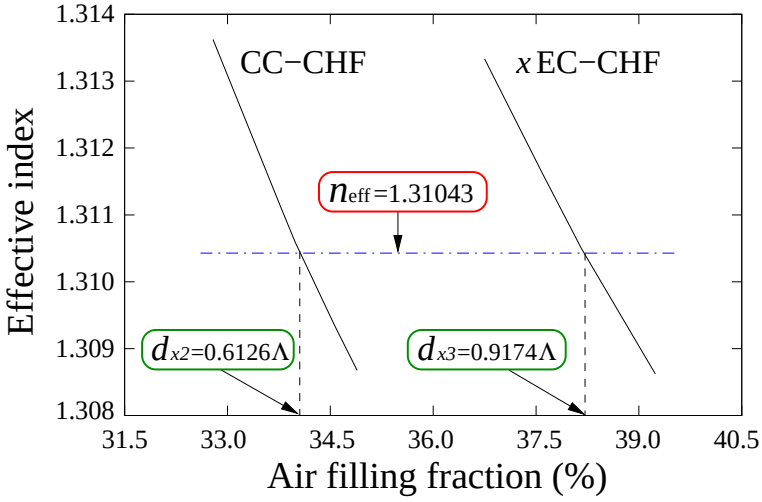

Figure 4.5: Effective refractive indices n_{eff} of the CC-CHF and xEC-CHF as a function of the air filling fraction.

respectively. The operating wavelength is set to $\lambda = 1.55$ μm. The cross sectional view of the proposed PS is shown in Fig. 4.4. In practical design, in order to reduce the insertion loss, it is necessary to satisfy the phase matching condition between the adjacent cores according to the coupled mode theory. In this study, we employ the FV-FEM to estimate the modal effective index. Moreover, we satisfy the phase matching condition by using the effective index of waveguide in isolated system and the FSM of the elliptical air holes in core region for each EC-CHF.

4.1.1 Design of PS using Effective Index of Waveguide

With the determined parameters above, we design the phase matching air holes in the core region of the CC-CHF and xEC-CHF by meeting the same effective index with the reference waveguide yEC-CHF. Figure 4.5 shows the effective refractive indices n_{eff} of the CC-CHF and xEC-CHF as a function of air filling fraction. Here, the ellipticity of the xEC-CHF is considered as $d_{x3}/d_{y3} = 2$. The dashed line represents the effective refractive index of the yEC-CHF. The air hole size that meets the phase matching condition corresponds to $d_{x2} = 0.6125\Lambda$ for the CC-CHF, and corresponds to $d_{x3} = 0.9175\Lambda$ for the xEC-CHF. The magnetic field distributions in each EC-CHF are shown in Fig. 4.6. The mode field diameters in all structures are almost the same.

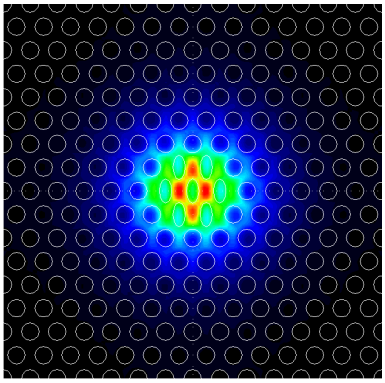

(a) yEC-CHF

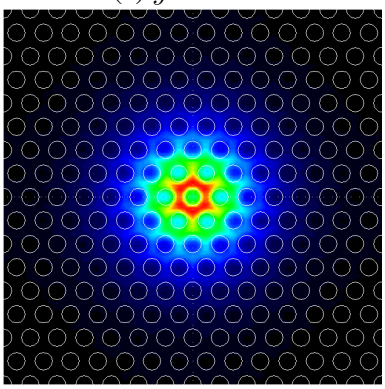

(b) CC-CHF

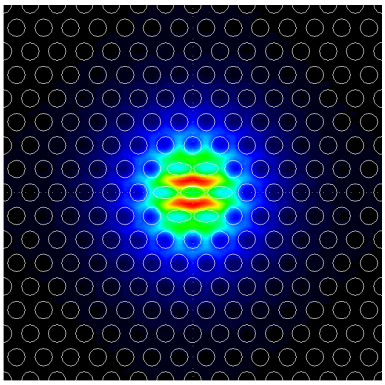

(c) xEC-CHF

Figure 4.6: Magnetic field distribution in each EC-CHF.

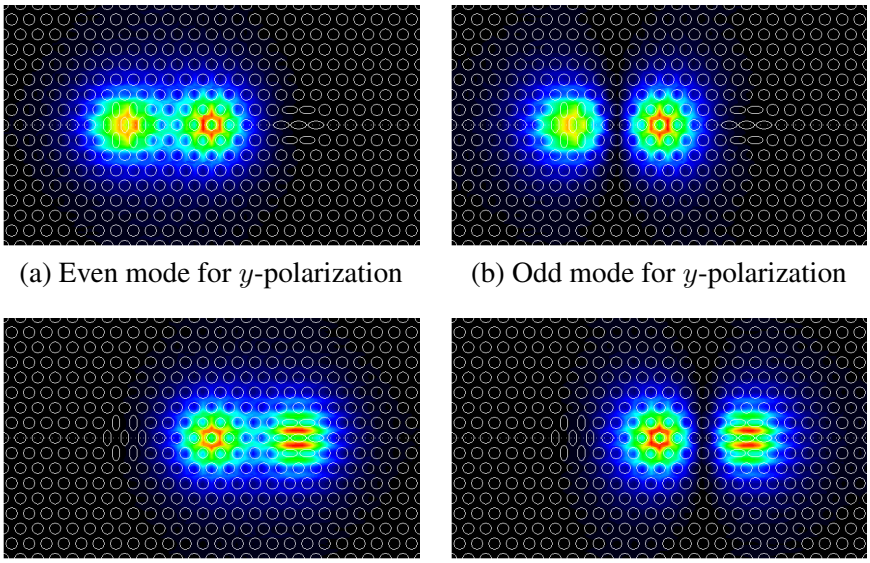

(a) Even mode for y-polarization (b) Odd mode for y-polarization

(c) Even mode for x-polarization (d) Odd mode for x-polarization

Figure 4.7: Even and odd modes field distribution of y- and x-polarization in coupled system, respectively.

So far, three EC-CHFs which satisfy the phase matching condition have been designed, then we will determine the device length of the PS. In this PS, the device length is determined by the coupling lengths of the EC-CHF directional couplers, so we first calculate the coupling length of them. Fig. 4.4 shows the cross-sectional structure of the PS, we note that each core is separated from the adjacent cores by two column of air holes. Fig. 4.7 (a) and (b) show the modal field distributions of the even- and odd-symmetric modes of y-polarization, respectively. We can observe that there is no light coupling to the xEC-CHF. The modal field distributions of the x-polarized modes are shown in Fig. 4.7 (c) and (d), on the contrary, there is no light coupling to the yEC-CHF. The effective refractive indices of the even and odd modes are obtained, then the coupling length L_c can be calculated by

$$L_c = \frac{0.5\lambda}{n_{\text{eff},1} - n_{\text{eff},2}} \tag{4.1}$$

where $n_{\text{eff},1}$ and $n_{\text{eff},2}$ are the effective refractive indices of even- and odd-modes, respectively.

Table 4.1 shows the effective refractive indices of even and odd modes in the coupled system and the estimated coupling lengths for the x- and y-polarization have also be given. The coupling lengths of the x- and y-polarized waves are

Table 4.1: Even and odd mode effective refractive index and the estimated coupling length

	Effective refractive index		
	Even mode	Odd mode	L_c [μm]
x-pol.	1.311040	1.309825	638
y-pol.	1.310982	1.309736	622

slightly different. Consequently, in this thesis the average length has been adopted and the device length is set to $L = 630$ μm. If the coupling length difference between the x- and y-polarized waves is not negligible, the coupling lengths can be independently designed for the x- or y-polarization by adjusting the air hole radius between the cores.

The propagation behavior in the PS is shown in Fig. 4.8. With a beam of 45-degree polarized light is launched into the CC-CHF, we can observe that the light is separated and coupled into left and right side depending on the field components. The y-polarized component (H_x) couples only to the left side yEC-CHF, and the x-polarized component (H_y) couples only to the right side xEC-CHF. The light power of the CC-CHF is almost zero at the device length of 630 μm. The calculated crosstalk is about the same as the computer's round-off error. Actually, there is a difference between the x- and y-polarizations coupling lengths. In order to investigate the extent of the influence, the normalized power along propagation distance has been estimated, as seen in Fig. 4.9. Assuming that a 45-degree polarized light is launched into the CC-CHF, there is a slight deviation in the graph of the xEC-CHF and yEC-CHF according to the difference of the coupling length. However, the normalized power at 630 μm of each waveguide is about 49.98%, the loss due to the difference between two coupling lengths is negligible. In another numerical simulation, if all of the hole sizes deviate 1%, the coupling efficiency degrades around 3%, and if only the hole sizes in a specific core deviate 0.2%, the coupling efficiency degrades around 5%. The structural tolerance will be discussed later in this chapter.

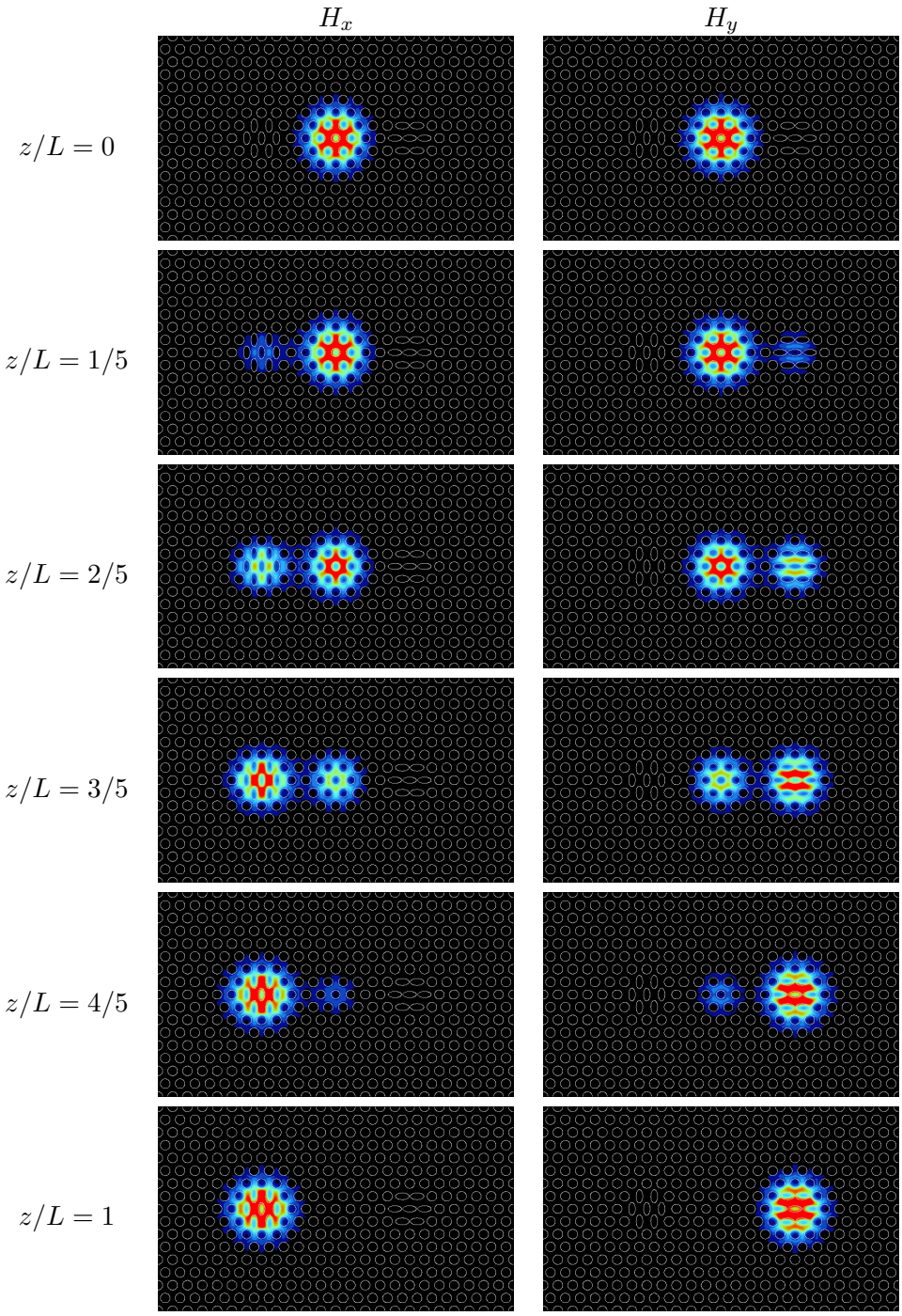

Figure 4.8: Propagation behavior in the PS with large hole EC-CHFs.

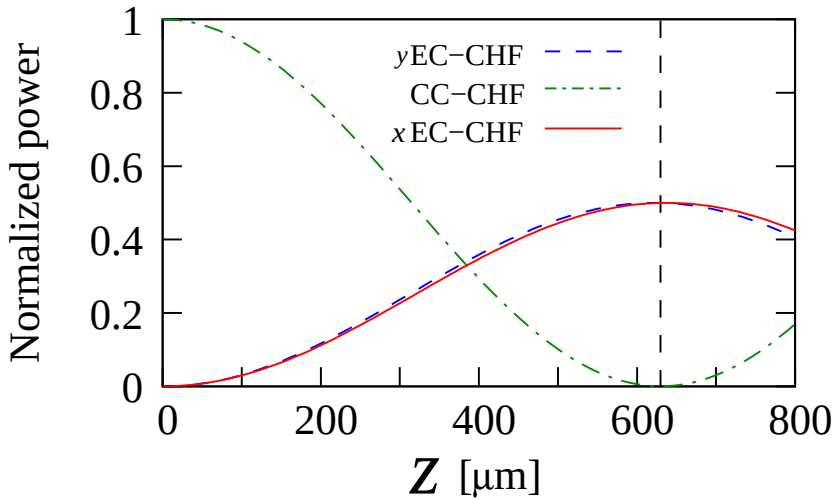

Figure 4.9: Normalized power along the propagation distance.

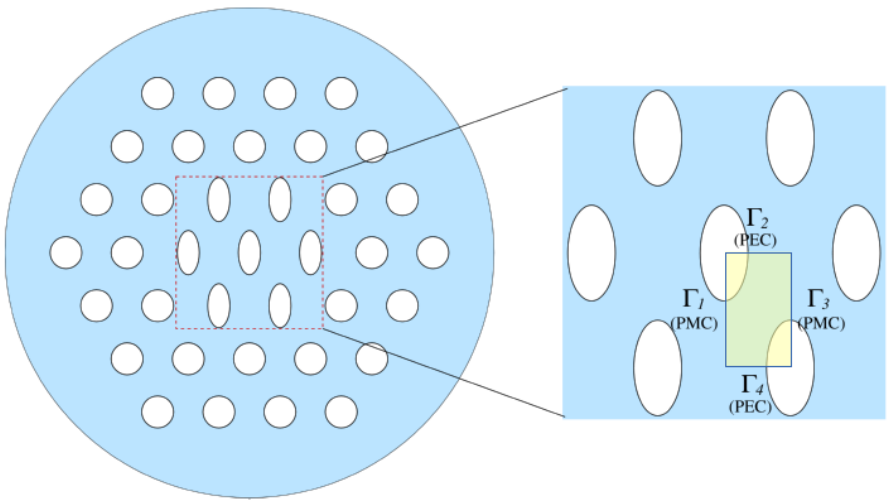

Figure 4.10: FSM of the elliptical air holes in core region for the yEC-CHF.

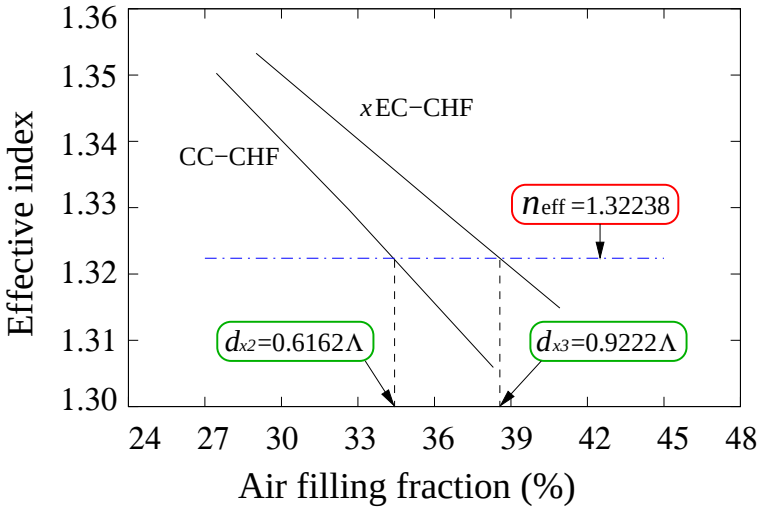

Figure 4.11: Effective indices of the FSM of core region for the large hole CC-CHF and xEC-CHF as a function of the air filling fraction.

4.1.2 Design of PS using FSM of Core

After we determined the air hole sizes of CC-CHF and xEC-CHF which meet the phase matching condition by using the effective index of each waveguide. In this subsection, instead to analyze the complicated whole structure of EC-CHF, we determined the phase matched air holes by using the FSM of the elliptical air holes in core region for each EC-CHF. Schematic of the FSM of a yEC-CHF is illustrated in Fig. 4.10.

The structural parameters of yEC-CHF are set as the same as mentioned above. The centers of all the air holes are arranged in the array of a hexagonal lattice with the hole pitch $\Lambda = 1.24$ μm, the elliptical holes in the core region is $d_{y1} = 0.9\Lambda$, $d_{y1}/d_{x1} = 2$, the diameter of the circular hole in the cladding region is $d_c = 0.65\Lambda$. Fig. 4.11 shows the effective indices of the FSM of core region for the CC-CHF and xEC-CHF as a function of air filling fraction. The effective index of yEC-CHF is illustrated by the dashed line. It can be seen that, the air hole sizes that meet the phase matching condition correspond to $d_{x2} = 0.6162\Lambda$ for the CC-CHF, and $d_{x3} = 0.9222\Lambda$ for the xEC-CHF. However, the numerical simulation demonstrates that in the isolated system, the phase matching condition between the three EC-CHFs can not be perfectly satisfied. In the coupled system, the effective indices of even and odd modes and the estimated coupling lengths for the x- and y-polarizations are

Table 4.2: Effective indices of even and odd modes and the estimated coupling lengths of the PS with the large hole EC-CHFs designed by FSM.

	Effective refractive index		
	Even mode	Odd mode	L_c [μm]
x-pol.	1.310171	1.308866	593
y-pol.	1.310681	1.309073	482

shown in Table 4.2.

There is a remarkable difference between x- and y-polarization coupling lengths. The normalized power along propagation distance of y- and x-polarized waves are illustrated in Fig. 4.12. Consequently, it can be seen that the incident light cannot completely split into two orthogonal polarization states. In particular, the maximum value of the normalized power in yEC-CHF is 0.347 (coupling efficiency is about 69.30%) at propagation distance of 482 μm. The propagation behavior in the PS with a device length of 1000 μm is illustrated in Fig. 4.13. The full-vector FE-BPM is applied to study the propagation along the z-direction. Here, the longitudinal step size is set to 1 μm, the analyzed region of 34.72×24.8 μm, is discretized using curvilinear hybrid edge/nodal elements. Adaptive mesh [87] is used and the total unknowns are 836,538. For the y-polarized component, H_x is the major field, and H_y is the minor field. In the same way, for the x-polarized component, H_y is the major field, and H_x is the minor field. With the propagation of the incident light, we can observe that, the y-polarized component cannot totally couple into the yEC-CHF, and the remain part propagates in the CC-CHF due to the single-polarization property of EC-CHF, and from this point, it also demonstrated that crosstalk- free polarization can be realized through our PS.

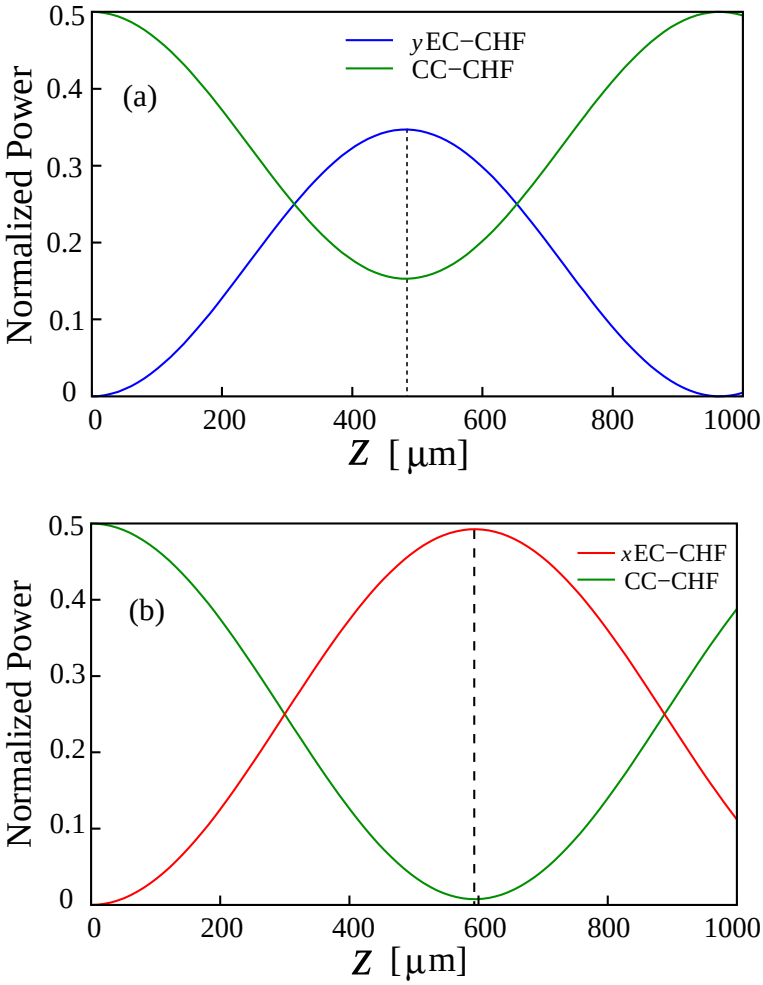

Figure 4.12: Normalized power along propagation of (a) y-polarized wave, (b) x-polarized wave for the PS designed by FSM.

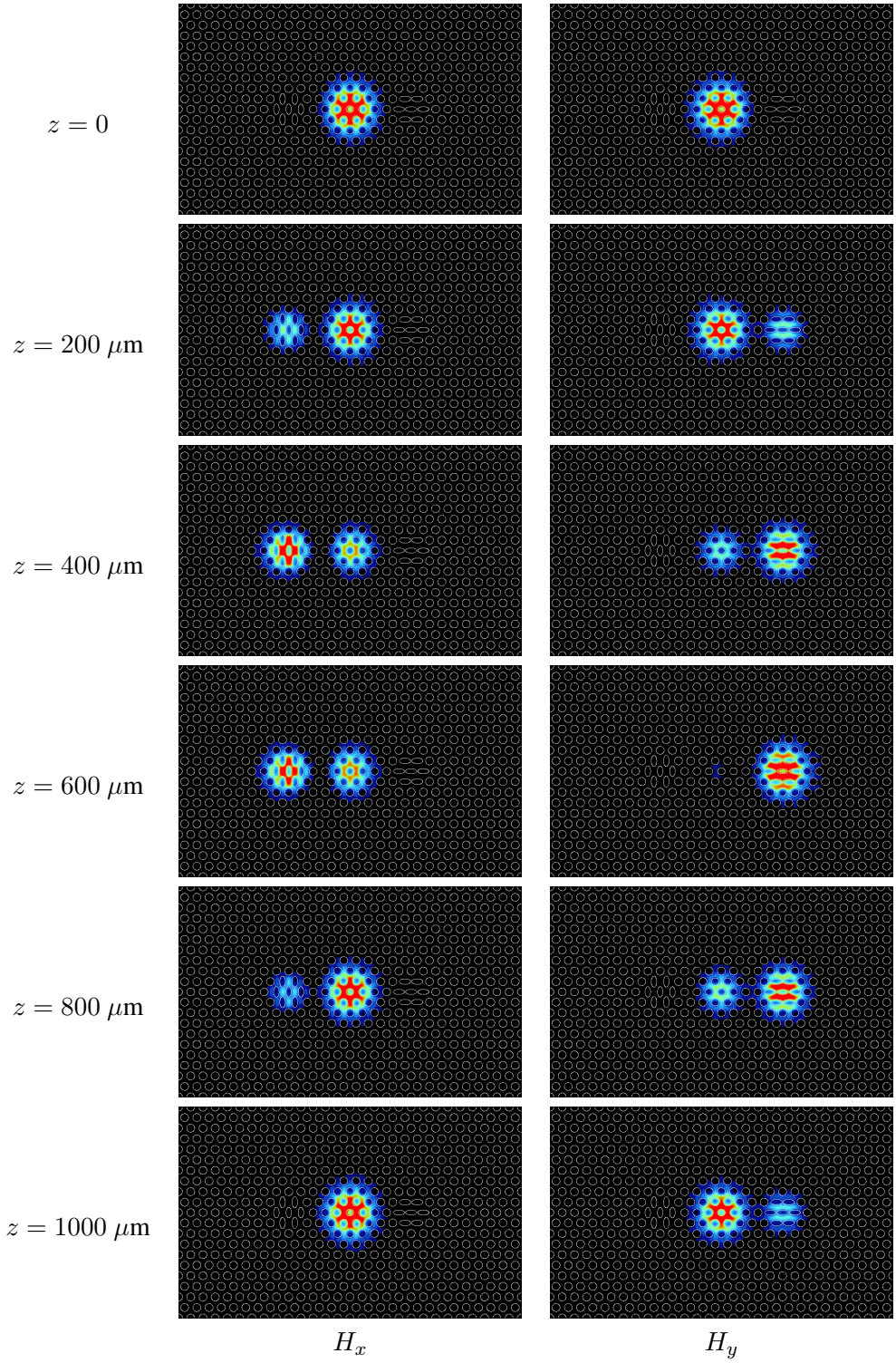

Figure 4.13: Propagation behavior in the PS with the large hole EC-CHF designed by FSM.

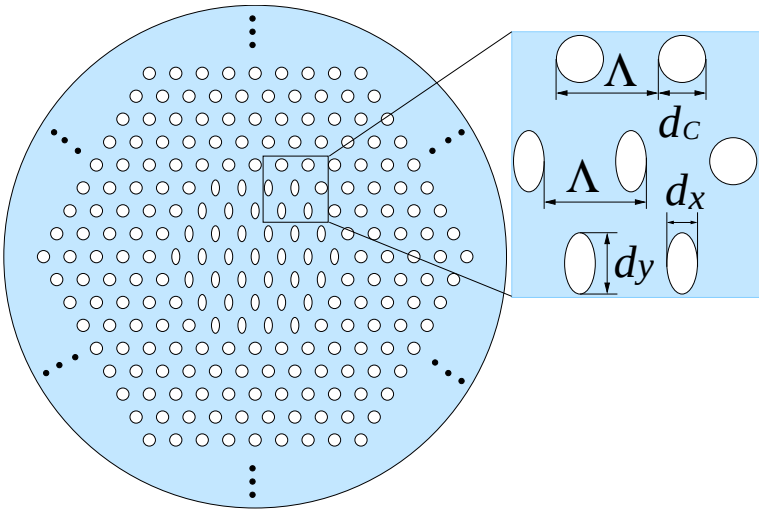

Figure 4.14: Cross sectional view of the small hole 3-ring core yEC-CHF.

4.2 Design of PS with Small Hole EC-CHFs

After we designed the PS with the large hole EC-CHFs which have a strong light confinement of the waveguide, in order to obtain the Gaussian like mode field distribution which can improve the connectivity between the EC-CHF and a standard single-mode fiber (SMF), we designed the PS with the small hole EC-CHFs. The parameters of yEC-CHF are set as follows: $d_{y1} = 0.3\Lambda$ for the major axis of elliptical holes, the ellipticity is set to $d_{\text{major}}/d_{\text{minor}} = 2$, the diameter of circular holes in cladding is $d_c = 0.22\Lambda$, the lattice pitch is $\Lambda = 1.24$ μm, and the operating length is $\lambda = 1.55$ μm. The cross section of the small hole yEC-CHF is shown in Fig. 4.14, it can be seen that the fiber includes three rings of elliptical holes in the core region to increase the optical confinement since the EC-CHF is weakly guiding waveguide with the small holes. Under the determined structural parameters, the effective indices of the FSM for two orthogonal polarization in the core and the cladding region of the yEC-CHF as a function of wavelength is shown in Fig. 4.15. From 800 nm to 2000 nm, we can observed that only y-polarized mode can be guided well in the fiber core because its modal effective index is obviously higher than the cladding effective index, whereas the x-polarized mode is lower than the cladding

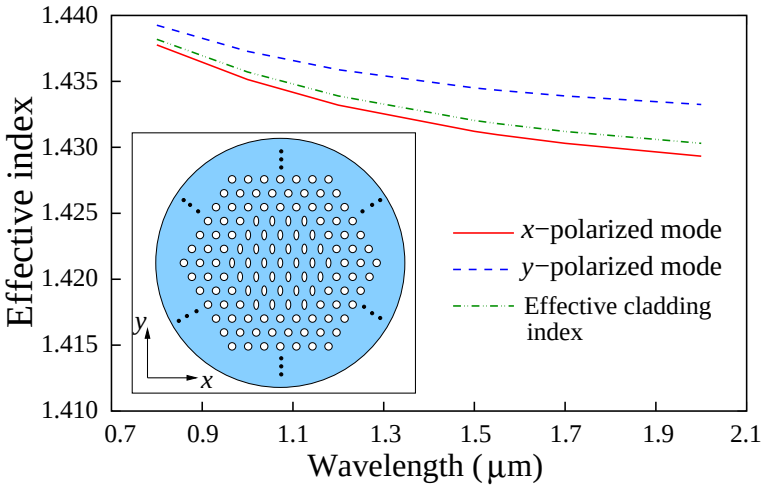

Figure 4.15: Effective indices of FSM for x- and y-polarized modes in the core region and cladding region of the small hole yEC-CHF as a function of wavelength.

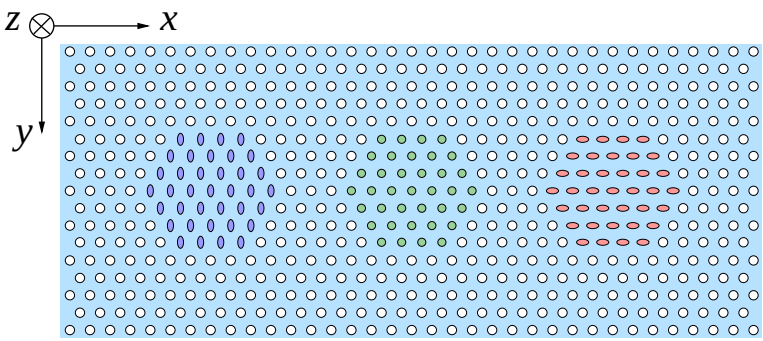

Figure 4.16: Cross sectional view of the PS with small hole EC-CHFs.

effective index. Fig. 4.16 shows the cross sectional structure of the PS, each core is separated from the adjacent cores by three column of air holes.

As we designed the PS based on the large hole EC-CHFs, in order to match the phase condition of each EC-CHF, we use the two design methods to determine the hole size of CC-CHF and xEC-CHF, that is using the effective index of waveguide which has a high accuracy of coupling efficiency and using only the FSM of core region which is easy to design. Fig. 4.17 illustrates the vary of effective indices for the CC-CHF and xEC-CHF as a function of air filling fraction by the two design methods mentioned above. Here we note that the phase matched holes in the core region for the CC-CHF and xEC-CHF have the same sizes based on the two design methods, $i.e.$ $d_{x2} = 0.2022\Lambda$ for the CC-CHF and $d_{x3} = 0.3\Lambda$ for the xEC-CHF. The

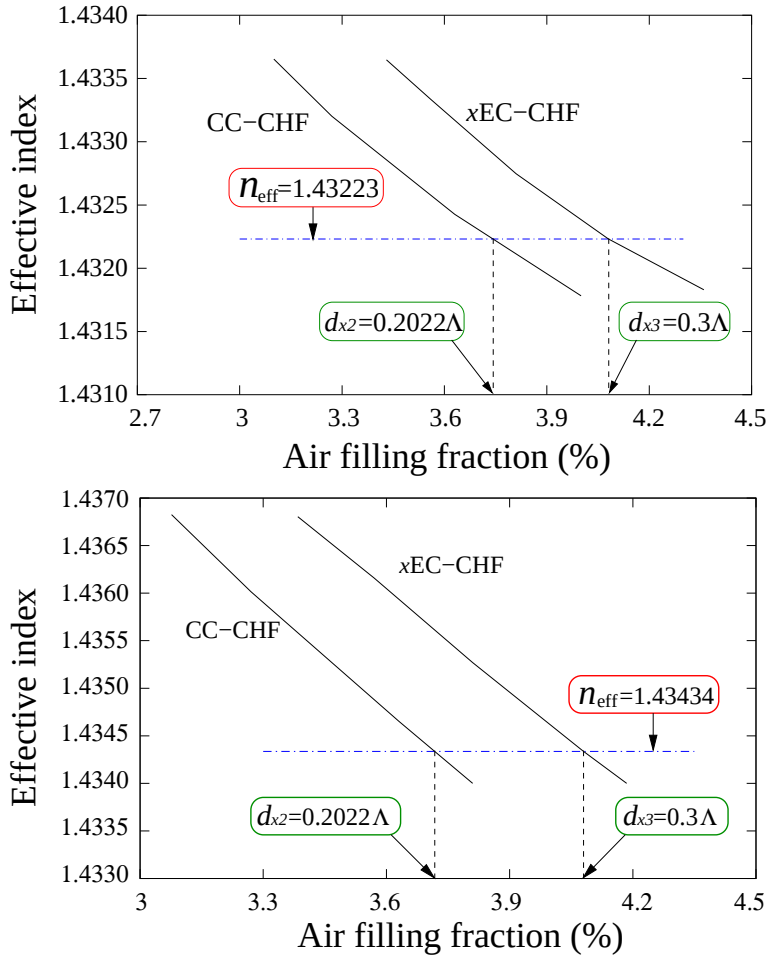

Figure 4.17: Effective indices of (a) the CC-CHF and xEC-CHF, (b) the FSM in core region of the CC-CHF and xEC-CHF, as a function of the air filling fraction.

magnetic field distributions in each EC-CHF are shown in Fig. 4.18. The mode field diameters in all EC-CHFs are almost the same.

With three column of air holes between the adjacent cores, we investigate the effective indices of even and odd modes in coupled system, the magnetic field distributions are shown in Fig. 4.19. And the estimated coupling lengths for x- and y-polarization are also given, as shown in Table 4.3. By adopting the average of the x- and y-polarization coupling lengths, the device length is set to $L = 1940$ μm. The propagation behavior in the PS with device length of 1940 μm is shown in Fig. 4.21. This time, the longitudinal step size is also set to 1 μm, however, the analyzed region is 62×39.68 μm, and the total unknowns are 1,145,650. A 45-degree linearly polarized light is launched into the CC-CHF, with the propagation

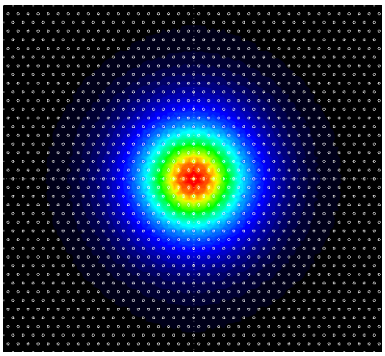

(a) yEC-CHF

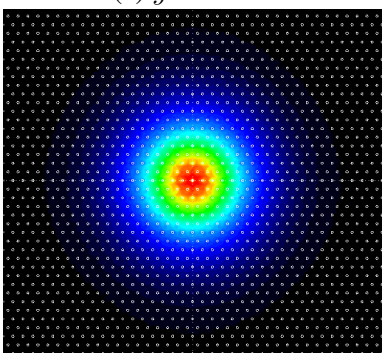

(b) CC-CHF

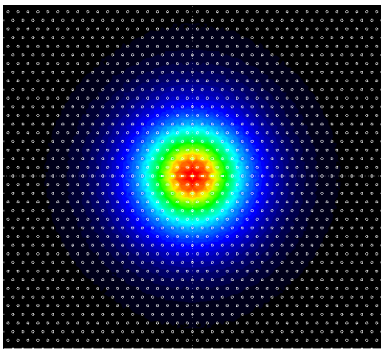

(c) xEC-CHF

Figure 4.18: Magnetic field distribution in each EC-CHF (with small air holes).

of the light, it can be observed that the x-polarized component and y-polarized component couple only to the xEC-CHF and yEC-CHF, respectively. We have also estimated the normalized power against propagation distance as illustrated in Fig. 4.20. The power of incident light in CC-CHF is almost 0 at 1940 μm, and x-polarized wave, y-polarized wave can be completely divided.

Table 4.3: Effective indices of even and odd modes and the estimated coupling lengths of the PS with the small hole EC-CHFs

	Effective refractive index		
	Even mode	Odd mode	L_c [μm]
x-pol.	1.432390	1.431996	1947
y-pol.	1.432395	1.431998	1933

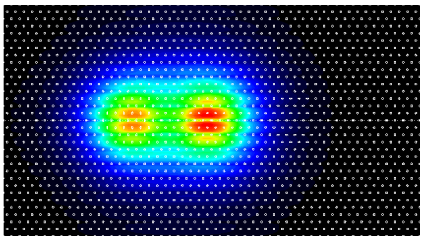

(a) Even mode for y-polarization

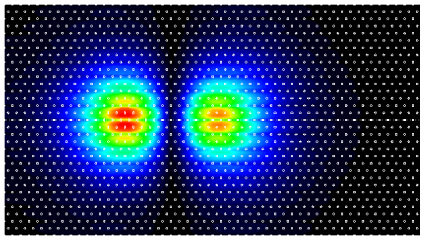

(b) Odd mode for y-polarization

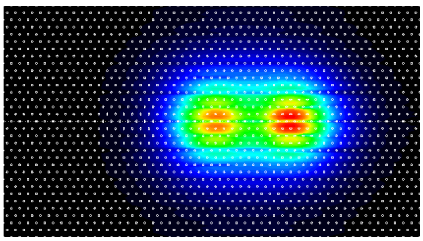

(c) Even mode for x-polarization

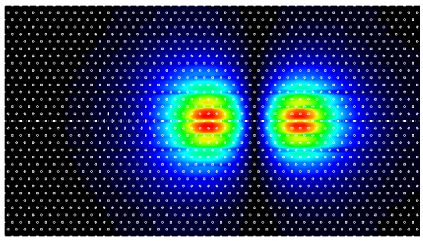

(d) Odd mode for x-polarization

Figure 4.19: Even and odd modes field distribution of PS with small hole EC-CHFs in coupled system.

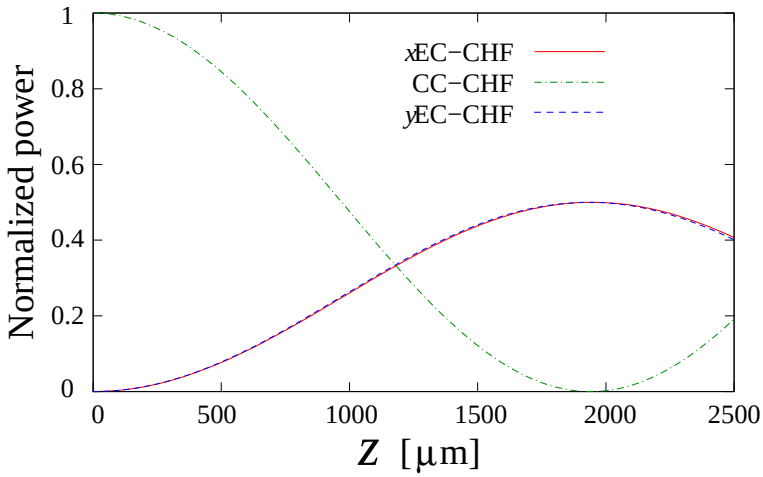

Figure 4.20: Normalized power along the propagation distance.

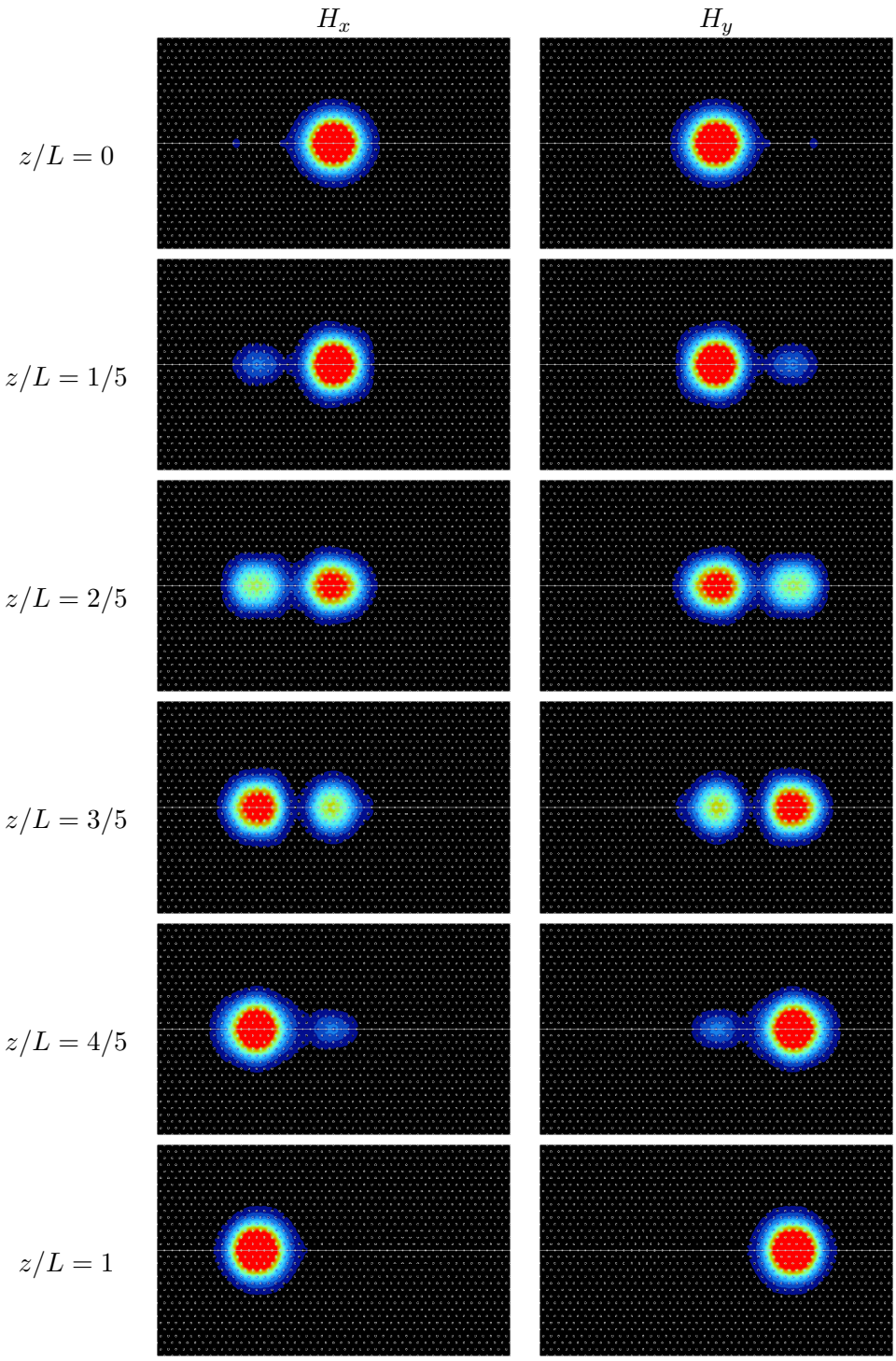

Figure 4.21: Propagation behavior in the PS with small hole EC-CHFs.

4.3 Design Accuracy of FSM Method

Compared with the coupling efficiencies of the PS by using the large hole EC-CHFs and small hole EC-CHFs based on FSM, we can observe that PS with the large hole EC-CHFs cannot obtain a high coupling efficiency. As a consequence, we investigated the vary of coupling efficiency for x- and y-polarization designed by FSM versus air filling fraction of core region, as shown in Fig. 4.22. Here, the ellipticity is considered as $d_{\mathrm{major}}/d_{\mathrm{minor}} = 2$, and the distance between the two adjacent cores is fixed to two air holes. Reference to the original parameters of yEC-CHF (the major axis of elliptical hole in core region is 0.9Λ, the diameter of circular hole in cladding is 0.65Λ), the circular hole size in cladding region varies as same ratio as the elliptical hole in core region to ensure the realization of single-polarization propagation of EC-CHF. In addition, as we know the EC-CHF with smaller holes leads to a weaker light confinement, so we introduce a multi-ring structure in core region to enhance the light confinement of the waveguide when the hole sizes decrease. Fig. 4.22 shows that the coupling efficiencies of x- and y-polarized waves decrease with the air filling fraction for each PS with different kinds of EC-CHFs. The normalized propagation constant b of a waveguide is defined as follows:

$$b = \frac{n_{\mathrm{eff}}^2 - n_2^2}{n_1^2 - n_2^2} \tag{4.2}$$

where n_{eff} is the effective index of the waveguide in isolated system, n_1 and n_2 represent the FSMs of core and cladding regions, respectively, and b is a quantity between 0 and 1. Small b means the waveguide has a weak light confinement that can realize light coupling easily. On the other hand, a waveguide with a large b has a strong light confinement and it is not easy to be coupled. b of a waveguide increases with air filling fraction for each region of the EC-CHFs. For example, the PS with 1-ring core EC-CHFs (the range of the air filling fraction is from 25.51% to 36.73%), it can be calculated that b is 0.2725 and the coupling efficiency of y-polarization is 68.8% at the air filling fraction of 36.73%. On the other hand, when the air filling fraction is 25.51%, b is 0.1185 and the coupling efficiency of y-polarization is 98.5%. Weakly light confinement fibers have a large insertion loss of input and output fiber even though it can realize the light coupling easily.

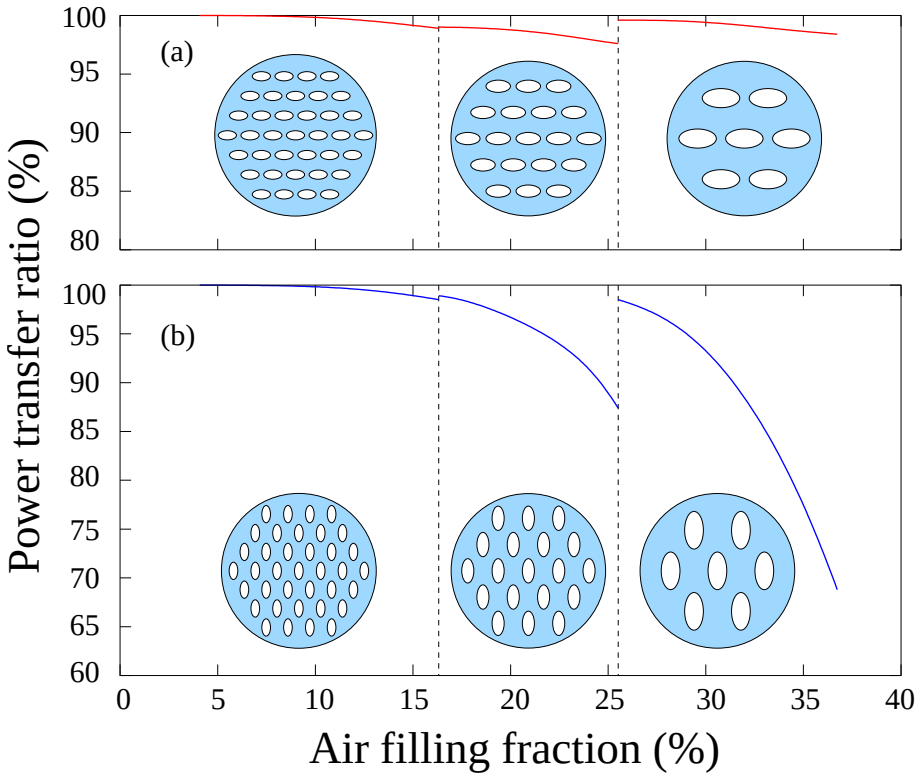

Figure 4.22: Coupling efficiency of (a) x-polarized wave, (b) y-polarized wave for the PS designed by FSM as a function of air filling fraction.

Therefore, the 2-ring core structure is generally used at the air filling fraction of 25.51%, although the coupling efficiency of y-polarization decreases to 87.4%. In the actual fabrication, according to the normalized propagation constant of needs, we determine the rings in the core region of the reference waveguide (such as the yEC-CHF in this paper) and the distance between the two adjacent cores, then we can choose the high design accuracy of FSM method to design the PS effectively.

4.4 Structural Tolerance and Wavelength Dependence of PS

In this section, we will focus on the structural tolerance and wavelength dependence of our designed PS. First of all, we will give the coupling efficiency formula of a coupled system. In a coupled system, the coupling efficiency F between the two adjacent waveguides is defined as

$$F = \frac{\kappa^2}{\kappa^2 + \psi^2} = \frac{1}{1 + \left(\frac{\psi}{\kappa}\right)^2} \tag{4.3}$$

with

$$\psi = \frac{1}{2}(\beta_2 - \beta_1) = \frac{\pi}{\lambda}(n_{\text{eff},1} - n_{\text{eff},2}) \tag{4.4}$$

where κ is the coupling coefficient between the two adjacent waveguides. ψ is the difference of propagation constants between the two adjacent waveguides in isolated system, and $n_{\text{eff},1}$ and $n_{\text{eff},2}$ are the respective effective indices of the two waveguides. Using the guide mode in isolated system, coupling length L_c can also be defined as follows:

$$L_c = \frac{\pi}{2\gamma}\,, \qquad \gamma = \sqrt{\kappa^2 + \psi^2} \tag{4.5}$$

where γ is a quantity which is related to the periodical power transfer between the two adjacent waveguides. When $L_c = \pi/(2\gamma)$, the power of incident light transmits from one waveguide to another completely. From the above, the coupling efficiency F between the two waveguides can be calculated by using the effective indices of the two waveguides in isolated system and the effective indices of the even and odd modes in coupled system, as shown as the following equation.

$$F = 1 - \left(\frac{n_{\text{eff},1} - n_{\text{eff},2}}{n_{\text{eff,e}} - n_{\text{eff,o}}}\right)^2 \tag{4.6}$$

Considering the current fabrication technology of PCF, the biggest problem in the fabrication process of an EC-CHF is the deviation of the circular or elliptical air holes away from the initial parameter values. So we discussed the effect of the deviation of the geometric parameters designed with the large and small hole EC-CHFs. Since the air holes deviate irregularly in fabrication, we investigated the coupling efficiency of the PS against all air holes varies randomly from the initial

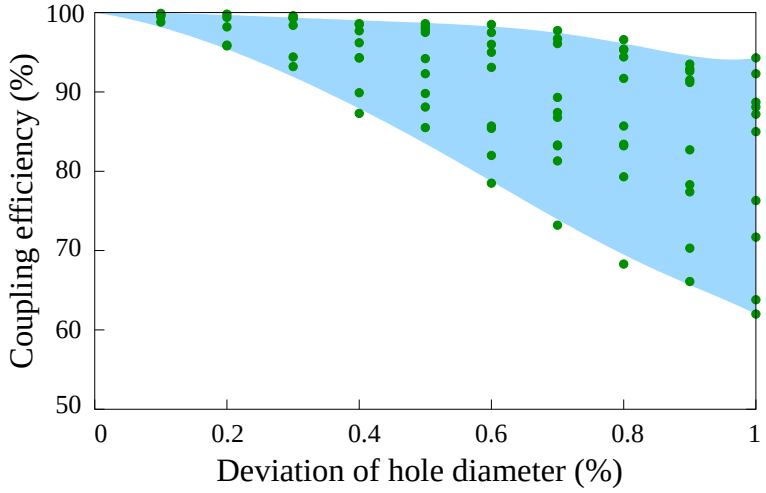

Figure 4.23: Coupling efficiencies of the PS with the large hole EC-CHFs against the random deviation of all the air holes.

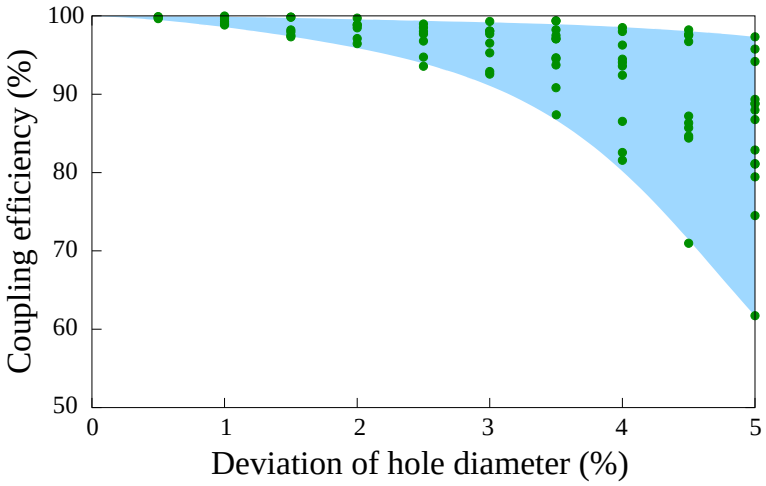

Figure 4.24: Coupling efficiencies of the PS with the small hole EC-CHFs against the random deviation of all the air holes.

parameters. Reference to the previous section, the parameters of each large hole EC-CHF are determined as follows: $d_{y1} = 0.9\Lambda$ for the major axis of elliptical holes in the yEC-CHF, $d_{x2} = 0.6126\Lambda$ for the core size of the CC-CHF, $d_{x3} = 0.9174\Lambda$ for the xEC-CHF, the ellipticity is $d_{\mathrm{major}}/d_{\mathrm{minor}} = 2$, $d_c = 0.65\Lambda$ for the holes in the cladding, each core is separated from the adjacent cores by two column of air holes, and the device length is fixed to 630 μm. Fig. 4.23 shows the coupling efficiency

Table 4.4: PS with large EC-CHF: Coupling efficiency versus the deviation for different parts of the device parameters at each deviation level.

Deviation level	Core region			Cladding region
	xEC-CHF	CC-CHF	yEC-CHF	
-0.3%	88.9%	85.4%	87.6%	99.8%
-0.2%	94.5%	92.6%	94.3%	99.7%
-0.1%	97.9%	97.2%	98.4%	99.3%
0	99.9%	99.9%	99.9%	99.9%
0.1%	97.8%	98.0%	98.2%	98.6%
0.2%	94.3%	94.2%	94.0%	98.0%
0.3%	88.9%	88.0%	87.6%	97.3%

of the PS with the large hole EC-CHFs against the random deviation of all the air holes. It can be observed that the coupling efficiency is almost 90% when the deviation is smaller than 0.4% of their initial parameters, and the coupling efficiency is better than 60% when the deviation is smaller than 1% of the initial parameters. On the other hand, Fig. 4.24 shows the coupling efficiency of the PS with the small hole EC-CHFs designed in section 4.2 against the random deviation of all the air holes. Compared with the condition in Fig. 4.23, the coupling efficiency is better than 90% when the deviation is smaller than 3% of their initial parameters, and the coupling efficiency is better than 60% when the deviation is smaller than 5% of the initial parameters. The PS with the small hole EC-CHFs has a higher tolerance than the splitter with the large hole EC-CHFs because it has more elliptical air holes in core region which lead to reducing the average of deviation and decrease the impact to effective index of the waveguide.

Moreover, we have also examined the coupling efficiency versus the deviation for the respective hole sizes of each region, as shown in Table 4.4 and Table 4.5. Here, all the hole sizes of the deviation part are varied with the same extent, such as if only the holes in xEC-CHF core region are expanded 1%, the coupling efficiency of the PS with small hole EC-CHFs will decrease to 87.7%. Compared with the random deviation of all the holes mentioned above, the deviation for one part of the device with same extent leads to a worse coupling efficiency. Especially for the coupling efficiency with deviation in the core regions which is much worse than the varies in the cladding, that is because in an EC-CHF, the effective index is

Table 4.5: PS with small EC-CHF: Coupling efficiency versus the deviation for different parts of the device parameters at each deviation level.

Deviation level	Core region			Cladding region
	xEC-CHF	CC-CHF	yEC-CHF	
-1%	86.1%	86.0%	86.3%	99.8%
-0.66%	94.0%	93.6%	94.1%	99.9%
-0.33%	98.6%	98.3%	98.6%	99.9%
0	100%	100%	100 %	100%
0.33%	98.3%	98.7%	98.4%	99.9%
0.66%	94.0%	94.9%	94.2%	99.9%
1%	87.7%	88.9%	87.8%	99.8%

sensitive to the hole sizes in the core region. So if we design this type of PS using other kinds of single-polarized PCFs [25]-[41] which have only circular air holes or no holes in the core region, it may be possible to obtain a device with larger tolerance. In addition, the splice loss between an EC-CHF and a SMF should also been considered, according to [93], the splice loss is not so large by adjusting the parameters of EC-CHF and SMF.

In order to achieve the wide-band transmission, we have also investigated the wavelength dependence of the PS with the large and small hole EC-CHFs, respectively, as shown in Fig. 4.25. The proposed PS with the large hole EC-CHFs has a coupling efficiency better than 20 dB at 1.55μm and a bandwidth of 50 nm from 1.52 to 1.57 μm, the PS with the small hole EC-CHFs exhibits a wider bandwidth of 160 nm from 1.47 to 1.63 μm. That is because the EC-CHF with small holes is a weakly guiding, and the effective index of the waveguide varies slightly versus wavelength, as shown in Fig. 4.26. Therefore, the PS based on small hole EC-CHF has a wider bandwidth.

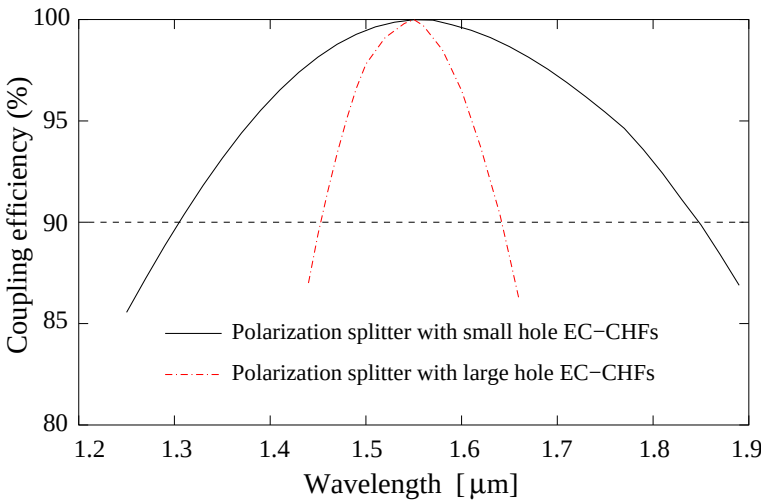

Figure 4.25: Coupling efficiency of the PS versus the light wavelength.

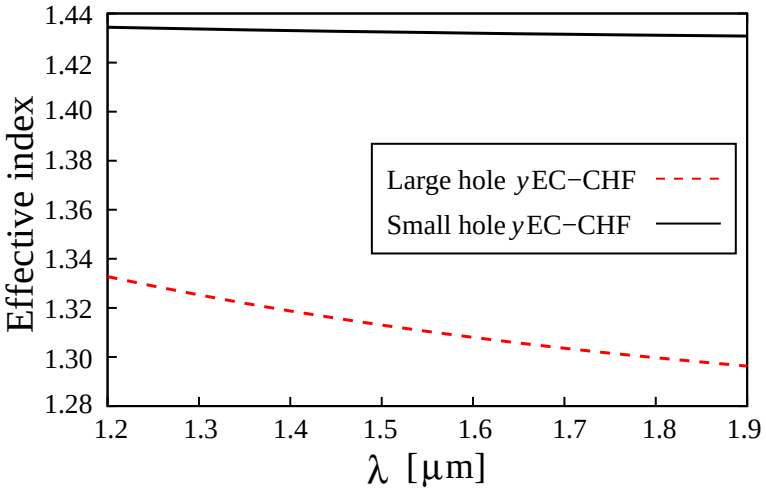

Figure 4.26: Effective index of the yEC-CHF versus wavelength.

In our research, the main object is to achieve a cross-talk free optical device. So far, we have designed the cross-talk free PS based on large and small hole EC-CHFs, and the corresponding structural tolerance and wavelength dependence have also been discussed in detail. As we know, the two EC-CHF output waveguides are the key components of the PS. Due to the single-polarization transmission of the EC-CHF, even the phase matching condition between the CC-CHF and yEC-CHF (or xEC-CHF) can not be perfectly satisfied, the uncoupled y-polarized component (or x-polarized component) would remain in the CC-CHF, and the output wave is still single polarized. Therefore, keeping single-polarization property of the EC-CHF is the basic condition of this design. Here, we investigate the absolutely single-polarization of the yEC-CHF with a various geometric elliptical holes. In our designing process, the major axis of the large hole yEC-CHF is $d_y = 0.9\Lambda$, the ellipticity is $d_{\text{major}}/d_{\text{minor}} = 2$, and the diameter of the circular holes in the cladding is $d_c = 0.65\Lambda$. During the fabrication process, since the ellipticity of the elliptical air holes is difficult to maintain in 2, thus we investigate the large hole yEC-CHF dispersion curves against a variation d_y while the elliptical hole area is unchanged, as shown in Fig. 4.27. The green dashed line represents the constant FSM in the cladding. We note that the elliptical holes in the core with a large major axis lead to a large birefringence, and the single polarization transmission can be easily achieved. Since the major axis d_y should smaller than the lattice pitch Λ, we only discussed until the d_y increased by 10% ($d_y/\Lambda = 0.99$). Moreover, if the d_y reduces by more than 18% ($d_y/\Lambda < 0.738$), the FSM of x-polarization is higher than the FSM of cladding, the single polarization can not be realized. Consequently, the single polarization property of the large hole yEC-CHF can be achieved with $d_y/\Lambda > 0.738$ by keeping the hole area.

In the same way, the dispersion curves of small hole yEC-CHF have also been investigated, as shown in Fig. 4.28. The initial parameters of the small hole yEC-CHF are given as: the major axis of the elliptical holes is $d_y = 0.3\Lambda$, the ellipticity is $d_{\text{major}}/d_{\text{minor}} = 2$, the diameter of circular holes in the cladding is $d_c = 0.22\Lambda$. The single polarization property of the small hole yEC-CHF can be achieved with $dy/\Lambda > 0.264$ by keeping the hole area.

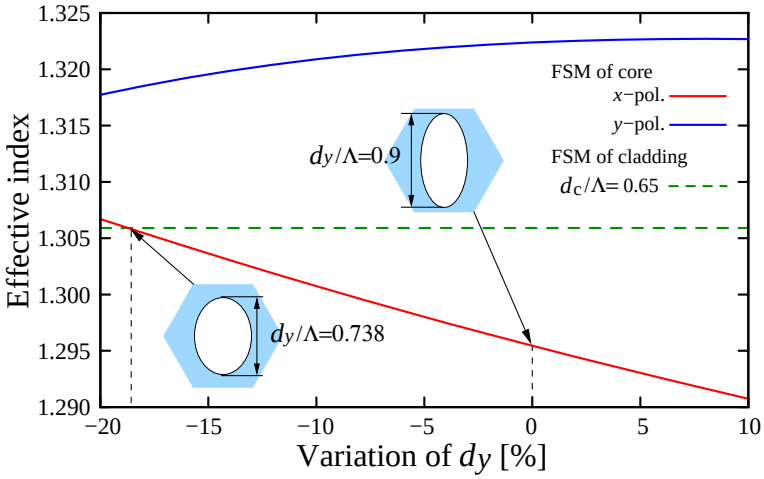

Figure 4.27: Effective index variation of the large hole yEC-CHF against the major axis d_y by keeping the elliptical hole area ($\lambda = 1.55\mu$m).

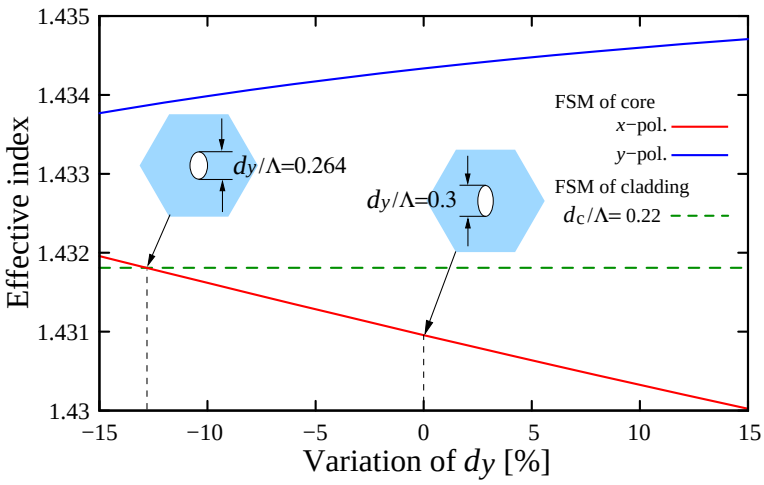

Figure 4.28: Effective index variation of the small hole yEC-CHF against the major axis d_y by keeping the elliptical hole area ($\lambda = 1.55\mu$m).

Chapter 5

Cross-Talk Free Polarization Converter

After we design the PS based on triangular lattice EC-CHFs, we will focus on another important component in the optical communication system, the PC, which can convert a liner polarization by 90 degrees. In our research, firstly, we proposed a novel single PC element based on the square lattice EC-CHF, as shown in Fig. 5.1. After that, in order to obtain a cross-talk free PC element, we adopt two EC-CHFs on both sides of the PC waveguide as the input and output waveguides, respectively. Moreover, considering the fabrication technology in recent years, the structural tolerance of the cross-talk free PC has been investigated detailedly.

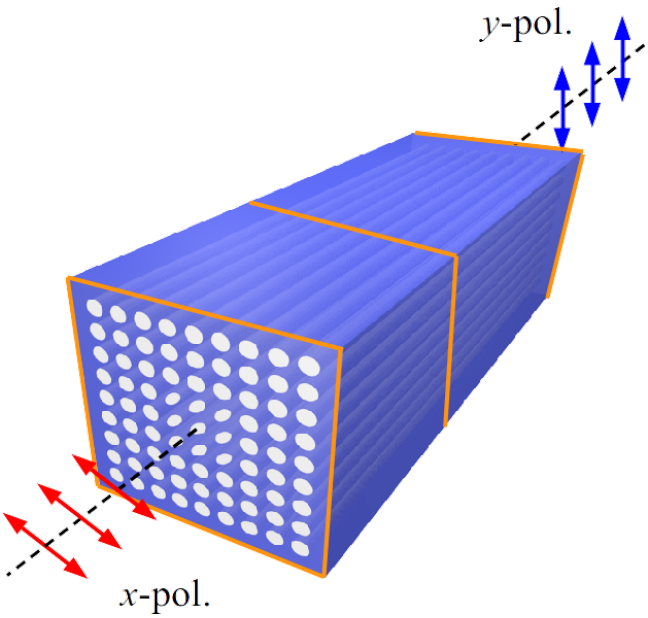

Figure 5.1: 3 dimensional structure of our proposed single PC element.

Additionally, we consist the cross-talk free PC with a PS to form a PSC based

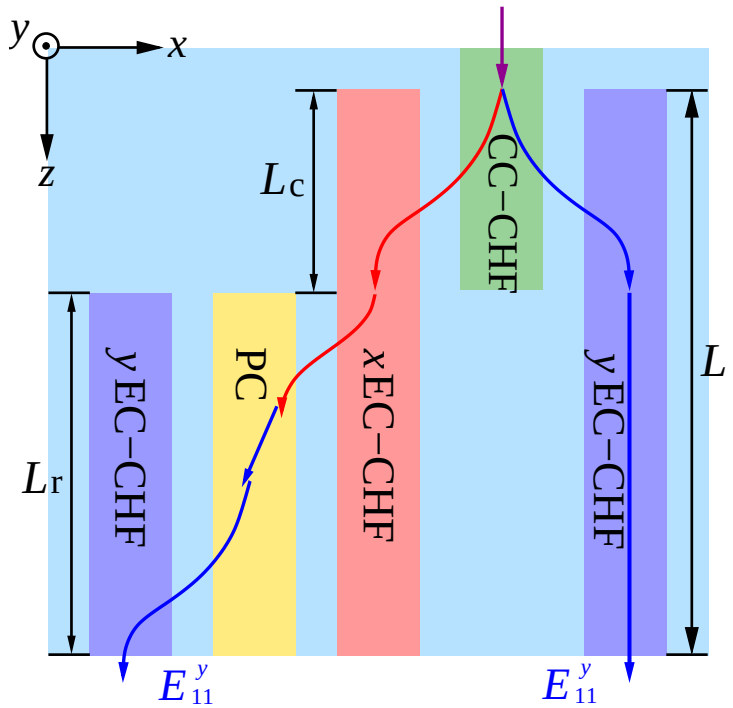

Figure 5.2: Structure and cross-sectional distribution of our proposed PSC.

on square lattice EC-CHFs. The incident light beam can be split and converted simultaneously without any cross-talk. The structure of our proposed PSC is illustrated in Fig. 5.2. It consists of five EC-CHFs in parallel, from left to right in order, a yEC-CHF, a PC with oblique elliptical holes in the core region, an xEC-CHF, a CC-CHF and a yEC-CHF. When an arbitrarily polarized light beam is launched into the input waveguide CC-CHF, firstly, it splits into the x- and y-polarized components which couple to the xEC-CHF and yEC-CHF, respectively. Then, the x-polarized component in the xEC-CHF couples to the PC waveguide and converts to the y-polarized component. Finally, with the light propagation, the converted y-polarized component couples to the yEC-CHF at the left side. Consequently, utilizing the absolutely single-polarization transmission property of an EC-CHF, when an arbitrarily polarized light wave is launched into the PSC, only y-polarized wave can be output. Moreover, only x-polarized wave can also be obtained by exchanging the yEC-CHF and xEC-CHF easily.

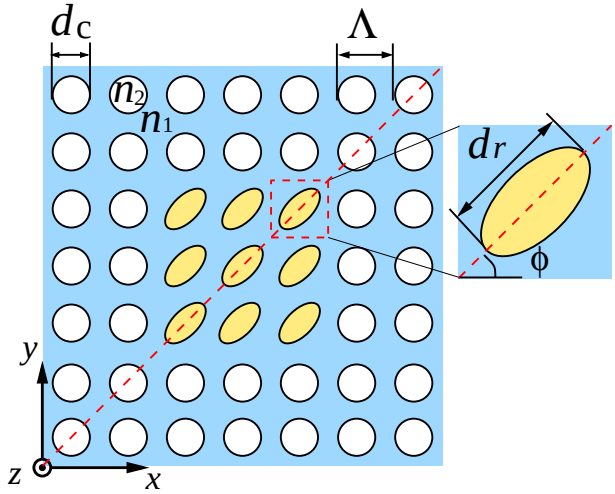

Figure 5.3: Cross-section view of the single PC element.

5.1 Design of Single PC Element with Square Lattice EC-CHF

In this subsection, we propose a novel PC based on a square lattice EC-CHF with a short conversion length. The cross-sectional structure of our proposed PC is illustrated in Fig. 5.3. The PC waveguide has nine oblique elliptical-holes in the core region whose major axis is rotated counter clockwise by $\phi = 45°$ with respect to the x-axis. Due to the symmetrical structure with respect to $y = x$, incident x- or y-polarized wave can be completely rotated $90°$. Refer to [74], the hybridness is defined as

$$\text{Hybridness} = \max|H_\mu| / \max|H_\nu| \tag{5.1}$$

where μ and ν are x and y for x-polarized mode while y and x for y-polarized mode, respectively. The conversion length L_r is defined as $L_r = 0.5\lambda/(n_{\text{eff},1} - n_{\text{eff},2})$, where λ is the operating wavelength, $n_{\text{eff},1}$ and $n_{\text{eff},2}$ represent the effective indices of two eigenmodes of the single PC. With the elliptical holes in the core, the PC element has a large birefringence which leads to a short conversion length. The basic structural parameters are set as follows: the lattice pitch Λ is 1 μm, all the elliptical-holes have the same ellipticity of $d_{\text{major}}/d_{\text{minor}} = 2$, the refractive indices of silica and air are $n_1 = 1.45$ and $n_2 = 1$, respectively, the operation wavelength is set to $\lambda = 1.55$ μm. In order to design the PC element, the guided modes in coupled and isolated systems are analyzed by using the FV-FEM, and the light propagation

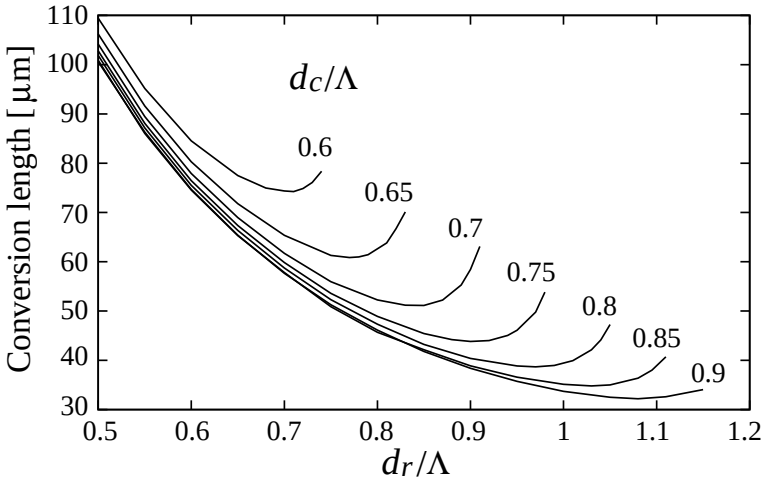

Figure 5.4: Hole sizes dependence of the conversion length.

Table 5.1: Minimum conversion length and corresponding elliptical-hole size for different hole sizes in the cladding.

d_c/Λ	d_r/Λ	Min. of L_{r1} [μm]
0.60	0.71	74.25
0.65	0.77	60.85
0.70	0.85	51.13
0.75	0.90	43.84
0.80	0.97	38.69
0.85	1.03	34.80
0.90	1.08	32.20
0.91	1.09	31.70

in the PC is simulated by using the FE-BPM.

Here, we investigate the hole size dependence of conversion length L_{r1}, as shown in Fig. 5.4. We note that with a constant hole size in the cladding, the conversion length decreases when d_r increases at first, and then it has a slight increase after reaching the minimum value. This is because the larger elliptical holes make the birefringence larger. However, with the elliptical holes getting larger, most of the light spreads into the birefringence-free cladding region, and this leads to a longer conversion length. Moreover, it also can be observed that the minimum value of conversion length decreases with larger circular-holes in the cladding. Table 5.1 shows the minimum conversion length and the corresponding major axis length of ellipse for different hole sizes in the cladding. The table also illustrates

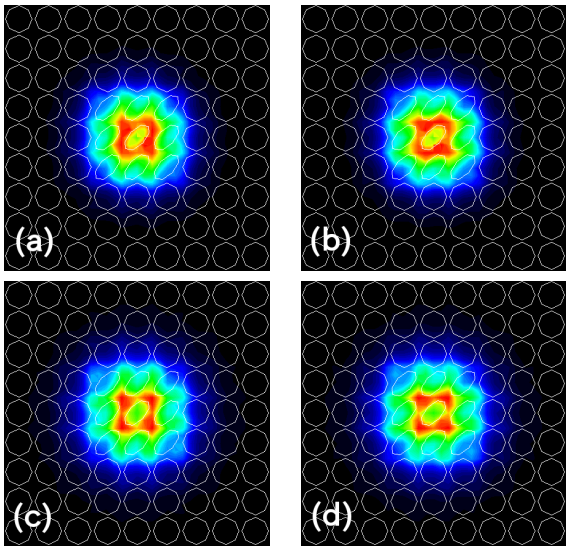

Figure 5.5: Magnetic field distributions of the (a) H_x and (b) H_y components for the fundamental mode (effective index is $n_{\text{eff},1} = 1.23914$), and the (c) H_x and (d) H_y components for the 1st-higher-order mode (effective index is $n_{\text{eff},2} = 1.21469$).

the shortest conversion length we have obtained, $i.e.$, $L_{r1} = 31.7$ μm with the hole sizes of $d_c = 0.91\Lambda$ and $d_r = 1.09\Lambda$. Figure 5.5 shows the magnetic field distributions of H_x and H_y components for the fundamental and 1st-higher-order modes, respectively. It can be observed that the two field profiles are very similar, and the hybridness is 0.99994 for the fundamental mode and 0.99921 for the 1st-higher-order mode. The propagation behaviors obtained by the full-vector FE-BPM in the PC with the shortest conversion length are shown in Fig. 5.6. It can be observed that an x-polarized incident light can be completely converted into a y-polarized light through our proposed PC. However, since both of the x- and y-polarized components exist in the same waveguide, the ER in the single PC element should be considered. Here, the ER in PC is defined as

$$\text{ER} = 10\log_{10}\frac{\text{Output power of } x\text{-polarization}}{\text{Output power of } y\text{-polarization}}. \tag{5.2}$$

A BPM simulation shows that the ER is -23dB at $\lambda = 1.55\mu$m. Here, the longitudinal step size is set to 1 μm, the analyzed region of 13×13 μm, is discretized using curvilinear hybrid edge/nodal elements [85]. An adaptive mesh [87] is used and the total unknowns are 191,559.

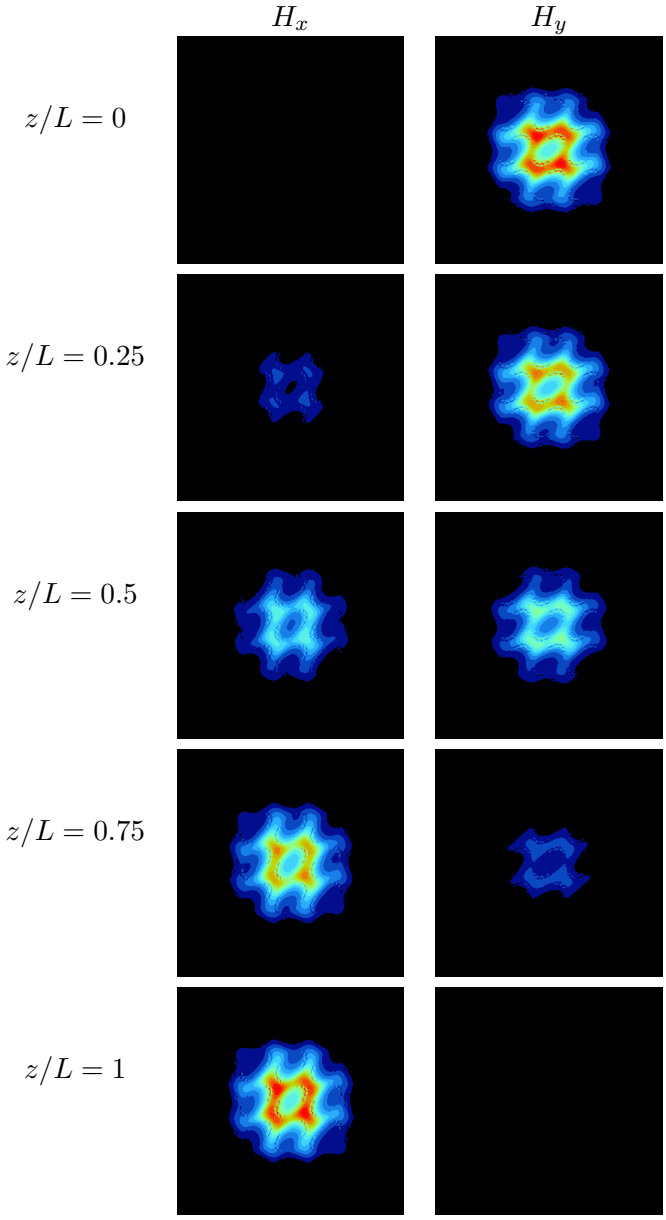

Figure 5.6: Propagation behavior in the single PC ($L_r = 31.7$ μm).

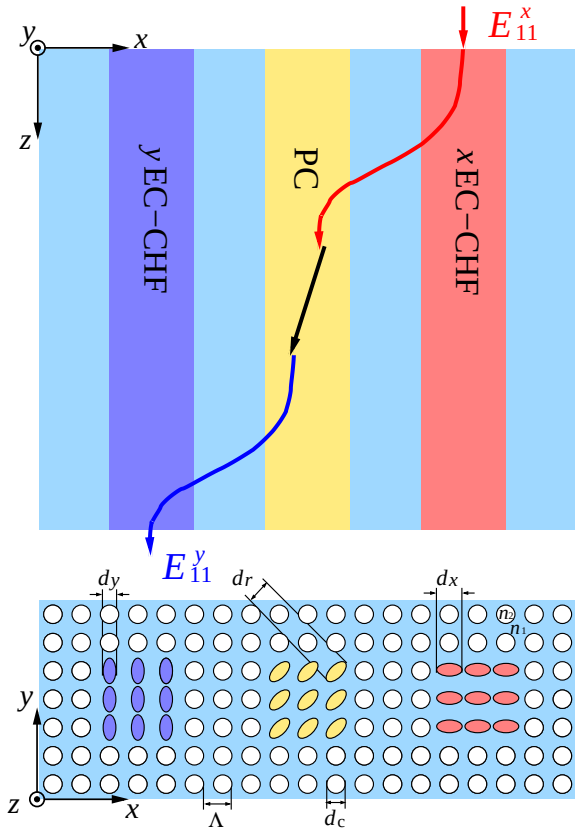

Figure 5.7: Cross-section view of a cross-talk free polarization converting part.

5.2 Design of Cross-Talk Free PC Element with Three EC-CHFs

In the previous subsection, we designed a single PC element based on a square lattice EC-CHF. In general, considering the deviation of hole sizes in the fabrication process, 100% conversion is difficult to achieve and a considerable ER may exist in this PC. However, in our study, in order to realize the cross-talk free device, a yEC-CHF and an xEC-CHF are added at both sides of the PC waveguide to ensure that the input and output waves are absolutely single-polarized. Fig. 5.7 shows the cross-sectional structure of our proposed cross-talk free three-core PC element. Here we set the PC waveguide in the middle, and design the hole size in the core by satisfying the phase matching condition with two EC-CHFs. According to the coupled mode theory, if an x-polarized light beam is launched into the xEC-CHF, it would be coupled into the PC and converted into a y-polarized light; then the converted y-polarized component would be coupled into the yEC-CHF at the left

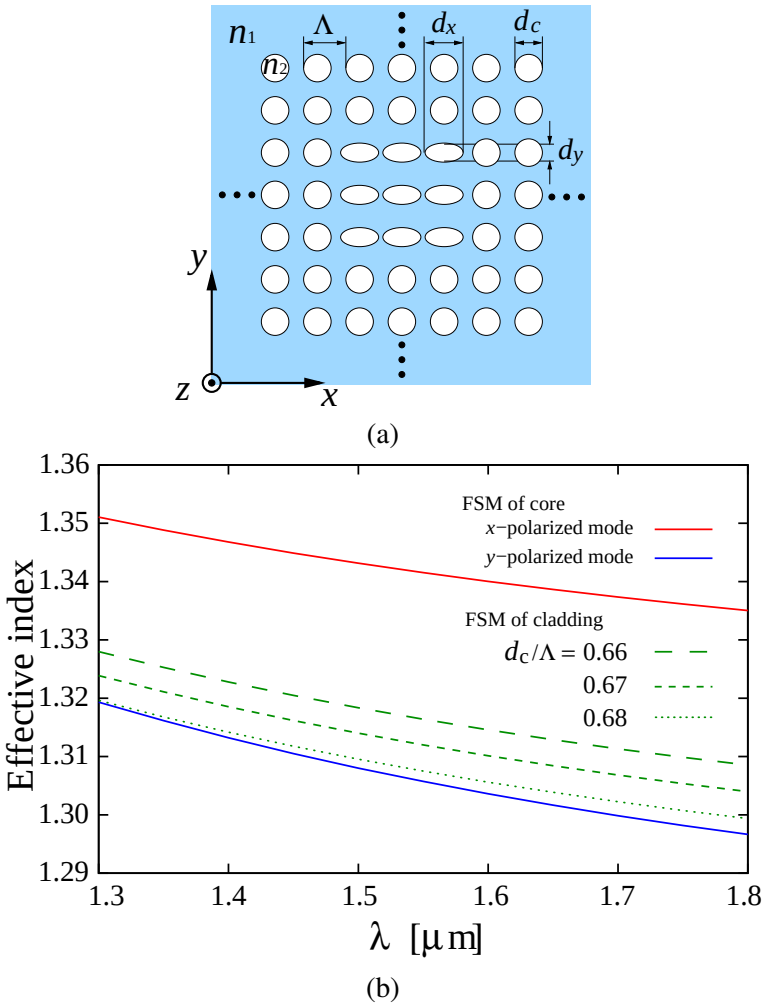

Figure 5.8: Cross-sectional view of the (a) square lattice xEC-CHF and (b) the dispersion curves of this xEC-CHF with different cladding holes.

side. Owing to the square lattice arrangement, the yEC-CHF and xEC-CHF have the same hole sizes for satisfying the phase matching condition. Therefore, we set the xEC-CHF at right side as the reference waveguide, the major axis length of elliptical-holes is set to $d_x = 0.9\Lambda$. The dispersion curves of the xEC-CHF are illustrated in Fig. 5.8, we note that the EC-CHF has a large birefringence by introducing elliptical holes in the core, the effective index of FSM for the x-polarization is much higher than the y-polarization. Three dashed curves between the FSMs of x- and y-polarizations represent the FSM of cladding with different circular hole sizes, $i.e.$ $d_c/\Lambda = 0.66,\ 0.67$ and 0.68, respectively. In order to achieve the single-polarization with a wide bandwidth for the EC-CHF, the hole size in the cladding

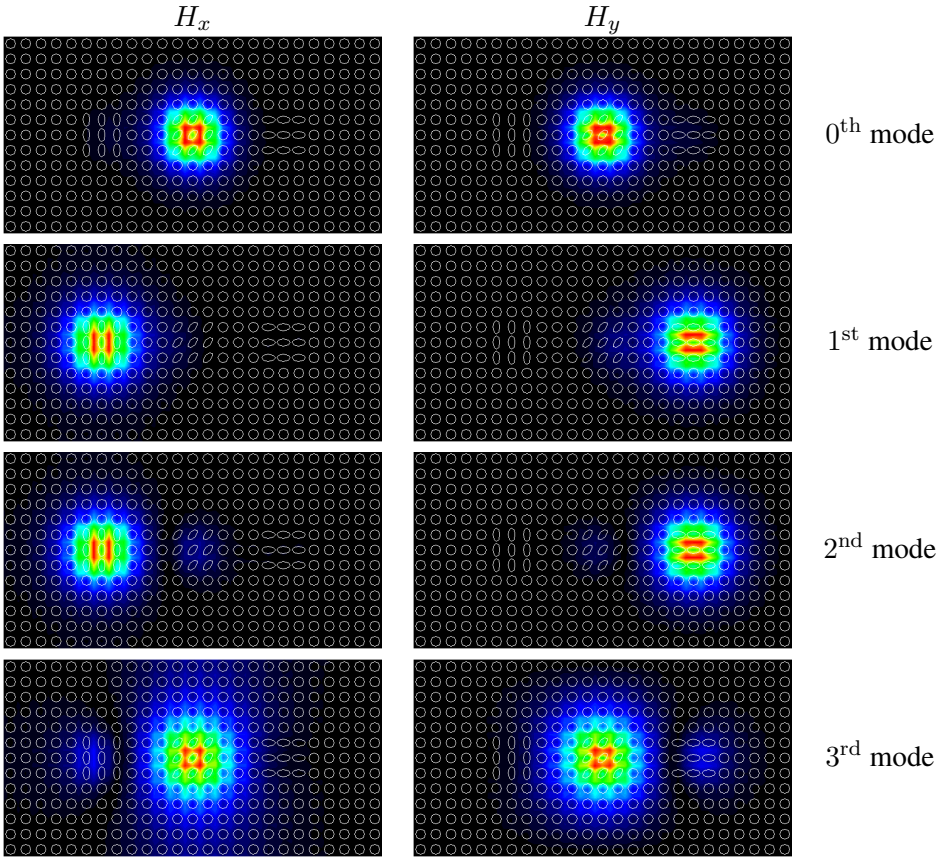

Figure 5.9: Modal field distribution of each coupled mode with $d_r = 0.835\Lambda$.

is set to $d_c/\Lambda = 0.66$. The effective index of the xEC-CHF in isolated system is $n_{\text{eff},x} = 1.32531$.

Then, we design the phase matching hole size in the core of PC waveguide. Since the PC waveguide has two eigenmodes, here we determine d_r by meeting $n_{\text{eff,pc}} = n_{\text{eff},x}$, where $n_{\text{eff,pc}}$ is the average value of effective indices of the two eigenmodes, and the corresponding d_r is $d_r/\Lambda = 0.835$.

In the coupled system, under the determined parameters for the three-core PC, there are four kinds of coupled modes exist ($i.e.$, both x- and y-polarized modes in the PC waveguide, the single x- and y-polarized modes in the xEC-CHF and yEC-CHF, respectively, are coupled to each other.) and the polarization conversion is achieved by utilizing these mode couplings. The modal field distribution of each coupled mode with $d_r/\Lambda = 0.835$ is illustrated in Fig. 5.9. It can be observed that the four coupled modes are almost isolated. In this case, the polarization conversion is achieved through the coupling between the 1st- and 2nd-modes. The polar-

ization conversion with these modes requires a relatively long conversion length since the coupling length depends on the minimum index difference between these coupled modes. In order to obtain a short conversion length, we investigate the effective index variation of four coupled modes against d_r, as shown in Fig. 5.10. Based on the coupled mode theory for three coupled modes, the same effective index difference between the coupled modes is required to obtain a short conversion length. Therefore, we investigate the variation of four coupled modes near $d_r/\Lambda = 0.795$ and 0.865 in detail, as shown in Figs. 5.11 (a) and (b), respectively. The figures show that the effective indices of three coupled modes in the bottom have the same index difference $\Delta = 5 \times 10^{-4}$ at $d_r/\Lambda = 0.798$. In addition, the same index difference $\Delta = 5 \times 10^{-4}$ can also be obtained at $d_r/\Lambda = 0.867$. Here, we use $d_r/\Lambda = 0.798$ to design the PC. The modal field distribution of each coupled mode is illustrated in Fig. 5.12. The first coupled modes of H_x and H_y are almost isolated and do not contribute to the polarization conversion, while the other three coupled modes contribute to the polarization conversion.

The calculated conversion length is $L_r = 0.5\lambda/\Delta = 1550$ μm, and the propagation behaviors are shown in Fig. 5.13. Here, the longitudinal step size is set to 1 μm, the analyzed region is 25×13 μm, and the total unknowns are 429,251. We can observe that after an x-polarized light is launched into the xEC-CHF, it is completely converted into a y-polarized light through our proposed PC. The ER of three-core PC element can be illustrated as follows,

$$\text{ER} = 10\log_{10}\frac{P_{1y\to 3x} + P_{1y\to 3y} + P_{1x\to 3x}}{P_{1x\to 3y}}. \tag{5.3}$$

where P_{1x} and P_{1y} respect to the power of x- and y-polarizations in the input waveguide xEC-CHF, P_{3x} and P_{3y} are the power of x- and y-polarizations in the output waveguide yEC-CHF, $P_{1y\to 3x}$ and $P_{1x\to 3x}$ represent the x-polarization in output waveguide which is converted by the P_{1y} and P_{1x}, respectively. In the same way, $P_{1y\to 3y}$ and $P_{1x\to 3y}$ represent the y-polarization in output waveguide which is converted by the P_{1y} and P_{1x}, respectively. Owning to the absolutely single-polarization property of an EC-CHF, P_{1y} for the xEC-CHF is 0, and P_{3x} for the yEC-CHF is 0. Therefore, the numerator of the ER fraction is 0, and the ER is infinitely high, the cross-talk free property is achieved.

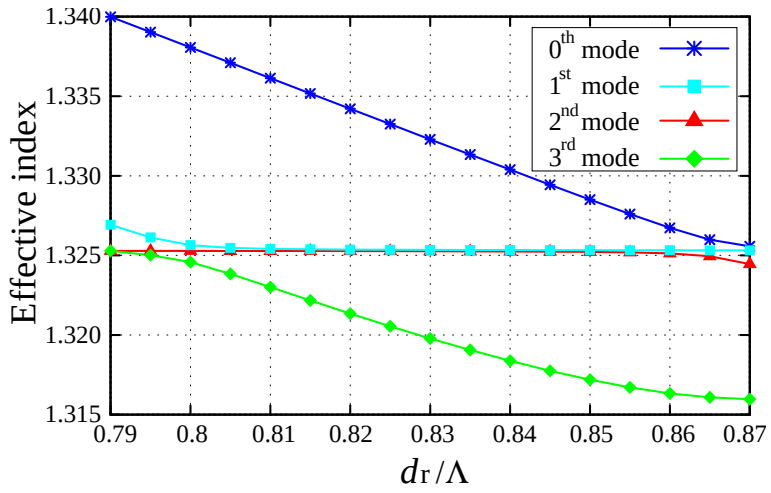

Figure 5.10: Effective indices of four coupled modes against d_r.

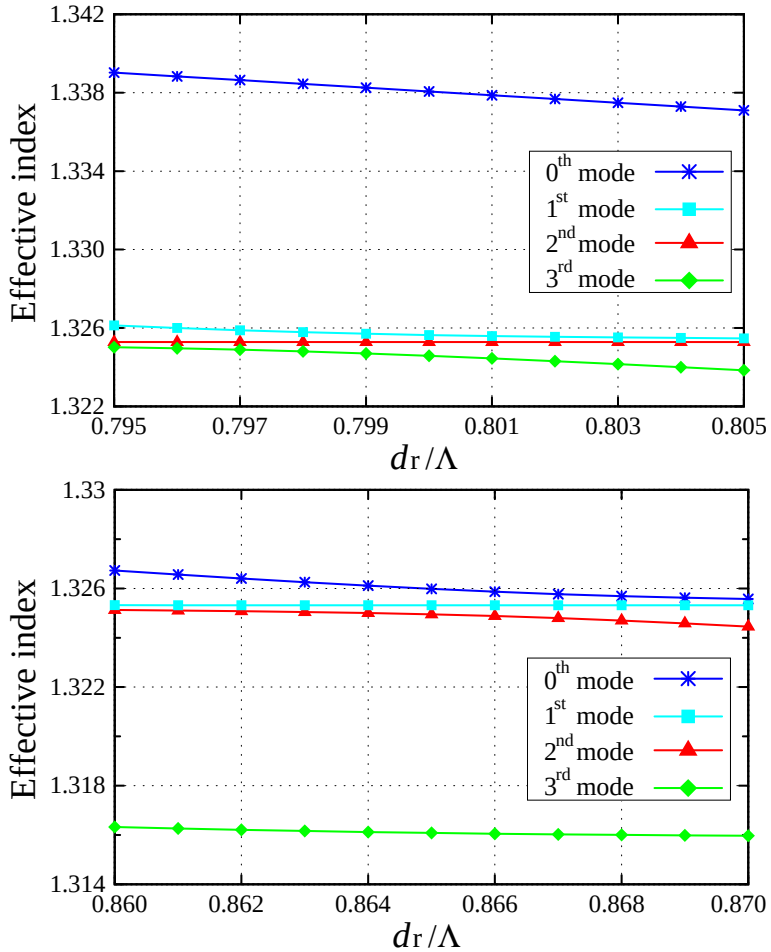

Figure 5.11: Effective indices of four coupled modes against d_r (a) near $d_r = 0.795\Lambda$, (b) near $d_r = 0.865\Lambda$.

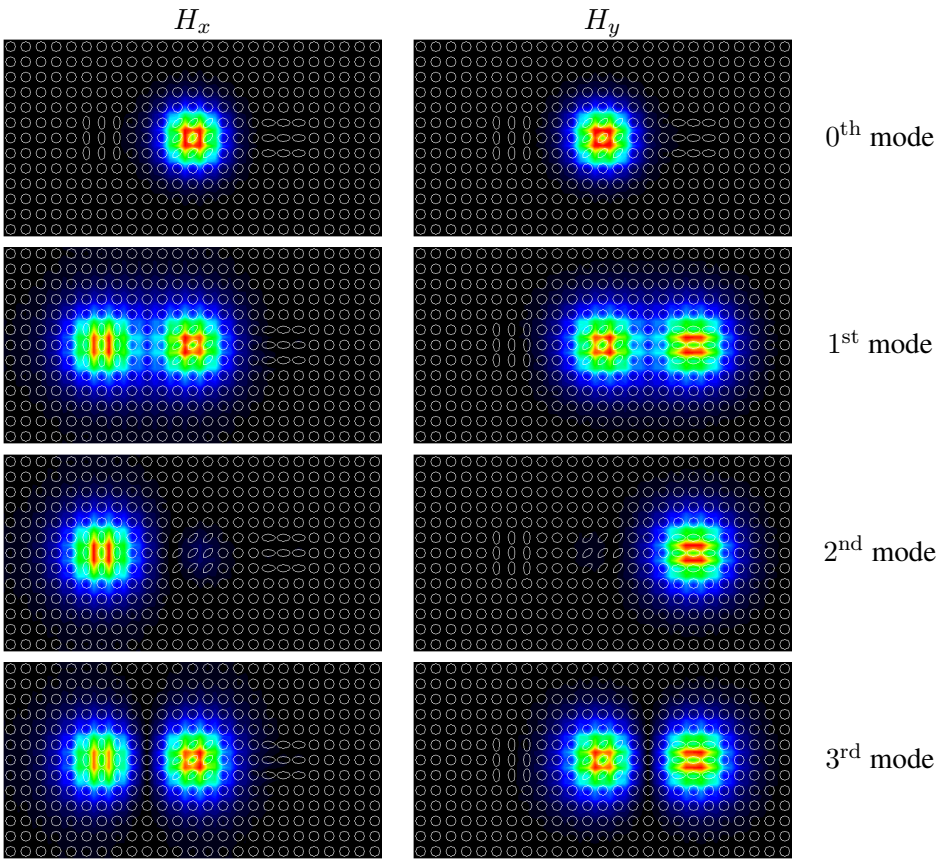

Figure 5.12: Modal field distribution of each coupled mode with $d_r = 0.798\Lambda$.

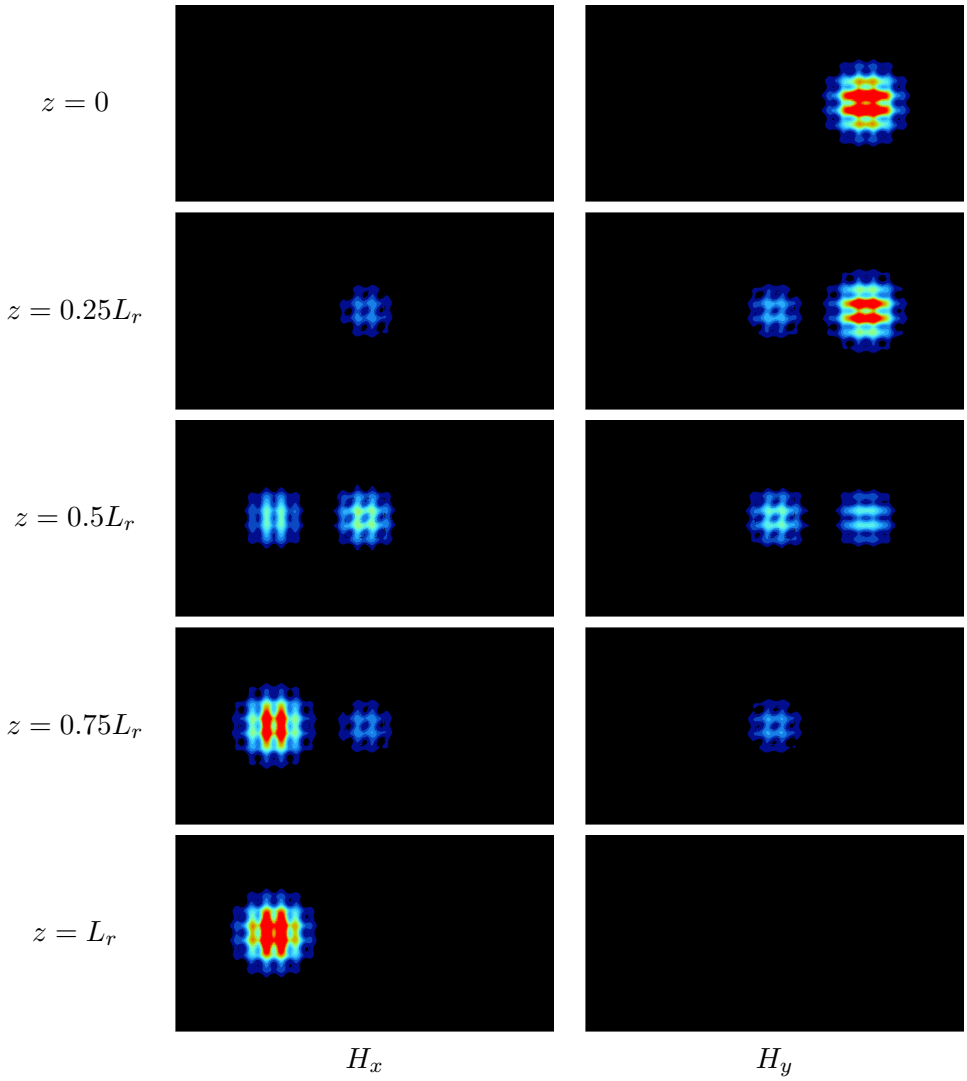

Figure 5.13: Propagation behavior in the polarization converting part ($L_r = 1550$ μm).

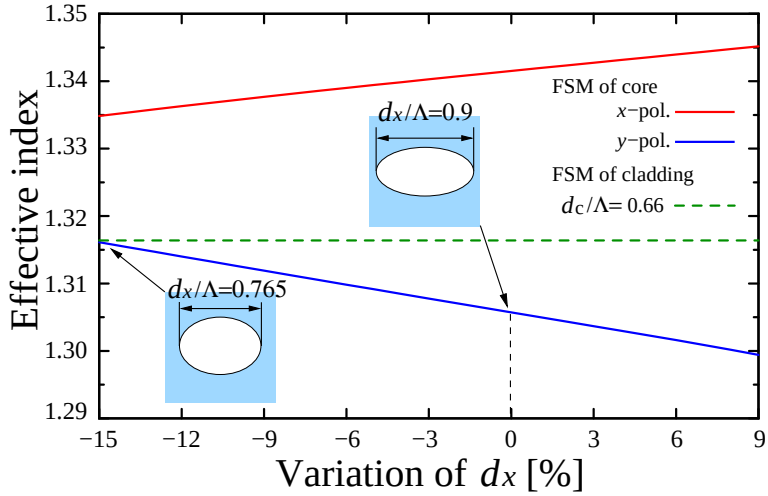

Figure 5.14: Effective index variation of the xEC-CHF against the major axis d_x by keeping the elliptical hole area ($\lambda = 1.55$ μm).

5.3 Structural Tolerance of Cross-Talk Free PC Element

So far, we have proposed and designed a novel PC element based on three-core EC-CHFs. Considering the current fabrication technology of PCF, one of the difficulties in our proposed PC element is the deviation of the air holes away from the designed values. Here, we wish to further discuss the structural tolerance of the cross-talk free three-core PC element. Since two EC-CHFs on both sides are the key components to obtain the cross-talk free property, firstly, we investigate the absolutely single-polarization of the xEC-CHF with a various geometric elliptical holes. In our designing process, the major axis of elliptical hole is $d_x/\Lambda = 0.9$, and the ellipticity is $d_{\text{major}}/d_{\text{minor}} = 2$. However, in practical manufacturing process, the ellipticity is difficult to maintain in 2, thus we investigate the xEC-CHF dispersion curves against a variation d_x while the elliptical hole area is unchanged, as shown in Fig. 5.14. The green dashed line represents the constant FSM in the cladding ($d_c/\Lambda = 0.66$). It can be observed that, elliptical holes in the core with a large d_x lead to a large birefringence, and the single polarization can be easily achieved. While due to $d_x < \Lambda$, we only take into account the d_x increased by 9%. In addition, if the major axis d_x decreases 15% ($d_x/\Lambda = 0.765$), the FSM of x-polarized mode is almost the same as the FSM in the cladding. Therefore, in

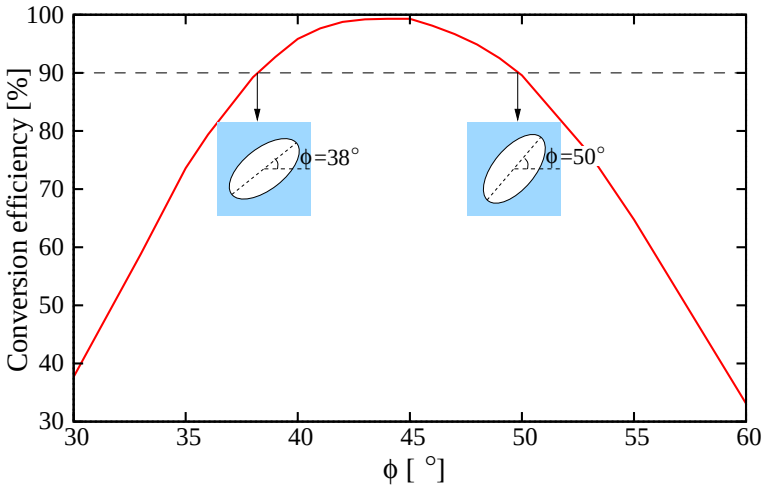

Figure 5.15: Conversion efficiency of the three-core PC element against the inclination angle of elliptical holes in the PC waveguide.

our research, the single-polarization property of xEC-CHF can be achieved with $d_x/\Lambda > 0.765$ by keeping the hole area.

After we discussed the structure tolerance of the single-polarized EC-CHF, we will focus on the inclination angle of the elliptical holes in PC waveguide. As we demonstrated in the last subsection, the PC waveguide whose elliptical hole inclination angle is $\phi = 45°$ can convert an x-polarized incident light by 90 degree with a low ER. If the inclination angle fluctuates, the symmetrical structure of the PC will be destroyed, and the completely polarization conversion will be difficult to achieve. For the three-core PC element, the cross-talk free property still can be achieved since the EC-CHF is used as the output waveguide, while the inclination angle fluctuation leads to a low conversion efficiency. Refer to the three-core PC parameters designed before, the major axis length of elliptical holes in EC-CHF is $d_x/\Lambda = 0.9$, $d_r/\Lambda = 0.798$ for PC waveguide in the middle, $d_c/\Lambda = 0.66$ for the cladding holes, the ellipticity is set to 2, each core is separated from the adjacent cores by three column of air holes, and the device length is fixed to 1550 μm. The conversion efficiency is calculated by

$$\eta = \frac{P_{3y}}{P_{1x}} \times 100\%. \tag{5.4}$$

where P_{3y} is the power of converted y-polarization in the output waveguide (yEC-CHF) and P_{1x} is the power of incident x-polarization in the input waveguide (xEC-

Table 5.2: Conversion efficiency versus the deviation for different parts of the device parameters at each deviation level.

Deviation level	Core region			Cladding region
	xEC-CHF	PC	yEC-CHF	
-0.2%	87.4%	77.3%	87.6%	98.2%
-0.1%	95.7%	92.1%	95.8%	98.3%
0	99.1%	99.1%	99.1%	99.1%
0.1%	95.0%	94.1%	94.8%	98.3%
0.2%	86.1%	81.6%	85.9%	98.1%

CHF). The variation of conversion efficiency against the fluctuated inclination angle is illustrated in Fig. 5.15. It can be observed that the conversion efficiency is better than 90% when the inclination angle is set between $38^\circ \sim 50^\circ$.

Finally, we examined the conversion efficiency versus the deviation for the respective hole sizes of each region, as shown in Table 5.2. Here, all the hole sizes of the deviation part are varied with the same extent, such as if only the elliptical holes in xEC-CHF core region are decreased 0.2%, then the coupling efficiency of the PC element will decrease to 87.4%, because the phase matching condition is mismatched between the xEC-CHF and PC waveguide. In practical manufacturing process, all the hole sizes vary randomly, however, the deviation for one part of the device with same extent leads to a worse conversion efficiency. Here, we investigate the worse conversion efficiency, while a better conversion efficiency can be obtained in the fabrication process. Obviously, the conversion efficiency with the deviation of elliptical holes is much worse than the varies in the cladding. That is because in an EC-CHF the effective index is sensitive to the hole sizes in the core region. So if we design this type of PC using a single-polarized PCF with only circular air holes, such as PCF in [41], it may be possible to obtain a device with larger tolerance.

Chapter 6

Mode Converter/Splitter for MDM/PDM

Mode division multiplexing (MDM) over few-mode fibers is considered as a promising solution for surpassing the capacity limits of single-mode fiber systems. In order to achieve this object, a mode converter could be widely used. In our research, we considering a passive optical device which can contribute to the MDM and PDM system, as shown in Fig. 6.1. If an arbitrary polarized light beam is launched into the input waveguide port 1 in the middle, firstly, the fundamental modes of x- and y-polarization are separated into the port 2 and port 3 by setting the waveguides which satisfied the phase matching condition. Similarly, the 1st-higher-order modes of x- and y-polarization are split into the port 4 and port 5 at the same time. Then, the separated 1st-higher-order modes with different polarization are split and converted into the corresponding fundamental modes, respectively. Therefore, through this kind of optical device, six kinds of different fundamental modes can be separated with an arbitrary polarized incident light, $i.\ e.$ the MDM and PDM system can be achieved simultaneously.

So far, for the passive optical device mentioned above, we have designed the PS element which can achieve the polarization splitting part. Additionally, in this chapter, we propose a novel MCS based on square lattice EC-CHFs, which can easily achieve the mode conversion between the 1st-higher-order mode and fundamental mode.

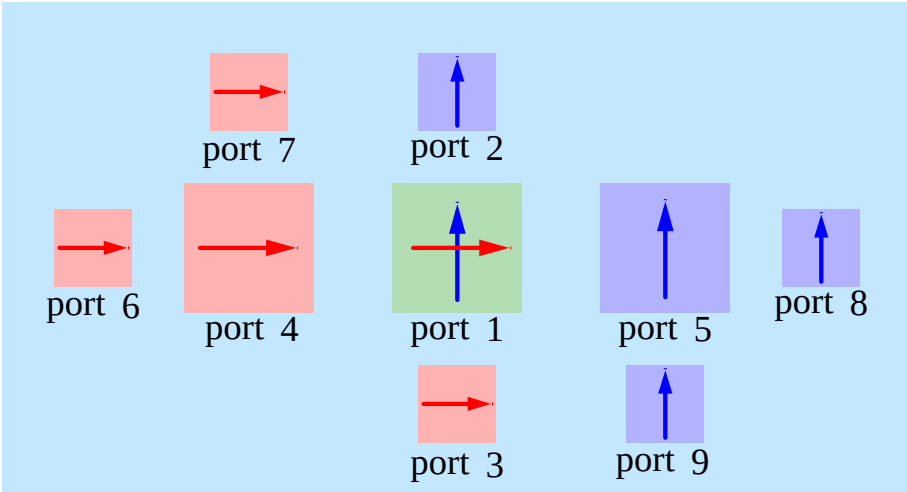

Figure 6.1: Schematic of a passive optical device that can contribute to the MDM and PDM system simultaneously.

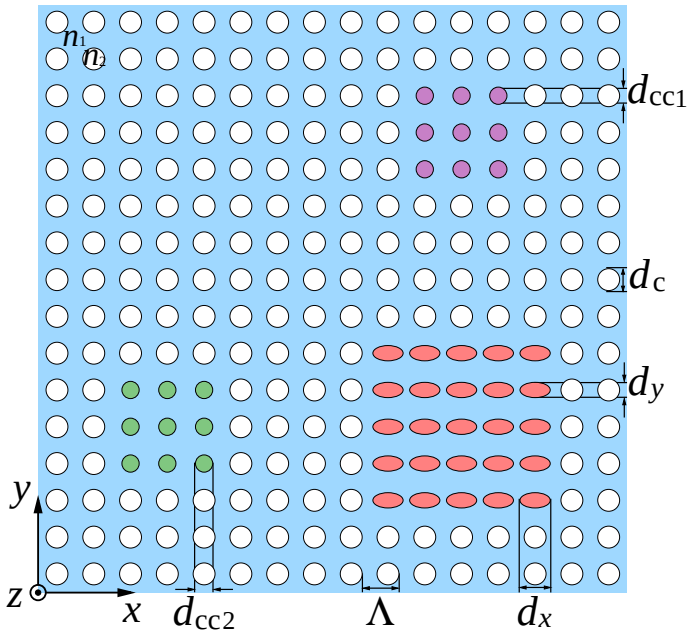

Figure 6.2: Cross section of the MCS.

6.1 Schematic and Design Procedure of MCS

In this section, we will introduce the structure of our proposed MCS and explain the design procedure of it. Figure 6.2 shows the cross-sectional structure of our proposed L-shaped MCS which consists of a multi-core xEC-CHF and two single mode CC-CHFs. If the x-polarized light beam launched into the multi-core xEC-CHF, then by setting appropriate parameters, the fundamental and 1st-higher-order modes are supported in this waveguide. Owing to the birefringence of EC-CHF, the E_{12}^{x} and E_{21}^{x} modes with different symmetries have a slight effective index difference. The E_{12}^{x} mode will only couple into the single-mode CC-CHF at right top, on the contrary, the E_{21}^{x} mode will only couple into the single-mode CC-CHF at left side, which means the mode splitting can be achieved. Due to the reciprocity property of an optical device, if the incident light launched into two CC-CHFs, only the x-polarized component of the incident light couples to the multi-core xEC-CHF, and transmits in the same waveguide. While the y-polarized component remains in the CC-CHF. Therefore, in this study, we estimate the modal effective index of each waveguide and analyze the propagation of incident light by only considering the x-polarized component. Additionally, the MCS for y-polarization can be easily obtained by exchange the multi-core xEC-CHF for a yEC-CHF.

The design procedure of the MCS is given as follows: firstly, we consider a multi-core xEC-CHF which supports only the fundamental and 1st-higher-order modes. Then, the hole sizes of two CC-CHFs are determined by meeting the phase matching condition with E_{12}^{x} mode and E_{21}^{x} mode, respectively. After that, each mode conversion length is calculated by setting a satisfied separation between adjacent cores. Finally, we determine the device length by adapting the average of the two conversion lengths.

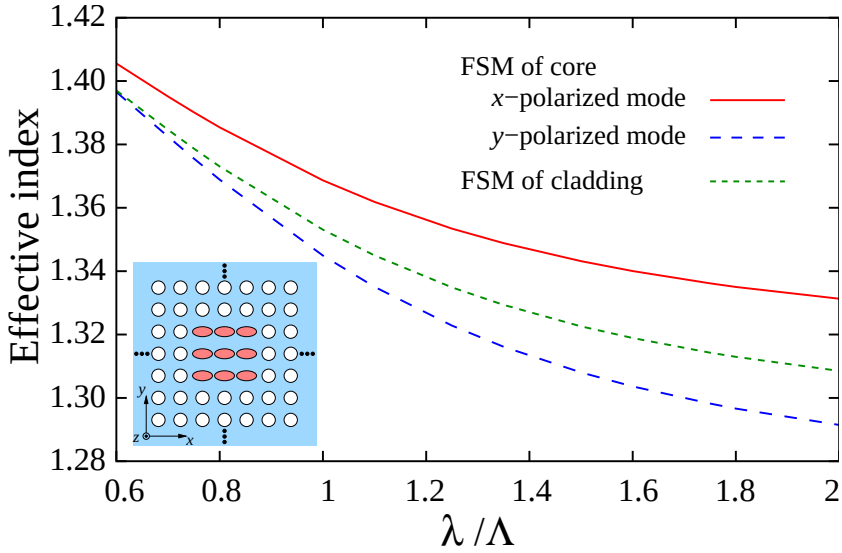

Figure 6.3: Dispersion curve of the one ring core square lattice xEC-CHF.

6.2 Design of MCS Based on Square Lattice EC-CHFs

According to the design procedure of our proposed MCS previously, firstly, we should design a multi-core xEC-CHF which supports the fundamental and 1st-higher-order modes with the wavelength $\lambda = 1.55$ μm. The basic structural parameters of a square lattice xEC-CHF are given as follows: all of the air holes are anchored in a square lattice with the lattice pitch Λ of 1 μm, the refractive indices of the silica and the air are set to $n_1 = 1.45$ and $n_2 = 1$, respectively, the major axis of elliptical hole is $d_x = 0.9\Lambda$, the ellipticity is set to $d_{\text{major}}/d_{\text{minor}} = 2$, and the diameter of the holes in the cladding is $d_c = 0.65\Lambda$. From the dispersion curves of the one ring core square lattice xEC-CHF with determined parameters shown in Fig. 6.3, we observe that the absolutely single polarization transmission can be achieved for the operation wavelength is longer than 0.6 μm.

Then, in order to investigate the number of the modes in an xEC-CHF, we adopt an equivalent square waveguide to obtain the dispersion curves. The schematic diagrams of xEC-CHF and its corresponding equivalent square waveguide are shown in Fig. 6.4. For equivalent waveguide, the effective indices of the core and cladding are determined as the same as the effective indices of the FSMs on those region for the xEC-CHF, respectively.

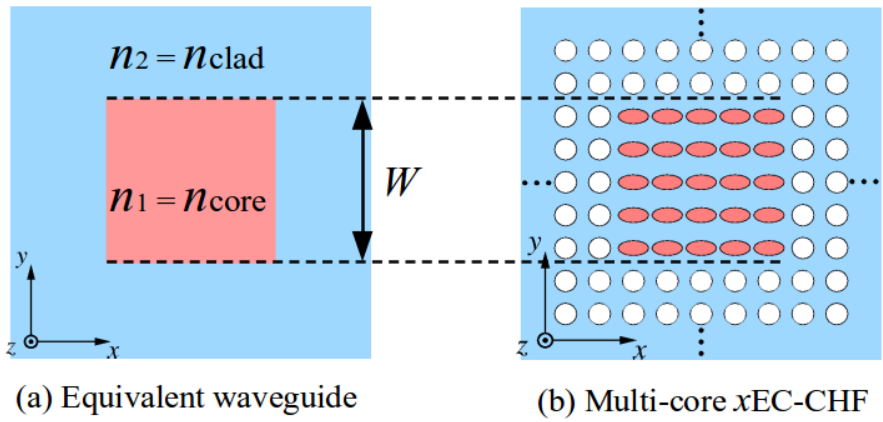

Figure 6.4: Schematic diagrams of xEC-CHF and its corresponding equivalent square waveguide.

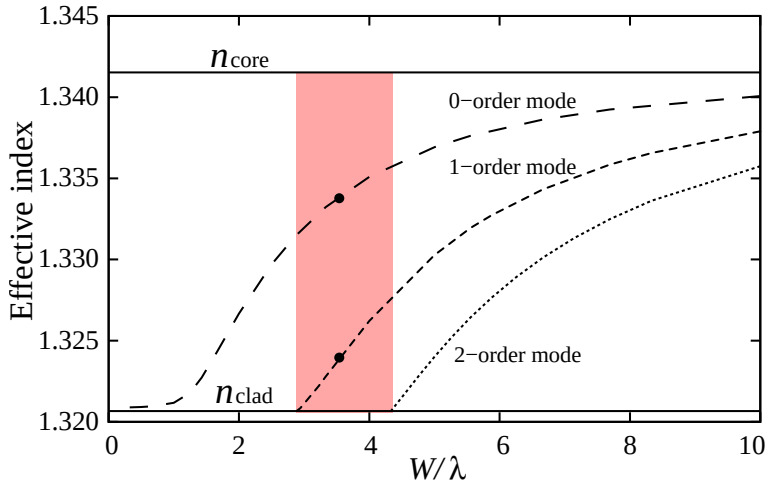

Figure 6.5: Core width dependence of the effective index for a square lattice EC-CHF at $\lambda = 1.55\ \mu$m.

Fig. 6.5 shows the core width W dependence of the effective index for the equivalent square waveguide. We can observe that in the shaded area ($4.48\ \mu$m$< W < 6.72\ \mu$m), the xEC-CHF supports fundamental mode and 1st-higher-order mode. Here, we adopt a 2-ring xEC-CHF whose core width is $W = 5\ \mu$m to design the MCS. The structural parameters are set as the same as mentioned in the previous subsection, the major axis of ellipses is $d_x = 0.9\Lambda$, the diameter of circular holes in the cladding is $d_c = 0.65\Lambda$. The cross-sectional view of 2-ring xEC-CHF and the magnetic field distribution of each eigenmode are illustrated in Fig. 6.6. In order to show the core region clearly in the magnetic field distribution, we use

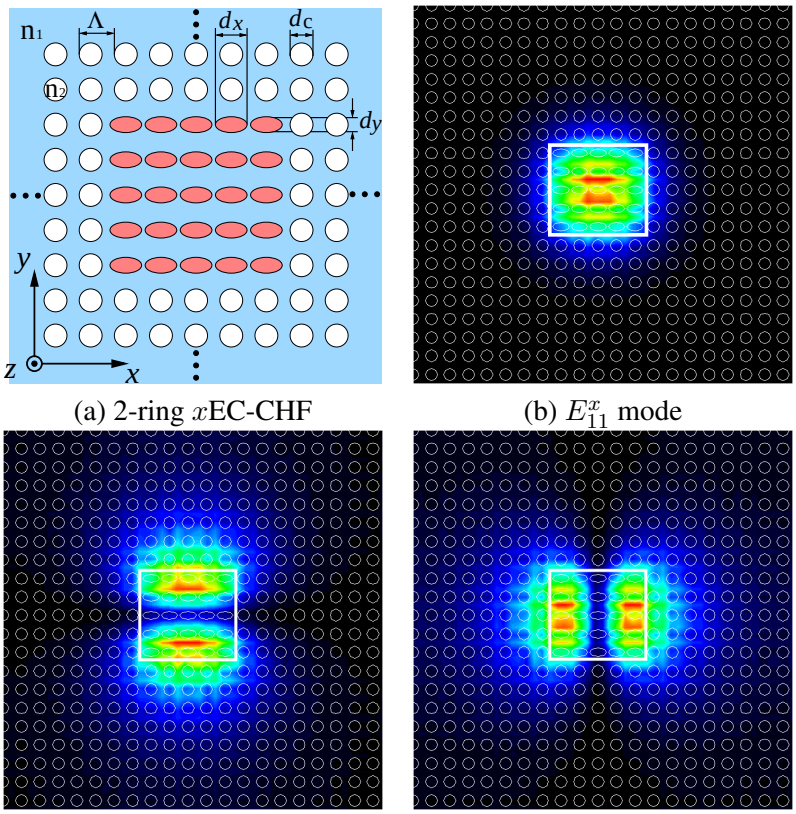

(a) 2-ring xEC-CHF (b) E^x_{11} mode

(c) E^x_{12} mode (d) E^x_{21} mode

Figure 6.6: (a) Cross section of the xEC-CHF and the magnetic field distribution of (b) E^x_{11} mode, (c) E^x_{12} mode, (d) E^x_{21} mode at $\lambda = 1.55$ μm.

white wire frame to emphasize the core region of EC-CHF.

In order to reduce the insertion loss, it is necessary to satisfy the phase matching condition between xEC-CHF and CC-CHFs according to the coupled mode theory. Since the E^x_{12} and E^x_{21} modes have different symmetry axes, the E^x_{12} mode of xEC-ECF couples to the CC-CHF above, and the E^x_{21} mode couples to the CC-CHF at left side. We design the hole size of two CC-CHFs using the effective index of waveguide to satisfy the phase matching condition. The effective index of the CC-CHF against air hole size in the core region is shown in Fig. 6.7. Two horizontal lines represent the effective indices of E^x_{12} and E^x_{21} modes in the isolated system, respectively. The phase matching hole size for the CC-CHF above is $d_{cc1} = 0.616\Lambda$, and the CC-CHF at left side is $d_{cc2} = 0.619\Lambda$. Moreover, the core gap between xEC-CHF and two CC-CHFs are set to the same which are also important parameters. Large core gap leads to a long conversion length, while too small core gap leads

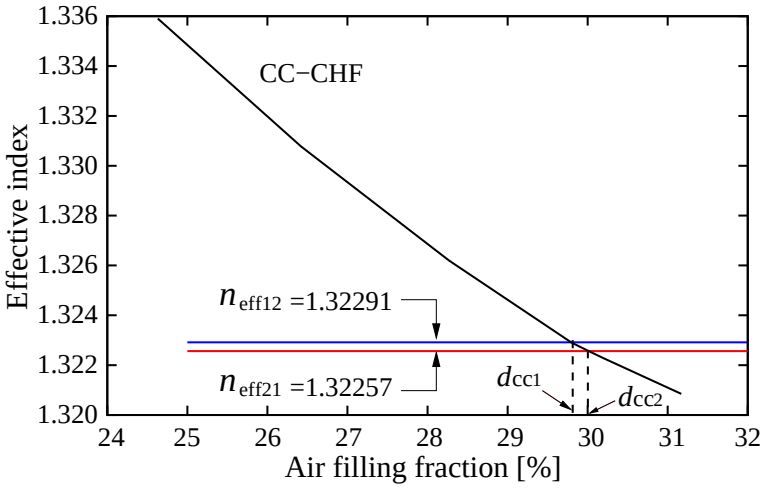

Figure 6.7: Effective index of the CC-CHF as a function of the air filling fraction.

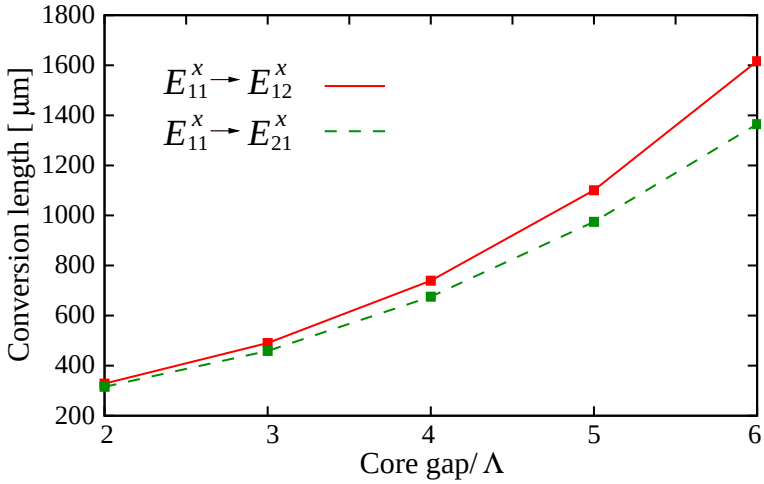

Figure 6.8: Core gap dependence of the conversion length for each mode conversion.

to a strong coupling between two CC-CHFs, which makes an influence for the coupling efficiency. The core gap dependence of the conversion length for each mode conversion is illustrated in Fig. 6.8. Here, we adopt 4 rows or columns of air holes between the xEC-CHF and CC-CHFs.

Magnetic field distributions of even and odd modes for each coupled system are illustrated in Fig. 6.9. Additionally, the effective index of each coupled mode is also given in Fig. 6.9. The mode conversion length can be calculated by $L = 0.5\lambda/(n_{\mathrm{e}} - n_{\mathrm{o}})$, where n_{e} and n_{o} represent the effective indices of even and odd modes, respectively. The calculated conversion length of vertical coupled system

(E_{11}^{x} mode to E_{12}^{x} mode) is $L_1 = 740$ μm, and the conversion length of horizontal coupled system (E_{11}^{x} mode to E_{21}^{x} mode) is $L_2 = 676$ μm. In order to reduce the loss caused by the difference between two conversion lengths, we determined the device length as the average of the two conversion lengths, $i.\ e.\ L = 708$ μm. The normalized power against the propagation distance is shown in Fig. 6.10, at $z = 708$ μm the loss caused by the difference between two conversion lengths is lower than 0.1%.

We simulated the propagation behavior of incident light through our proposed MCS as shown in Fig. 6.11. It can be observed that after x-polarized fundamental modes launched into the CC-CHFs, light in each port can be totally converted into the corresponding 1st-higher-order mode and coupled to the same xEC-CHF.

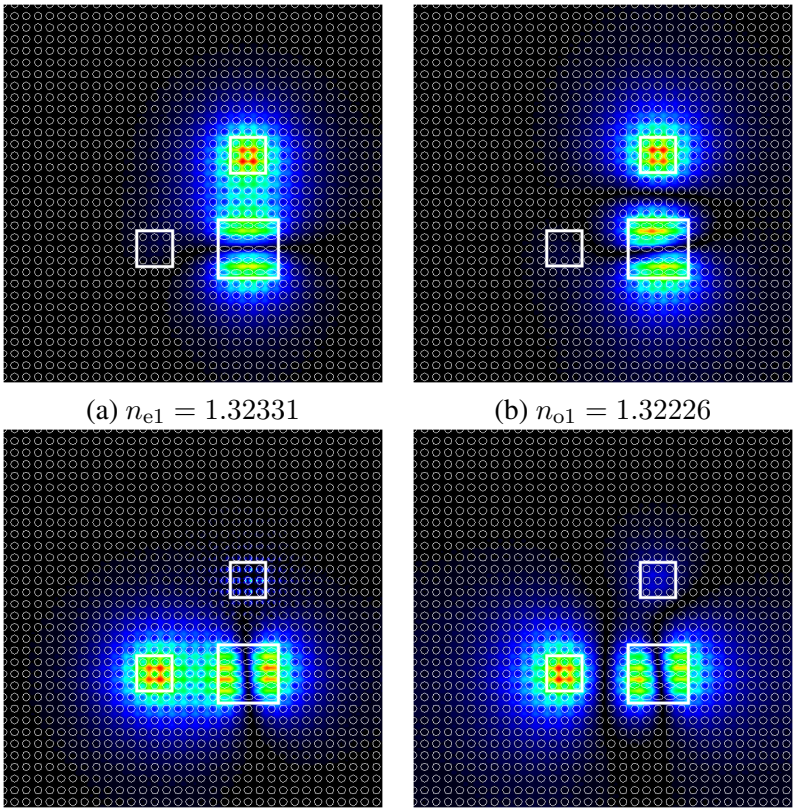

(a) $n_{e1} = 1.32331$ (b) $n_{o1} = 1.32226$

(c) $n_{e2} = 1.32295$ (d) $n_{o2} = 1.32180$

Figure 6.9: Magnetic field distribution of even and odd modes of (a),(b) longitudinal coupled system, (c),(d) transversal coupled system and their corresponding effective indices.

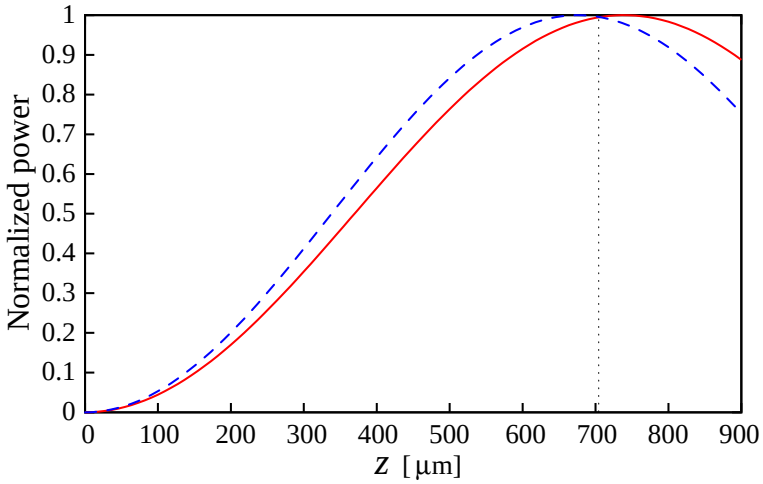

Figure 6.10: Normalized power against the propagation distance.

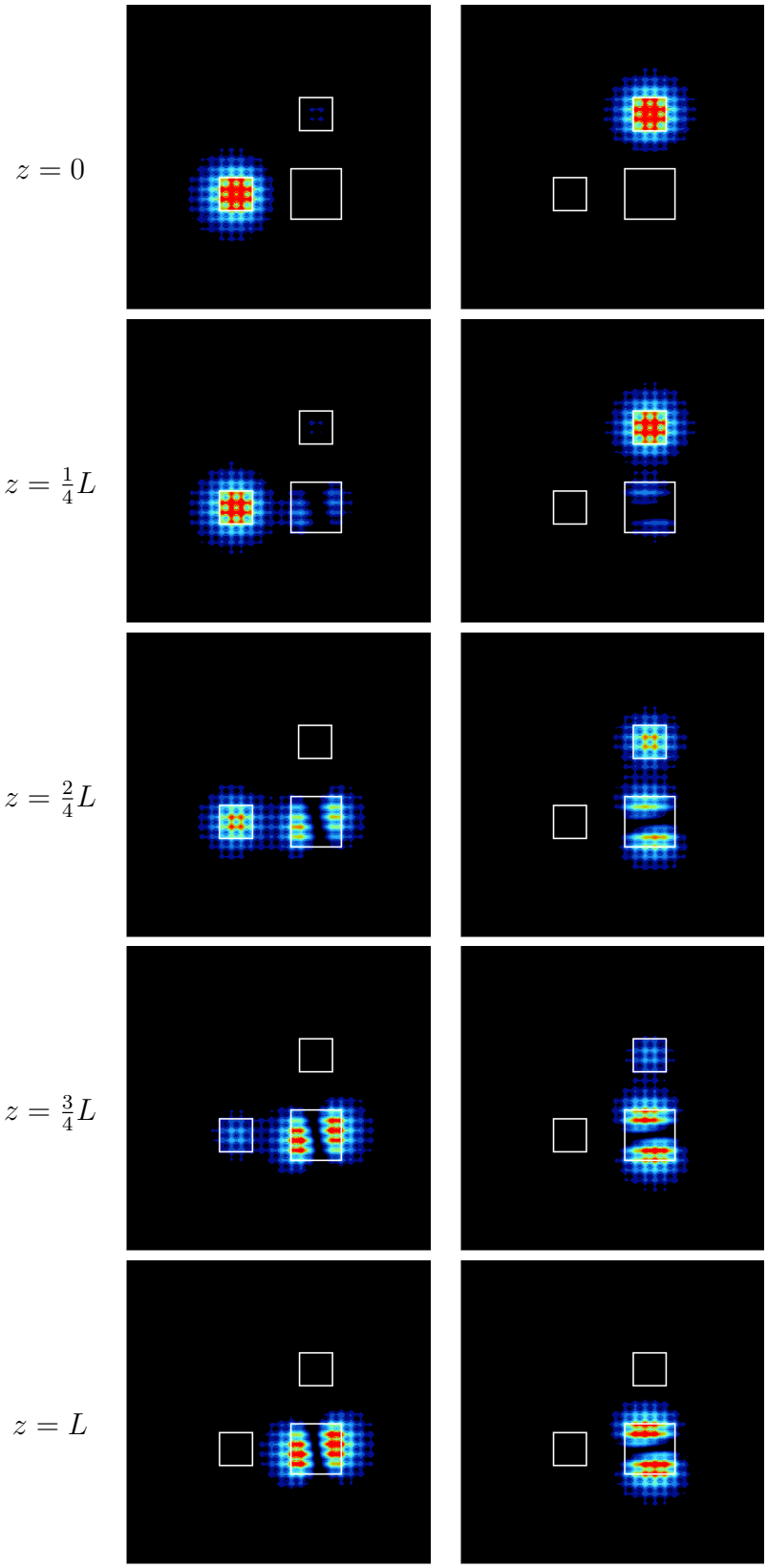

Figure 6.11: Light propagation behavior in our MCS (x-polarized component,$L = 708$ μm).

6.3 Improved MCS

So far, an MCS based on square lattice EC-CHFs has been proposed, however, from the FE-BPM simulated light propagation behavior, we note that the converted 1st-higher-modes (E^x_{12} and E^x_{21} modes) have the oblique magnetic field distributions, respectively. In this section, we will optimize the structural parameters of the MCS to realize the mode converting and splitting with a pretty magnetic field distribution. Firstly, from the magnetic field distributions of the coupled modes shown in Fig. 6.9, it can be observed that the odd mode of the longitudinal coupled system and the even mode of the transversal coupled system have the obvious oblique distributions, and the effective indices of the two coupled modes are extremely close. Therefore, the coupling between this two coupled modes may be the reason of the oblique magnetic field distribution. Moreover, 4 rows or columns of the air holes between the adjacent cores have been adopted to consist the MCS, we can see that a strong coupling between the CC-CHF and xEC-CHF occurred. Pretty magnetic field distribution may obtained with a large core gap.

According to the above considerations, we adopt the following measures: firstly, in order to avoid the unwanted coupling for the coupled system, we expand the effective index difference between the E^x_{12} and E^x_{21} modes in isolated system to ensure that the coupled modes have a large effective index difference between each other. Then, the core gap should be enlarged to realize the pretty magnetic field distributions of the coupled modes.

In order to expand the effective index difference between the E^x_{12} and E^x_{21} modes in isolated system, firstly, we investigate the hole size dependence of the effective index difference, as shown in Fig. 6.12. For the 2-ring xEC-CHF, the ellipticity of the elliptical holes in the core is remained as 2, the effective index difference is represented by $\Delta = n_{\text{eff},12} - n_{\text{eff},21}$, where $n_{\text{eff},12}$ and $n_{\text{eff},21}$ are the effective indices of E^x_{12} and E^x_{21} modes, respectively. We can observed that large hole size in the cladding leads to a relatively high Δ, and for a constant hole size in the cladding region, the Δ has a peak value with the variation of the elliptical holes in the core. The effective index difference of the xEC-CHF with initial parameters ($d_c/\Lambda = 0.65$, $d_x/Lambda = 0.9$) is $\Delta = 4.24 \times 10^{-4}$. Here, we chose an xEC-CHF with large index difference of 5.34×10^{-4} to design the MCS, and the hole sizes

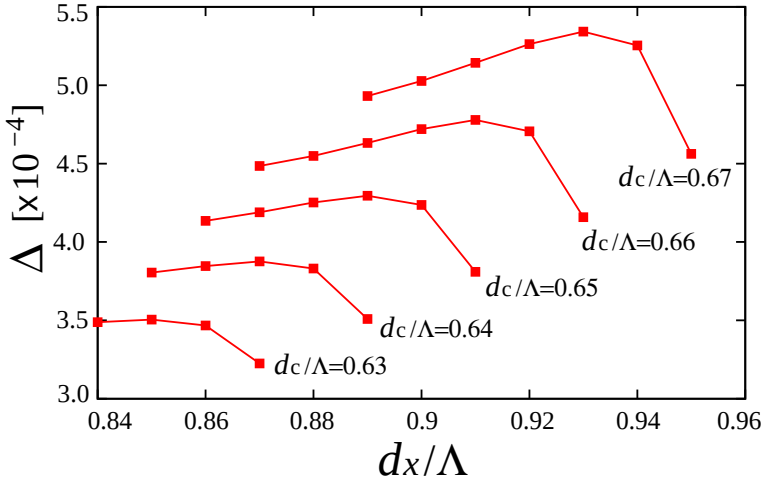

Figure 6.12: Hole size dependence of the effective index difference between E^x_{12} and E^x_{21} modes.

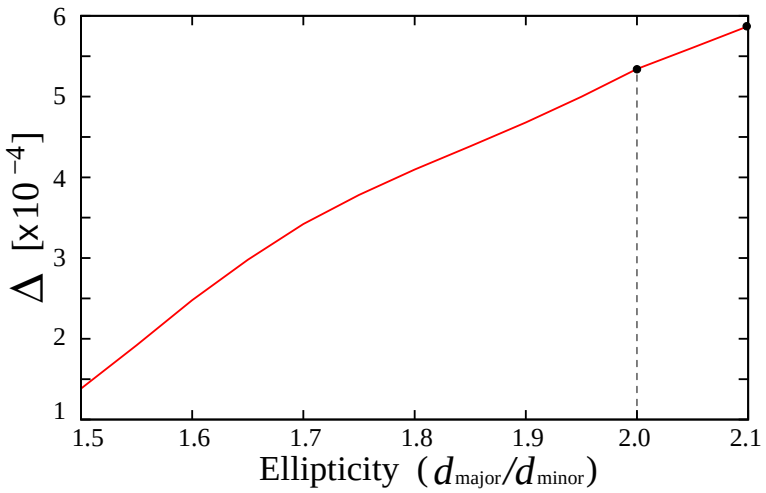

Figure 6.13: Ellipticity dependence of the effective index difference between E^x_{12} and E^x_{21} modes.

are set to $d_c/\Lambda = 0.67$ and $d_x/\Lambda = 0.93$. Next, the variation of effective index difference against the ellipticity of the ovals in the core has also been investigated, as shown in Fig. 6.13. The ellipticity varies from 1.5 to 2.1 by keeping the elliptical hole area. It is evident from this figure that the Δ increases by increasing the ellipticity. With $d_{\text{major}}/d_{\text{minor}} = 2.1$, the Δ reaches 5.87×10^{-4}, however, the major axis of the elliptical hole is $d_x/\Lambda = 0.953$ which is very close to the lattice pitch Λ and this could lead to a complex manufacturing process. Therefore, we still adopt the ellipticity as 2. Additionally, in order to realize the pretty magnetic field distributions of the coupled modes, 7 rows or columns of air holes have been used

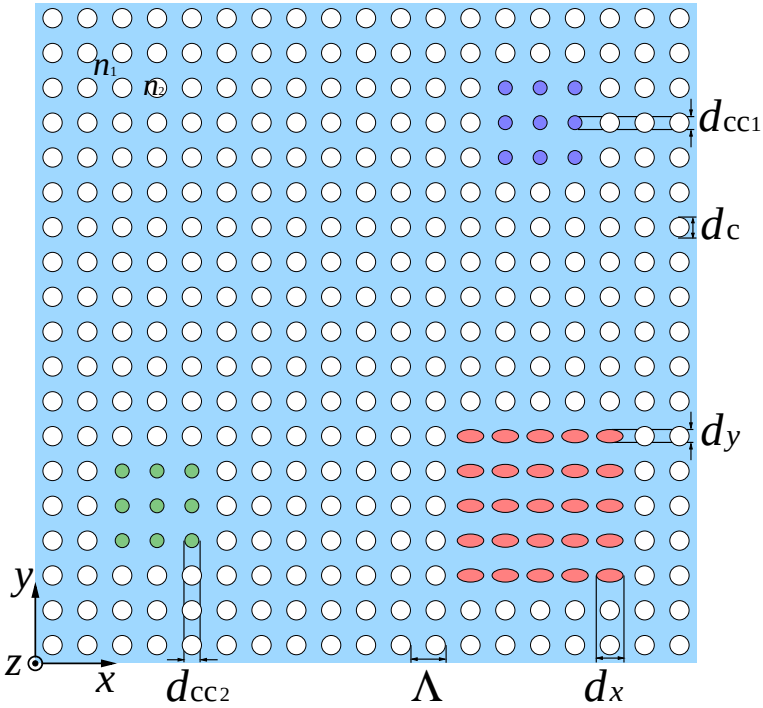

Figure 6.14: Improved MCS with 7 columns air holes between the adjacent cores.

between the adjacent cores.

Fig. 6.14 illustrates the structure of the improved MCS, and fundamental parameters are set as follows: all of the air holes are anchored in a square lattice with the lattice pitch Λ of 1 μm, the indices of the silica and air are set to $n_1 = 1.45$ and $n_2 = 1$, respectively, the operation wavelength is $\lambda = 1.55\mu$m, the major axis of elliptical holes in the 2-ring xEC-CHF is $d_x/\Lambda = 0.93$, the ellipticity is $d_{\text{major}}/d_{\text{minor}} = 2$, the diameter of the circular holes in the cladding is $d_c/\Lambda = 0.67$. Based on the above parameters, same as the design process in the previous section, the hole sizes of the two CC-CHFs can be determined by satisfying the phase matching condition with E^x_{12} and E^x_{21} modes, respectively. The corresponding hole size for the CC-CHF above is $d_{cc1}/\Lambda = 0.6316$, for the left CC-CHF is $d_{cc1}/\Lambda = 0.6343$.

For the improved MCS, the magnetic field distribution of even and odd modes of each coupled system are illustrated in Fig. 6.15. Additionally, the effective index of each coupled mode is also given in Fig. 6.15. The calculated mode conversion length of vertical coupled system (E^x_{11} mode to E^x_{12} mode) is $L_1 = 3249$ μm, and the conversion length of horizontal coupled system (E^x_{11} mode to E^x_{21} mode) is

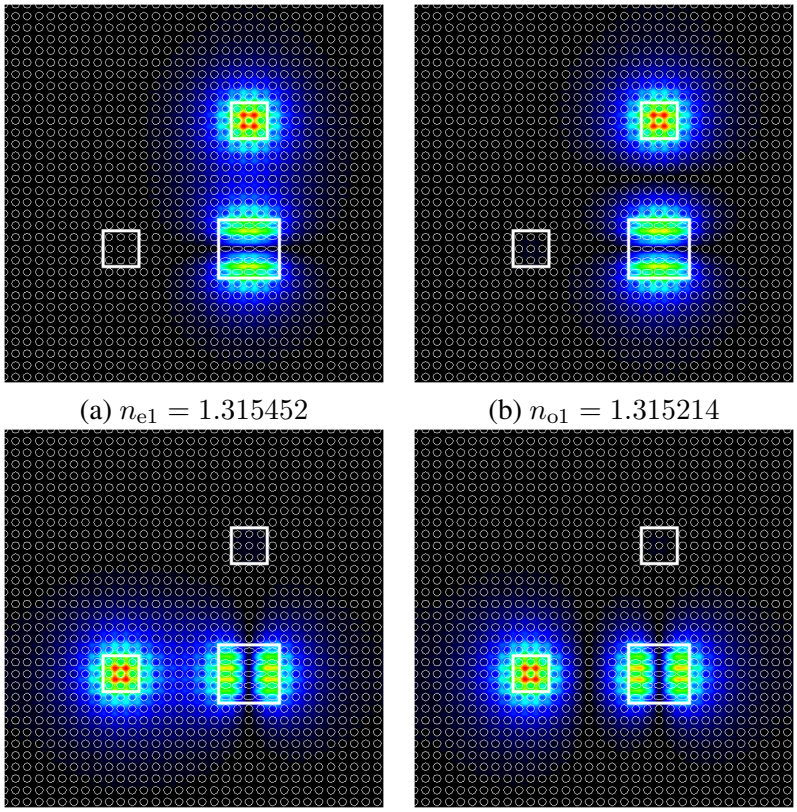

(a) $n_{\mathrm{e1}} = 1.315452$ (b) $n_{\mathrm{o1}} = 1.315214$

(c) $n_{\mathrm{e2}} = 1.314946$ (d) $n_{\mathrm{o2}} = 1.314645$

Figure 6.15: Magnetic field distributions of the improved MCS. Even and odd modes and their corresponding effective indices for (a),(b) longitudinal coupled system, (c),(d) transversal coupled system.

$L_2 = 2577$ μm. The device length is set to $L = 2913$ μm, and the loss caused by the difference between two conversion lengths is lower than 0.01%. We simulated the propagation behavior of incident light through our proposed MCS as shown in Fig. 6.16. It can be observed that after x-polarized fundamental modes launched into the CC-CHFs, light in each port can be totally converted into the corresponding 1st-higher-order mode perfectly and coupled to the same xEC-CHF.

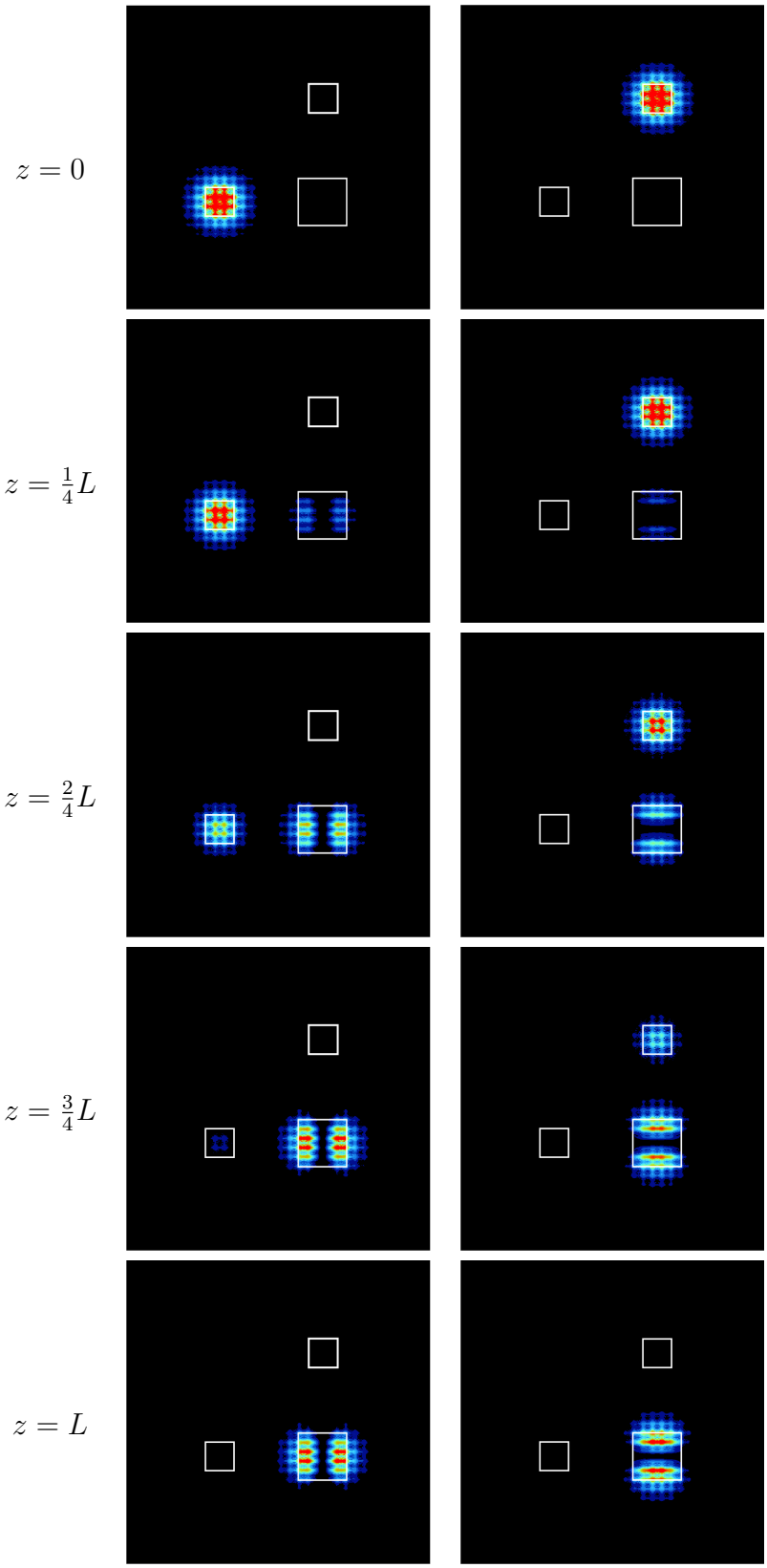

Figure 6.16: Light propagation behavior in the improved MCS (x-polarized component, $L = 2913\ \mu$m).

Chapter 7

Conclusions and Future Work

7.1 Conclusions

In this thesis, three kinds of passive optical devices, which are widely used in the optical communication system, have been proposed and studied based on single-polarized EC-CHF. So far, the ER of an passive optical device is a key performance parameter, and a better ER with a wide bandwidth is one of the important evaluation criteria for most researches. Utilizing the single polarization transmission property of EC-CHF, simulation results demonstrated that our proposed optical devices (PS, PC and MCS) can achieve the cross-talk free with a wide bandwidth.

In the first two chapters, we have reviewed the backgrounds of this study.

In chapter 1, with the development of information society, several important passive optical devices used in the communication system have been briefly introduced. In order to obtain the high-performance optical devices, numbers of designs based on PCF have been given in recent decades. So far, since the proposed optical devices have to consider the ER, we illustrated the main objective of our research, to realize the cross-talk free optical devices.

In chapter 2, we shown two main categories of the PCF with different light wave guided mechanisms, and given the schematic for each kind of PCF. In our research, we designed optical devices based on EC-CHFs, here, two kinds of EC-CHFs with different arrangement of air holes, $i.\ e.$ the triangular lattice EC-CHF and square lattice EC-CHF, have been illustrated.

In chapter 3, we explained the analysis method that we used in this research, the formulations of FV-FEM and full-vectorial FE-BPM have been given. Moreover,

the FSM of PCF has also been briefly introduced.

After that, in the next three chapters, we designed three kinds of passive optical devices based on the single-polarized EC-CHF, and their structural parameters, light propagation behaviors, and structural tolerance have been also discussed in detail.

In chapter 4, we proposed a novel PS element by using three triangular lattice EC-CHFs. Simulation results demonstrated that, with a wide bandwidth ($\lambda > 0.6$ μm for the PS with large hole EC-CHF, $\lambda > 0.7$ μm for the PS with small hole EC-CHF), the PS can completely split an arbitrarily polarized light beam into two orthogonal polarization states without any cross-talk. Since the coupling lengths for two orthogonally polarized waves are almost the same, this makes the splitter easy to design. Additionally, the simulated results demonstrated that PS with small air hole EC-CHF has a relative large tolerance and its coupling efficiency is better than 20 dB with a wavelength bandwidth of 160 nm.

In chapter 5, firstly, we proposed a novel single PC element based on square lattice EC-CHF. With nine 45-degree oblique elliptical air holes in the core, an incident orthogonal polarization can be converted 90 degrees through this symmetrical PC element. A design example shown that the ER of the single PC is better than -23 dB with the conversion length is only 31.7 μm. After that, we adopted two EC-CHFs on both sides of the PC to obtain a cross-talk free structure. The ER of our proposed three-core PC element is infinitely small for $\lambda > 0.75$ μm.

In chapter 6, we considered a L-shaped MCS based on square lattice EC-CHF to achieve the mode splitting and converting simultaneously. Since the EC-CHF has a large birefringence in the core, simulation results demonstrated that the input waveguide supports the x-polarized 1st-higher-modes (E^x_{12} mode and E^x_{21} mode), and they have different symmetry along the x- and y-axis. With the incident light is launched into the multi-core xEC-CHF, E^x_{12} and E^x_{21} modes can be converted into the corresponding fundamental modes and transmitted through each output CC-CHF, respectively.

As briefly mentioned in the previous chapters, passive optical devices based on single-polarized EC-CHF can achieve the cross-talk free property with a wide bandwidth. In addition, our proposed devices have a high design flexibility. Such

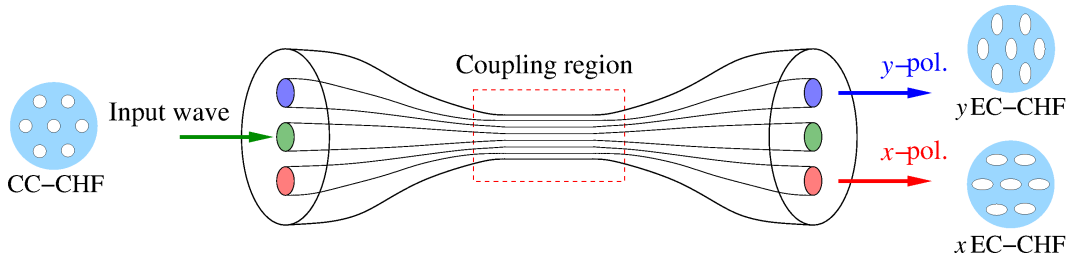

Figure 7.1: Schematic of the taper coupler type PS.

as a novel PSC based on PCF can be obtained by combining the PS and PC we have designed. Moreover, a high-performance optical device based on our proposed PS and MCS can make a contribution to the PDM and MDM system.

7.2 Future Work

In the future, we will continue to investigate high-performance optical devices based on single-polarization PCFs. Following directions are worthwhile to the future works based on the work we have conducted in this thesis.

- Considering the current fabrication technology of PCF, the manufacturing process of air holes has not reached a high accuracy, especially for the elliptical air holes. Therefore, in order to obtain the high tolerance optical devices, instead of the elliptical air holes, the discussion about cross-talk free devices based on single-polarized PCFs with only circular air holes are needed, such as the PCF in [41].

- As shown in Fig. 7.1, optical devices with a taper structure [94],[95] for the mode coupling region should be investigated to increase the structural tolerance.

Reference

[1] J. Jiang, J. Cai, G. P. Nordin, and L. Li, "Parallel microgenetic algorithm design for photonic crystal and waveguide structures," *Opt. Lett.*, vol. 28, issue 23, pp. 2381-2383, Dec. 2003.

[2] Y. Sakamaki, T. Saida, T. Hashimoto, and H. Takahashi, "New optical waveguide design based on wavefront matching method," *J. Lightw. Technol.*, vol. 25, no. 11, pp. 3511-3518, Nov. 2007.

[3] J. S. Jensen and O. Sigmund, "Systematic design of photonic crystal structures using topology optimization: Low-loss waveguide bends," *Appl. Phys. Lett.*, vol. 84, no. 12, pp. 2022-2024, Mar. 2004.

[4] J. S. Jensen, O. Sigmund, L. H. Frandsen, P. I. Borel, A. Harpoth, and M. Kristensen, "Topology design and fabrication of an efficient double 90° photonic crystal waveguide bend," *IEEE Photon. Technol. Lett.*, vol. 17, issue 6, pp. 1202-1204, Jun. 2005.

[5] R. Matzen, J. S. Jensen, and O. Sigmund, "Topology optimization for transient response of photonic crystal structures," *J. Opt. Soc. Amer. B*, vol. 27, issue. 10, pp. 2040-2050, 2010.

[6] F. Wang, J. S. Jensen, and O. Sigmund, "Robust topology optimization of photonic crystal waveguides with tailored dispersion properties," *J. Opt. Soc. Amer. B*, vol. 28, issue 3, pp. 387-397, 2011.

[7] L. Frandsen, Y. Elesin, L. Frellsen, M. Mitrovic, Y. Ding, O. Sigmund, and K. Yvind, "Topology optimized mode conversion in a photonic crystal waveguide fabricated in silicon-on-insulator material," *Opt. Express*, vol. 22, issue 7, pp. 8525-8532, Apr. 2014.

[8] H. Men, K. Y. K. Lee, R. M. Freund, J. Peraire, and S. G. Johnson, "Robust topology optimization of three-dimensional photonic-crystal band-gap structures," *Opt. Express*, vol. 22, issue 19, pp. 22632-22648, May 2014.

[9] Y. Tsuji, K. Hirayama, T. Nomura, K. Sato, and S. Nishiwaki, "Design of optical circuit devices based on topology optimization," *IEEE Photon. Technol. Lett.*, vol. 18, issue 7, pp. 850-852, Apr. 2006.

[10] Y. Tsuji and K. Hirayama, "Design of optical circuit devices using topology optimization method with function-expansion-based refractive index distribution," *IEEE Photon. Technol. Lett.*, vol. 20, issue 12, pp. 982-984, Jun. 2008.

[11] K. Fujimoto, Y. Tsuji, K. Hirayama, T. Yasui, S. Sato, and R. Kijima, "A study on topology optimization of optical circuits consisting of multi-materials," *J. Lightw. Technol.*, vol. 30, issue 13, pp. 2210-2215, Apr. 2012.

[12] T. Yasui, Y. Tsuji, J. Sugisaka, and K. Hirayama, "Design of three-dimensional optical circuit devices by using topology optimization method with function-expansion-based refractive index distribution," *J. Lightw. Technol.*, vol. 31, issue 23, pp. 3765-3770, Dec. 2013.

[13] M. Kasahara, K. Saitoh, T. Sakamoto, N. Hanzawa, T. Matsui, K. Tsujikawa, F. Yamamoto, and M. Koshiba, "Design of few-mode fibers for mode-division multiplexing transmission," *IEEE Photon. J.*, vol. 31, issue 23, pp. 3765-3770, Dec. 2013.

[14] K. Shi, F. Feng, G. S. D. Gordon, T. D. Wilkinson, and B. C. Thomsen, "SLM-based mode division multiplexing system with 6×6 sparse equalization," *IEEE Photon. Technol. Lett.*, vol. 27, no. 16, pp. 1687-1690, Aug. 2015.

[15] J. C. Knight, T. A. Birks, P. St. J. Russell, and D. M. Atkin, "All-silica single-mode optical fiber with photonic crystal cladding," *Opt. Lett.*, vol. 21, issue 19, pp. 1547-1549, Oct. 1996.

[16] J. Broeng, D. Mogilevstev, E. Barkou, and A. Bjarklev, "Photonic crystal fibers: A new class of optical waveguides," *Opt. Fiber Lett.*, vol. 5, pp. 305-330, 1999.

[17] J. C. Knight, "Photonic crystal fibers," *Nature*, vol. 424, pp. 847-851, Aug. 2003.

[18] P. St. J. Russell, "Photonic-crystal fibers," *J. Ligthw. Technol.*, vol. 24, no. 12, pp. 4729-4749, Dec. 2006.

[19] T. A. Birks, J. C. Knight, P. St. J. Russell, "Endlessly single-mode photonic crystal fiber," *Opt. Lett.*, vol. 23, no. 13, pp. 961-963, Jul. 1997.

[20] R. F. Cregan, B. J. Mangan, J. C. Knight, T. A. Birks, P. St. J. Russell, P. J. Roberts, and D. C. Allan, "Single-modephotonic band gap guidance of light in air," *Science*, vol. 285, no. 3, pp. 1537-1539, Sep. 1999.

[21] G. Kim, K. Hwang, K. Lee, K.S. Lee, Y.-G. Han, and S.B. Lee, "Experimental study of an elliptical-core photonic bandgap fiber with thin core wall and high aspect ratio and its birefringence characteristics," *Appl. Phys. B*, vol. 101, no. 3, pp. 583-586, Nov. 2010.

[22] K. Z. Aghaie, V. Dangui, M. J. F. Digonnet, S. Fan, and G. S. Kino, "Classification of the core modes of hollow-core photonic-bandgap fibers," *J. Quantum Electron.*, vol. 45, no. 9, pp. 1192-1200, Sep. 2009.

[23] T. Okoshi, "Single-polarization single-mode optical fibers," *IEEE J. Quantum Electron.*, vol. 17, no. 6, pp. 879-884, Jun. 1981.

[24] K. S. Chiang, "Stress-induced birefringence fibers designed for single-polarization single-mode operation," *J. Ligthw. Technol.*, vol. 7, no. 2, pp. 436-447, Feb. 1989.

[25] R. Goto, S. D. Jackson, and K. Takenaga, "Single-polarization operation in birefringent all-solid hybrid microstructured fiber with additional stress applying parts," *Opt. Lett.*, vol. 34, no. 20, pp. 3119-3121, Oct. 2009.

[26] K. Satioh and M. Koshiba, "Single-polarization single-mode photonic crystal fibers," *IEEE Photon. Technol. Lett.*, vol. 15, no. 10, pp. 1384-1386, Oct. 2003.

[27] H.Kubota, S. Kawanishi, S.Koyanagi,M.Tanaka, and S.Yamaguchi, "Absolutely single polarization photonic crystal fiber," *IEEE Photon. Technol. Lett.*, vol. 16, no. 1, pp. 182-184, Jan. 2004.

[28] J. R. Folkenberg, M. D. Nielsen, and C. Jakobsen, "Broadband single-polarization photonic crystal fiber," *Opt. Lett.*, vol. 30, no. 12, pp. 1446-1448, Jun. 2005.

[29] T. Schreiber, F. Röser, O. Schmidt, and J. Limpert, "Stress-induced single-polarization single transverse mode photonic crystal fiber with low non-linerarity," *Opt. Express*, vol. 13, no. 19, pp. 7621-7630, Sep. 2005.

[30] F. Zhang, M. Zhang, X. Liu, and P. Ye, "Design of wideband single-polarization single-mode photonic crystal fiber," *J. Ligthw. Technol.*, vol. 25, no. 5, pp. 1184-1189, May 2007.

[31] J. Ju, W. Jin, and M. S. Demokan, "Design of single-polarization singlemode photonic crystal fiber at 1.30 and 1.55 μm," *J. Lightw. Technol.*, vol. 24, no. 2, pp. 825-830, Feb. 2006.

[32] M. Szpulaka, T. Martynkiena, J. Olszewskia, W. Urbanczyka, T. Nasilowskib, F. Berghmansb, and H. Thienpont, "Single-polarization single-mode photonic band gap fiber," *ACTA Phy. Pol. A*, vol. 111, no. 2, pp. 239-245, 2007.

[33] M. J. Steel and R. M. Osgood, "Polarization and dispersive properties of elliptical-hole photonic crystal fibers," *J. Lightw. Technol.*, vol. 19, no. 4, pp. 495-503, Apr. 2001.

[34] M. Eguchi and Y. Tsuji, "Single-mode single-polarization holey fiber using anisotropic fundamental space-filling mode," *Opt. Lett.*, vol. 32, no. 15, pp. 2112-2114, Aug. 2007

[35] M. Eguchi and Y. Tsuji, "Design of single-polarization elliptical-hole core circular-hole holey fibers with zero dispersion at 1.55 μm," *J. Opt. Soc. Am. B*, vol. 25, no. 10, pp. 1690-1701, Oct. 2008.

[36] M. Eguchi, and Y. Tsuji, "Single-polarization elliptical-hole lattice core photonic-bandgap fiber," *J. Lightw. Technol.*, vol. 31, no. 1, pp. 177-182, Jan. 2013.

[37] A. Cerqueira S. Jr., D. G. Lona, I. de Oliveira, H. E. Hernandez-Figueroa, and H. L. Fragnito, "Broadband single-polarization guidance in hybrid photonic crystal fibers," *Opt. Lett.*, vol. 36, no. 2, pp. 133-135, Jan. 2011.

[38] D. Hu, P. Shum, C. Lu, X. Yu, G. Wang, and G. Ren, "Holey fiber design for single-polarization single-mode guidance," *Appl. Opt.*, vol. 48, no. 20, pp. 4038-4043, Jul. 2009.

[39] F. Zhang, M. Zhang, X. Liu, and P. Ye, "Design of wideband single-polarization single-mode photonic crystal fiber," *J. Lightw. Technol.*, vol. 25, no. 5, pp. 1184-1189, May 2007.

[40] N. Chen, J. Liang, and L. Ren, "High-birefringence low-loss porous fiber for single-mode terahertz-wave guidance," *Appl. Opt.*, vol. 52, no. 21, pp. 5297-5302, Jul. 2013.

[41] K. Ichikawa, Z. Zhang, Y. Tsuji, and M. Eguchi, "A single-polarization holey fiber with anisotropic lattice of circular air holes," *J. Lightw. Technol.*, vol. 33, no. 18, pp. 3866-3871, Sep. 2015.

[42] W. J. Wadsworth, R. M. Percival, G. Bouwmans, J. C. Knight, and P. St. J. Russell, "High power air-clad photonic crystal fiber laser," *Opt. Express.*, vol. 11, no. 1, pp. 48-53, Jan. 2003.

[43] L. Michaille, C. R. Bennett, D. M. Taylor, T. J. Shepherd, J. Broeng, H. R. Simonsen, and A. Petersson, "Phase locking and supermode selection in multicore photonic crystal fiber lasers with a large doped area," *Opt. Lett.*, vol. 30, no. 13, pp. 1668-1670, Jul. 2005.

[44] L. Limpert, T. Schreiber, S. Nolte, H. Zellmer, A. Tunnermann, R. Iliew, F. Lederer, J. Broeng, G. Vienne, A. Petersson, and C. Jakobsen, "High-power air-clad large-mode-area photonic crystal fiber laser," *Opt. Express.*, vol. 11, no. 7, pp. 818-823, Apr. 2003.

[45] Y. Wang, W. Jin, L. Jin, X. Tan, H. Bartelt, W. Ecke, K. Moerl, K. Schroeder, R. Spittel, R. Willsch, J. Kobelke, M. Rothhardt, L. Shan, and S. Brueckner, "Optical switch based on a fluid-filled photonic crystal fiber bragg grating," *Opt. Lett.*, vol. 34, no. 23, pp. 3683-3685, Dec. 2009.

[46] Z. Fan, S. Li, Q. Liu, G. An, H. Chen, J. Li, D. Chao, H. Li, J. Zi, and W. Tian, "High sensitivity of refractive index sensor based on analyte-filled photonic crystal fiber with surface plasmon resonance," *Photon. J.*, vol. 7, issue 3, Jun. 2015.

[47] Y. Xu, and J. Xiao, "Compact silicon hybrid plasmonic microring resonator-based polarization demultiplexer," *Jpn. J. Appl. Phys.*, vol. 54, no. 8, Jul. 2015.

[48] L. Zhang and C. Yang, "Polarization splitter based on photonic crystal fibers," *Opt. Express*, vol. 11, no. 9, pp. 1015-1020, May 2003.

[49] L. Zhang and C. Yang, "A novel polarization splitter based on the photonic crystal fiber with nonidentical dual cores," *IEEE Photon. Technol. Lett.*, vol. 16, no. 7, July 2004.

[50] L. Zhang and C. Yang, "Polarization-dependent coupling in twin-core photonic crystal fibers," *J. Lightw. Technol.*, vol. 22, no. 5, pp. 1367-1373, May 2004.

[51] L. Zhang, C. Yang, C. Yu, T. Luo and A. E. Willner, "PCF-based polarization splitters with simplified structures," *J. Lightw. Technol.*, vol. 23, no. 11, pp. 3558-3565, Nov. 2005.

[52] M. Chen, B. Sun, Y. Zhang and X. Fu, "Design of broadband polarization splitter based on partial coupling in square-lattice phtotnic-crystal fiber," *Appl. Opt.*, vol. 49, no. 16, pp. 3042-3048, June 2010.

[53] Z. Sheng, J. Wang, and R. Feng, "Design of a compact polarization splitter based on the dual-elliptical-core photonic crystal fiber," *Infrared Physics Technol.*, vol. 67, pp. 560-565, Nov. 2014.

[54] H. Jiang, E. Wang, J. Zhang, L. Hu, Q. Mao, Q. Li, and K. Xie, "Polarization splitter based on dual-core photonic crystal fiber," *Opt. Express*, vol. 22, issue 25, pp. 30461-30466, Dec. 2014.

[55] H. Rei, "Highly birefringent photonic crystal fiber polarization splitter made of soft glass," *Optik*, vol. 125, issue 22, pp. 6757-6760, Nov. 2014.

[56] Z. Fan, S. Li, J. Li, Z. Wei, and W. Tian, "Ultra-bandwidth polarization splitter based on soft glass dual-core photonic crystal fiber," *Opt. Materials*, vol. 46, pp. 384-388, Aug. 2015.

[57] W. Lu, S. Lou, X. Wang, L. Wang and R. Feng, "Ultrabroadband polarization splitter based on three-core photonic crystal fibers," *Appl. Opt.*, vol. 52, no. 3, pp. 449-455, Jan. 2013.

[58] S. Li, H. Zhang, J. Bai, W. Liu, Z. Jiang, and S. Chang, "Dual-porous fiber-based low loss broadband terahertz polarization splitter," *IEEE Photon. Technol. Lett.*, vol. 26, no. 14, pp. 1399-1402, Jul. 2014.

[59] K. Saitoh, Y. Sato and M. Koshiba, "Polarization splitter in three-core photonic crystal fibers," *Opt. Express*, vol. 12, no. 17, pp. 3940-3946, Aug. 2004.

[60] S. Li, H. Zhang, Y. Hou, J. Bai, W. Liu, and S. Chang, "Terahertz polarization splitter based on orthogonal microstructure dual-core photonic crystal fiber," *Appl. Opt.*, vol. 52, no. 14, pp. 3305-3310, May 2013.

[61] L. Rosa, F. Poli, M. Foroni, A. Cucinotta, and S. Selleri, "Polarization splitter based on a square-lattice photonic-crystal fiber," *Appl. Lett.*, vol. 31, no. 4, pp. 441-443, Feb. 2006.

[62] Z. Zhang, Y. Tsuji and M. Eguchi, "Design of polarization splitter with single-polarized elliptical-hole core circular-hole holey fibers," *IEEE Photon. Technol. Lett.*, vol. 26, no. 6, pp. 541-543, Mar. 2014.

[63] Z. Zhang, Y. Tsuji, and M. Eguchi, "Study on crosstalk-free polarization splitter with elliptical-hole core circular-hole holey fibers," *J. Lightw. Technol.*, vol. 32, no. 23, pp. 3956-3962, Dec. 2014.

[64] T. Tsuchizawa, K. Yamada, H. Fukuda, T. Watanabe, J. Takahashi, M. Takahashi, T. Shoji, E. Tamechika, S. Itabashi, and H. Morita, "Microphotonics devices based on silicon microfabrication technology," *IEEE J. Sel. Topics Quantum Electron.*, vol. 11, no. 1, pp. 232-240, Feb. 2005.

[65] W. Bogaerts, R. Baets, P. Dumon, V. Wiaux, S. Beckx, D. Taillaert, B. Luyssaert, J. Van Campenhout, P. Bienstman, and D. Van Thourhout, "Nanopho-

tonic waveguides in silicon-on-insulator fabricated with CMOS technology," *J. Ligthw. Technol.*, vol. 23, no. 1, pp. 401-402, Jan. 2005.

[66] E. Dulkeith, F. Xia, L. Schares, W. M. J. Green, and Y. A. Vlasov, "Group index and group velocity dispersion in silicon-on-insulator photonic wires," *Opt. Express*, vol. 14, no. 9, pp. 3853-3863, May 2006.

[67] L. Liu, Y. Ding, K. Yvind, and J. M. Hvam, "Silicon-on-insulator polarization splitting and rotating device for polarization diversity circuits," *Opt. Express*, vol. 19, no. 13, pp. 12646-12651, Jun. 2011.

[68] D. Dai, and J. E. Bowers, "Novel concept for ultracompact polarization splitter-rotator based on silicon nanowires," *Opt. Express*, vol. 19, no. 11, pp. 10940-10949, May 2011.

[69] Y. Ding, L. Liu, C. Peucheret, and H. Ou, "Fabrication tolerant polarization splitter and rotator based on a tapered directional coupler," *Opt. Express*, vol. 20, no. 18, pp. 20022-20028, Aug. 2012.

[70] H. Guan, A. Novack, M. Streshinsky, R. Shi, Q. Fang, A. E. Lim, G. Lo, T. B. Jones, and M. Hochberg, "CMOS-compatible highly efficient polarization splitter and rotator based on a double-etched directional coupler," *Opt. Express*, vol. 22, no. 3, pp. 2489-2496, Feb. 2014.

[71] W. D. Sacher, T. Barwicz, B. J. F. Taylor, and J. K. S. Poon, "Polarization rotator-splitters in standard active silicon photonics platforms," *Opt. Express*, vol. 22, no. 4, pp. 3777-3786, Feb. 2014

[72] L. Scolari, T. Alkeskjold, J. Riishede, A. Bjarklev, D. Hermann, A. Anawati, M. Nielsen, and P. Bassi, "Continuously tunable devices based on electrical control of dual-frequency liquid crystal filled photonic bandgap fibers," *Opt. Express*, vol. 13, no. 19, pp. 7483-7496, Sep. 2005.

[73] M. F. O. Hameed, and S. S. A. Obayya, "Analysis of polarization rotator based on nematic liquid crystal photonic crystal fiber," *J. Ligthw. Technol.*, vol. 28, no. 5, pp. 806-815, Mar. 2010.

[74] M. F. O. Hameed, and S. S. A. Obayya, "Polarization rotator based on soft glass photonic crystal fiber with liquid crystal core," *J. Ligthw. Technol.*, vol. 29, no. 18, pp. 2725-2731, Sep. 2011.

[75] M. F. O. Hameed, S. S. A. Obayya, and H. A. El-Mikati, "Passive polarization converters based on photonic crystal fiber with L-shaped core region," *J. Ligthw. Technol.*, vol. 30, no. 3, pp. 283-289, Feb. 2011.

[76] M. F. O. Hameed, A. M. Heikal, and S. S. A. Obayya, "Novel passive polarization rotator based on spiral photonic crystal fiber," *J. Ligthw. Technol.*, vol. 25, no. 16, pp. 1578-1581, Aug. 2013.

[77] M. F. O. Hameed, M. Abdelrazzak, and S. S. A. Obayya, "Novel Design of Ultra-Compact Triangular Lattice Silica Photonic Crystal Polarization Converter," *J. Ligthw. Technol.*, vol. 31, no. 1, pp. 81-86, Jan. 2013.

[78] W. Lawson, M. Esteban, H. Raghunathan, B. P. Hogan, and K. Bharathan, "Bandwidth studies of $\mathrm{TE_{0n}}$-$\mathrm{TE_{0(n+1)}}$ ripple-wall mode converters in circular waveguide," *IEEE Trans. Microw. Theory Techn.*, vol. 53, no. 1, pp. 372-379, Jan. 2005.

[79] D. Dai, S. He, and H. Tsang, "Bilevel mode converter between a silicon nanowire waveguide and a larger waveguide," *J. Ligthw. Technol.*, vol. 24, no. 6, pp. 2428-2433, Jun. 2006.

[80] J. Zhang, T. Liow, M. Yu, G. Lo, and D. Kwong, "Silicon waveguide based TE mode converter," *Opt. Express*, vol. 18, no. 24, pp. 25264-25270, Nov. 2010.

[81] C. P. Tsekrekos, and D. Syvridis, "All-fiber broadband $\mathrm{LP_{02}}$ mode converter for future wavelength and mode division multiplexing systems," *Photon. Technol. Lett.*, vol. 24, no. 18, pp. 1638-1641, Sep. 2012.

[82] X. Zhang, H. Subbaraman, A. Hosseini, and R. Chen, "Highly efficient mode converter for coupling light into wide slot photonic crystal waveguide," *Opt. Express*, vol. 22, no. 17, pp. 20678-20690, Aug. 2014.

[83] J. Qiu, D. Zhang, Y. Tian, J. Wu, Y. Li, and Y. Wang, "Performance analysis of a broadband second-order mode converter based on multimode interference coupler and phase shifter," *IEEE Photon. J.*, vol. 7, no. 5, Oct. 2015.

[84] S. Cai, S. Yu, M. Lan, L. Gao, S. Nie, and W. Gu, "Broadband mode converter based on photonic crystal fiber," *Photon. Technol. Lett.*, vol. 27, no. 5, pp. 474-477, Mar. 2015.

[85] M. Koshiba and Y. Tsuji, "Curvilinear hybrid edge/nodal elements with triangular shape for guidedwave problems," *J. Ligthw. Technol.*, vol. 18, no. 5, pp. 737-743, May 2000.

[86] N. Kejalakshmy, B.M.A. Rahman, A. Agrawal, T. Wongcharoen, and K.T.V. Grattan, "Characterization of single-polarization single-mode photonic crystal fiber using full-vectorial finite element method," *Appl. Phys. B: Laser Opt.*, vol. 93, no. 1, pp. 223-230, Oct. 2008.

[87] Y. Tsuji and M. Koshiba, "Adaptive mesh generation for full-vectorial guided-mode and beam propagation solutions," *J. Sel. Topics Quantum Electron.*, vol. 6, no. 1, pp. 163-169, Jan. 2000.

[88] Y. Li, Y. Yao, M. Hu, L. Chai, and C. Wang, "Analysis of the fundamental space-filling mode of photonic crystal fibres: a symmetry point of view," *J. Opt. A: Pure Appl. Opt.*, vol. 10, Jul. 2008.

[89] Y. Li, C. Wang, Y. Chen, M. Hu, B. Liu, and L. Chai, "Solution of the fundamental space-filling mode of photonic crystal fibers: numerical method versus analytical approaches," *Appl. Phys. B*, vol. 85, pp. 597-601, May 2006.

[90] M. Mansourabadi, A. Poorkazemi, M. Shamloufard, and Y. Riazi, "Finite-difference time-domain method solution of fundamental space-filling mode in photonic crystal fiber," *J. Appl. Sci.*, vol. 9, no. 15, pp. 2801-2807, 2009.

[91] M. Koshiba, K. Saitoh, "Simple evaluation of confinement losses in holey fibers," *Opt. Commun.*, vol. 253, issues 1-3, pp. 95-98, Sep. 2005.

[92] M. D. Nielsen, N. A. Mortensen, M. Albertsen, J. R. Folkenberg, A. Bjarklev, and D. Bonacinni, "Predicting macrobending loss for large-mode area photonic crystal fibers," *Opt. Express*, vol. 12, no. 8, pp. 1775-1779, Sep. 2005.

[93] M. Eguchi and Y. Tsuji, "Influence of reflected radiation waves caused by large mode field and large refractive index mismatches on splice loss evaluation between elliptical-hole lattice core holey fibers and conventional fibers," *J. Opt. Soc. Am. B*, vol. 30, no. 2, pp. 410-420, Feb. 2013.

[94] E. C. Mägi, P. Steinvurzel, and B. J. Eggleton, "Tapered photonic crystal fibers," *Opt. Express*, vol. 12, no. 5, pp. 776-784, Mar. 2004.

[95] S. T. Huntington, and B. C. Gibson, "A fractal-based fibre for altra-high throughput optical probes," *Opt. Express*, vol. 15, no. 5, pp. 2468-2475, Mar. 2007.

Acknowledgements

I would like to express my sincere gratitude to my advisor Prof. Yasuhide Tsuji, the Department of Information and Electronic Engineering, Muroran Institute of Technology, for the continuous support of my Ph.D study and related research, for his patience, motivation, and immense knowledge. I would like to thank him for encouraging my research and for allowing me to grow as a research scientist.

I am especially grateful to Prof. Koji Hasegawa, the Department of Information and Electronic Engineering, Muroran Institute of Technology, Prof. Shin Kagami, the Department of Information and Electronic Engineering, Muroran Institute of Technology, for their helpful discussions and suggestions.

My sincere thanks also goes to Prof. Masashi Eguchi, the Department of Photonics System Technology, Chitose Institute of Science and Technology, for his insightful comments and encouragement to my research.

Many thanks to my fellow labmaters, for their help and the fun they brought to my life. I would like to express my sincerest thanks to them all. My special thanks go to Mr. Hiroyuki Goto, Mr. Shun Kato, Mr. Kodai Nozawa, Mr. Kazuki Ichikawa, Mr. Zheng Zhong for their cooperation and encouragement. I will never forget the wonderful times we spent together.

Special thanks go to my dear Japanese friends, especially Mrs. Kozawa, Mr. Hiei, Mrs. Mitsuya, *et al.* for providing me kindly help in my daily life.

Last but not least, I want to express my deepest appreciation to my beloved family, for their understanding and supporting over these years. Everlasting gratitude for my fiancee for her confidence in me and supporting my academic. This dissertation is dedicated to them all.

List of Author's Publication

Peer-Reviewed Papers

[1] Z. Zhang, Y. Tsuji, and M. Eguchi, "Design of polarization splitter with single-polarized elliptical-hole core circular-hole holey fibers," *IEEE Photonics Technology Letters*, Vol. 26, No. 6, pp. 541–543, Mar. 2014.

[2] Z. Zhang, Y. Tsuji, and M. Eguchi, "Study on crosstalk-free polarization splitter with elliptical-hole core circular-hole holey fibers," *IEEE/OSA Journal of Lightwave Technology*, Vol. 32, No. 23, pp. 3956–3962, Dec. 2014.

[3] Z. Zhang, Y. Tsuji, T. Yasui, and K. Hirayama, "Design of ultra-compact triplexer with function-expansion based topology optimization," *Optics Express*, Vol. 23, No. 4, pp. 3936–3950, Feb. 2015.

[4] K. Ichikawa, Z. Zhang, Y. Tsuji, and M. Eguchi, "A single-polarization holey fiber with anisotropic lattice of circular air holes," *IEEE/OSA Journal of Lightwave Technology*, Vol. 33, No. 18, pp. 3866–3871, Sep. 2015.

International Conference

[1] Z. Zhang, Y. Tsuji and M. Eguchi, "A study on crosstalk-free polarization splitter based on single-polarized photonic crystal fibers," Progress In Electromagnetics Research Symposium (PIERS 2014), 2014年8月. (Guangzhou; China)

[2] Z. Zhang, Y. Tsuji and M. Eguchi, "Study on polarization splitter and converter using square lattice elliptical-hole core circular-hole holey fibers," Progress In Electromagnetics Research Symposium (PIERS 2015), 2015年7月. (Prague ; Czech Republic)

Conference Presentation

[1] 張 沢君，辻 寧英，江口真史，“楕円ホールコア円形ホールホーリーファイバを用いた偏波分離素子に関する検討”，平成24年度IEICE北海道支部学生会インターネットシンポジウム，104-3，2013年2月.

[2] 張　沢君，辻　寧英，江口真史，“楕円ホールコア円形ホールホーリーファイバを用いた偏波分離素子の設計”，電子情報通信学会技術研究報告，Vol. 113，No. 142，OPE2013-30, pp. 87–92, 2013年7月.

[3] 張　沢君，加藤　駿，辻　寧英，安井 崇，平山浩一，“進化的アルゴリズムを用いた光回路デバイスの最適設計”，電気学会電子・情報・システム部門大会，MC4-3，2013年9月.

[4] 張　沢君，辻　寧英，江口真史，“楕円空孔フォトニック結晶ファイバを用いた偏波分離素子のFSMによる設計”，電気学会電子・情報・システム部門大会，PS6-4，2013年9月.

[5] 張 沢君，辻 寧英，江口 真史，“絶対単一偏波フォトニック結晶ファイバを用いた偏波分離素子に関する検討”，平成25年度電気・情報関係学会北海道支部連合大会，128，2013年10月.

[6] 張　沢君, 辻　寧英, 江口真史, “楕円ホールコア円形ホールホーリーファイバを用いた偏波分離素子に関する研究”，平成25年度IEICE北海道支部学生会インターネットシンポジウム，104-3，2014年2月.

[7] 市川和輝，張　沢君，辻　寧英，江口真史, “異方的な空孔格子を用いた単一偏波ホーリーファイバに関する検討”，電子情報通信学会技術研究報告，Vol. 114，No. 14，MWP2014-8，pp. 39–44，2014年4月.

[8] 張　沢君，辻　寧英，江口真史，“単一偏波フォトニック結晶ファイバを用いた偏波分離素子の特性に関する検討”，電子情報通信学会技術研究報告，Vol. 114，No. 142，EST2014-26，pp. 99–104，2014年7月.

[9] 張 沢君，辻 寧英，江口 真史，“正方格子楕円ホールコア円形ホールホーリーファイバを用いた偏波分離・変換素子に関する検討”，平成26年度電気・情報関係学会北海道支部連合大会，103，2014年10月.

[10] 市川和輝，張　沢君，辻　寧英，江口真史，“異方的な空孔格子を用いた単一偏波フォトニックバンドギャップファイバに関する検討”，

平成26年度電気・情報関係学会北海道支部連合大会，105，2014年10月.

[11] 張 沢君，辻 寧英，江口真史，“正方格子楕円ホールコア円形ホールホーリーファイバを用いた偏波分離・変換素子に関する研究”，IEICE 北海道支部学生会インターネットシンポジウム，，2015年2月.

[12] 市川和輝，張　沢君，辻　寧英，江口真史，“異方性空孔格子を用いた単一偏波フォトニックバンドギャップファイバの広帯域化に関する検討”，IEICE 北海道支部学生会インターネットシンポジウム,，2015年2月.

[13] 鐘　正，張　沢君，辻　寧英，江口真史，“正方格子単一偏波フォトニック結晶ファイバを用いた偏波分離素子に関する検討”，IEICE 北海道支部学生会インターネットシンポジウム,，2015年2月.

[14] Z. Zhang, Y. Tsuji, and M. Eguchi, “Study on polarization splitter and converter using square lattice elliptical-hole core circular-hole holey fiber,” 電子情報通信学会総合大会，C-15-9，2015年3月.

[15] Zheng Zhong, Zejun Zhang, Yasuhide Tsuji, and Masashi Eguchi，“Design of crosstalk-free polarization splitter based on square lattice single polarization photonic crystal fibers,” 電子情報通信学会技術研究報告，vol. 115， no. 143， OPE2015-54， pp. 197–201， 2015年7月.

[16] Z. Zhang, Y. Tsuji, and M. Eguchi, “A study on mode converter/splitter based on single-polarization holey fiber,” 電子情報通信学会技術研究報告，vol. 115，no. 259，EMCJ2015-60，pp. 7–10，2015年10月.

[17] 市川和輝，張　沢君，辻　寧英，江口真史，“異方的な空孔格子を用いた単一偏波PCFによる偏波分離素子の検討”，電子情報通信学会技術研究報告， vol. 115， no. 259， EMCJ2015-61， pp. 11–16，2015年10月.

[18] 市川和輝，張　沢君，辻　寧英，江口真史，“異方的な空孔格子を用いたフォトニック結晶ファイバ型偏波回転素子に関する検討”，平成27年度電気・情報関係学会北海道支部連合大会，147，2015年11月.

[19] 市川和輝，張　沢君，辻　寧英，江口真史，“異方的な空孔格子を用いた単一y偏波ホーリーファイバに関する検討”，IEICE 北海道支部学生会インターネットシンポジウム，2016年2月.